UNIVERSITY OF CALIFORNIA
SANTA CRUZ

INTERIOR STRUCTURE OF THE GAS GIANTS: THERMAL EVOLUTION AND NORMAL MODE SEISMOLOGY

A dissertation submitted in partial satisfaction of the
requirements for the degree of

Doctor of Philosophy

in

ASTRONOMY AND ASTROPHYSICS

by

Christopher R. Mankovich

June 2019

The Dissertation of Christopher R. Mankovich
is approved:

Jonathan J. Fortney, Chair

Mark S. Marley

Ruth Murray-Clay

Francis Nimmo

Lori G. Kletzer
Vice Provost and Dean of Graduate Studies

Table of Contents

List of Figures

List of Tables

Abstract

Interior Structure of the Gas Giants: Thermal evolution and normal mode seismology

by

Christopher R. Mankovich

Understanding the structure and composition of gas giants is of basic importance to planetary astrophysics. Our local exemplars Jupiter and Saturn permit spatially resolved observations from Earth as well as sensitive *in situ* observations by spacecraft. This intersection of physical accessibility and conceptual importance for the planet formation process renders Jupiter and Saturn essential for establishing baseline truth for exploration of the assembly and evolution of planetary systems in general. In this thesis I develop new models for the structure and evolution of these solar system gas giants, bringing spacecraft observations to bear on our understanding of the physical processes at work in giant planet interiors.

I first describe evolutionary models for Jupiter and Saturn that incorporate results from first-principles simulations of hydrogen-helium mixtures at high pressures to address how the helium distribution is likely to evolve in these planets as they cool. Bayesian parameter estimation is used to retrieve the distribution of likely thermal histories for Jupiter and Saturn. I present models that reconcile Jupiter and Saturn's observed heat flow, and Jupiter's atmospheric helium depletion, at the solar age. These solutions put stringent limits on the uncertain physics of helium immiscibility, and

translate to a precise prediction for the unknown atmospheric helium content of Saturn.

Second, I describe seismology of Saturn using ring waves driven by gravitational perturbations from the planet's nonradial oscillations. I present a family of Saturn interior models together with their normal mode eigenfrequencies and corresponding resonances with orbits in Saturn's C ring, where more than twenty otherwise unexplained waves have been characterized using Cassini stellar occultation data. I identify the fundamental modes of Saturn at the origin of these ring waves, and use their observed frequencies and azimuthal wavenumbers to estimate Saturn's rotation period to within ± 2 minutes. This yields a period significantly faster than those in Saturn's kilometric radiation, the traditional proxy for Saturn's unknown rotation period. The global fit does not exhibit any clear systematics indicating strong differential rotation in Saturn's outer envelope.

Acknowledgments

First and foremost I thank Jonathan Fortney, whose support as an advisor both stoked the curiosity and created the space that I needed in order to make my modest contributions. Jonathan is constantly setting an example as a scientist and as a leader, and I learned a great deal from witnessing his unfailing conscientiousness firsthand over the years. In retrospect I cannot believe my luck. On a not coincidental note, I would like to thank the Fortney group at large—including Caroline, Eric, Nadine, Naor, Daniel, Vivien, Kat, Mike, Ty, Angie, and many others—for being such a supportive, stimulating, and fun research environment and for introducing me to so many gifted people.

I owe a great deal of thanks also to Mark Marley, if not for his patience and generosity as a brilliant second advisor over the last few years, then for whatever combination of courage, stubbornness, and scientific rigor led him to develop and defend Saturn ring seismology as a topic of legitimate scientific merit in the course of his Ph.D. research circa 1990 and ultimately in his collaboration with Carolyn Porco. It has been a pleasure to build on that vision decades later by dotting some i's and crossing some t's and uncovering a surprise or two along the way. In this Mark has been the most pleasant of surprise collaborators and mentors, and to him I am grateful.

Even with the help of gifted mentors, I would be nowhere without the camaraderie and support I felt among the astronomy graduate students at UC Santa Cruz. This includes my stately elders Caroline, Claire, Angie, Jenn, John, Nathan, Rosalie, Justin, and many more for being true role models for me when I was just getting my

start; thanks also to my closer contemporaries Emily, Phil, Alexa, Jieun, Zach, Alex, and more still for helping me through the sticking points and dark days. I would also like to thank the (increasingly innumerable) students in later cohorts for continuing this tradition that I have been priveleged to live through, and for generally excelling to a degree that makes me wonder how I ever got into this school in the first place.

Special thanks go to my dear Santa Cruz friends Phil, Jieun, Emily, Alexa, Zach, and Ben for making this the time of my life and for confirming my suspicion that graduate school might lead me to some of the most funny, peculiar, capable, and lovely people I would ever meet.

Especially special thanks, then, to Jieun, easily the most significant discovery I made in my time at Santa Cruz. She is my friend and companion in the truest sense of each. Astronomy brought her into my life, and with her she brought a little magic.

Thanks finally to my parents Betsy and Nick, whose sheer competence and openness to the world's possibilities always made me feel invincible, and to my brothers Gabe and Al. I am uniquely me, but even more, we are uniquely us.

Published Material

The text of this dissertation includes reprints of the following published material led by Mankovich, with the permission of the listed coauthors.

Chapter 2 was published in the literature as Mankovich et al. (2016). I was responsible for developing the models, performing the analysis, writing the text, and creating the figures. I wish to thank my coauthors Jonathan J. Fortney and Kevin L. Moore for their generous support and feedback in the course of this research.

Chapter 4 was published in the literature as Mankovich et al. (2019). I was responsible for developing the models and performing the analysis, as well as creating the figures and writing the text with the exception of §4.1.1 written by Mark S. Marley. I wish to thank my coauthors Mark S. Marley, Jonathan J. Fortney, and Naor Movshovitz for their generous support and feedback in the course of this research.

Scientific Acknowledgments

I gratefully acknowledge research support from NASA through its Earth and Space Science Fellowship program grant NNX15AQ62H. This research was further supported by NASA's *Cassini* Participating Scientist program grant NNX16AI43G to Jonathan Fortney. The University of California supported this work through multi-campus research award 00013725 for the Center for Frontiers in High Energy Density Science. Some of the calculations herein made use of the Hyades supercomputer at UCSC, supported by NSF grant AST-1229745 and the University of California, Santa Cruz and graciously mantained by Brant Robertson and previously by Shawfeng Dong.

I further give thanks to Philip Nicholson, Matthew Hedman, and Richard French for extensive conversations about their painstaking detection and characterization of the wave features in *Cassini* stellar occultation data that made Chapter 4 possible. I thank also Nadine Nettelmann, Daniel Thorngren, Andrew Ingersoll, Jim Fuller, Burkhard Militzer, Stephen Markham, Ethan Dederick, William Hubbard, and David Stevenson for enlightening conversations that helped shape the direction of this dissertation research at one time or another. I thank Manuel Schöttler for kindly supplying the phase diagram data used in Chapter 3.

For Tuff and Victoria

Chapter 1

Introduction

Cool giant planets are relics of the protoplanetary systems from which they formed in the sense that they do not carry out nuclear fusion, and they are well-bound enough that even hydrogen does not escape appreciably over tens of billions of years. As a result their thermal evolution is not intractably complicated, and simulating it empowers us to use the present states of the giant planets to test ideas pertaining to their history and formation. The major open questions about planet formation—do gas giants form by core accretion or by disk instability? To what degree do their observable abundances represent their bulk abundances?—thus motivate a comprehensive theory of giant planet evolution, the development of which will continue to be driven heavily by our nearby, well-studied gas giants Jupiter and Saturn.

This thesis is concerned with the evolution and interior structures of Jupiter and Saturn, particularly as informed by a spate of recent developments spanning the disciplines of dense matter physics and planetary science. The work presented here was

completed during an eventful time for exploration of the outer planets by spacecraft, most notably the arrival of *Juno* (Bolton et al. 2017) at Jupiter and the culmination of the *Cassini* mission (Edgington & Spilker 2016) at Saturn, and aims to synthesize some of those results into a refined understanding of the jovian interiors. This requires the application of models to turn the tangible fundamental characteristics of these planets—typically their temperatures, radii, and gravity fields—into inferences about the physics of their interiors. First I will briefly develop some background.

1.1 Modeling a giant planet

The essence of a stable self-gravitating fluid planet is captured by a system of four differential equations

$$\frac{\partial m}{\partial r} = 4\pi r^2 \rho \tag{1.1}$$

$$\frac{\partial P}{\partial r} = -\rho g \tag{1.2}$$

$$\frac{\partial L}{\partial m} = -T\frac{ds}{dt} \tag{1.3}$$

$$\frac{\partial T}{\partial m} = -\nabla \frac{T}{P}\frac{Gm}{4\pi r^4 \rho} \tag{1.4}$$

representing the conditions of mass conservation, momentum conservation, energy conservation, and thermal transport. Combined with an equation of state $\rho(P, T, \{X_i\})$, a model for the distribution of the mass fractions $\{X_i\}$, and appropriate boundary conditions, solutions to this system can be sought, and the result is a model for the structure and evolution of a planet as a whole. The most flexible and realistic solutions are usu-

ally sought numerically, and such numerical models are the principal tool used for the work described in this thesis. Myriad simplifications have been made in order for these equations to appear in this simple form, notably (i) the strong assumption of sphericity allowing us to neglect horizontal forces and temperature gradients, and (ii) the hydrostatic assumption allowing us to neglect fluid accelerations. Assumption (i) is called into question when one appreciates that planets are generally rotating, introducing for example Coriolis and centrifugal forces that warrant at least a two-dimensional description. Assumption (ii), while certainly valid in establishing the background structure of the planets, likewise ignores potentially interesting behavior that can take place on timescales close to the dynamical timescale. Depending on the questions being asked of the model, these can be critical ingredients, and indeed in Chapter 4 below special methods are used to address these very issues in the context of normal mode oscillations of the rapidly rotating Saturn. Chapters 2 and 3 are concerned with the broader thermal evolution of Jupiter and Saturn where the one-dimensional hydrostatic description suffices.

Still, untold complexity lurks even in this simplified description. The single term on the right-hand side of Equation 1.3 monolithically captures heating and cooling from a variety of sources including compression, irradiation, differentiation, and accretion, the balance among which sets the luminosity throughout the planet. Likewise in Equation 1.4 the factor $\nabla \equiv \mathrm{d}\ln T/\mathrm{d}\ln P$ representing the temperature gradient in the interior rather cryptically encapsulates the full description of how heat is transported in the planet's interior, be it by radiative or conductive diffusion, turbulent convective

motions, some combination of these mechanisms, or somewhat more subtle small-scale mixing processes. There remains significant uncertainty about which among these modes of thermal transport are significant in the interiors of giant planets, leading to a broad range of plausible values for ∇ and consequently to uncertain interior structures and evolution pathways. The major goal of the first part of this work is to use the more detailed constraints available only for Jupiter and Saturn in order to identify what energy sources and heat transport mechanisms are necessary to give a satisfactory explanation for these planets' heat flow at the present day.

1.1.1 Power sources and heat flow

It has been appreciated since Low (1966) that Jupiter and Saturn radiate more thermal energy than they receive in the form of solar light, indicating that they possess significant internal sources of luminosity. Soon after, it was shown by Hubbard (1968) that Jupiter's interior was probably fully convective, a result of the large radiative and conductive opacities in the hydrogen-dominated interior. In fact, these opacities are so large that for realistic estimates of the total Jovian flux, nearly perfect convection would carry the heat flux in the interior, and consequently the interior of the planet should be close to an adiabatic stratification, i.e.,

$$\nabla \approx \nabla_{\rm ad} \tag{1.5}$$

where $\nabla \equiv \mathrm{d}\ln T/\mathrm{d}\ln P$ is the temperature gradient and $\nabla_{\rm ad} \equiv (\partial \ln T/\partial \ln P)_{\rm ad}$ is the adiabatic temperature gradient, a fundamental property of the equation of state.

Equation 1.5 reflects the simple fact that in the limit of little leakage of heat out of convective upwellings by radiative or conductive diffusion, they will retain virtually all of their initial specific entropy, and thus large-scale convective motions will lead to a structure wherein $\mathrm{d}s/\mathrm{d}r \approx 0$. In reality these diffusive processes, however minuscule, do occur and so convection is never perfect; as a result $\mathrm{d}s/\mathrm{d}r \lesssim 0$ and $\nabla \gtrsim \nabla_{\mathrm{ad}}$. Typical realistic values *in a convective layer* in the interior of Jupiter or Saturn are $\nabla - \nabla_{\mathrm{ad}} \sim 10^{-9}$–$10^{-6}$ so that Equation 1.5 is an excellent approximation. Thus if these planets are indeed *fully* convective then Equation 1.4 taken with $\nabla = \nabla_{\mathrm{ad}}$ straightforwardly provides the temperature throughout the interior.

Further support for the paradigm of the fully convective gas giant came from evolutionary models. The basic picture from Hubbard (1968) of an initially hot, fully convective Jupiter deriving its intrinsic flux from the thermal energy of baryons (principally hydrogen) proved to yield a cooling time roughly in line with the age of the solar system (Hubbard 1969), a finding bolstered by more detailed calculations by Graboske et al. (1975) and others since. The evolution of Jupiter can thus be framed in broad strokes as a prolonged Hayashi-track-like contraction for a failed star, albeit one with a partially degenerate interior and a surface boundary condition complicated by chemistry and input from its host star.

The major issues with this picture emerge when the same ideas are applied to Saturn, a planet one third the mass of Jupiter and ~ 30 K colder but otherwise ostensibly quite similar. The same assumptions that lead to successful evolutionary models for Jupiter vastly underpredict Saturn's observed luminosity (Pollack et al. 1977;

Grossman et al. 1980; Fortney et al. 2011; Nettelmann et al. 2013), indicating either that another energy source beyond simple Kelvin-Helmholtz contraction is operating, or that at least part of the interior is not convective and therefore the interior temperatures deviate from those expected for an adiabat. Several lines of reasoning point toward a reality that probably involves both (Stevenson 1982a).

1.1.2 Phase transitions

To identify what processes might be responsible for these complications, it is helpful to gather some perspective on the characteristics of hydrogen-helium mixtures at the conditions relevant for the interiors of the gas giants.

Hydrogen metallization

As was appreciated in the earliest interior models of Smoluchowski (1967) and Hubbard (1968), for the temperatures relevant to Jupiter and Saturn there exists a phase transition in the neighborhood of $P \sim 10^{12}$ dyne cm^{-2} $= 10^6$ bar separating molecular hydrogen from a denser, pressure-ionized metallic phase of hydrogen. This denser metallic fluid phase comprises the inner $\sim 80\%$ of Jupiter's mass and $\sim 50\%$ of Saturn's mass. It has been debated whether this hydrogen phase transition is a first-order phase transition in the sense that it is necessarily accompanied by a discontinuous change in density and a release of latent heat (e.g., Stevenson & Salpeter 1977a; Saumon et al. 1995). In more recent years, *ab initio* methods used to simulate dense matter systems directly on small scales have uncovered no strong evidence for a first-order transition in hydrogen at the temperatures relevant to giant planets, indicating that

the change from molecular to metallic hydrogen may in fact be a gradual transition within these planets (McMahon et al. 2012). While this question is far from settled, it appears that interior models for Jupiter and Saturn need not involve a first-order phase transition for hydrogen.

Hydrogen-helium immiscibility

A distinct but closely related phase transition concerns the behavior of helium in metallic hydrogen. Helium remains essentially perfectly neutral under Jovian conditions, and as a result has imperfect solubility in the pressure-ionized liquid metallic hydrogen. This means that generally speaking, a sufficiently cooled hydrogen-helium fluid at $P \gtrsim 10^6$ bar will tend to separate into a helium-poor phase and a denser helium-rich phase, with the density (or helium fraction) contrast between the two phases increasing as the fluid is cooled (Salpeter 1973; Stevenson 1975; Stevenson & Salpeter 1977a). This hydrogen-helium phase transition sets in at temperatures comparable to the temperatures of the metallic layers inside Jupiter, and thus the phase separation of helium may be occuring in both Jupiter and Saturn. The preference for the resulting overdense helium-rich droplets to fall deeper into the metallic layers—a helium rain—may have major ramifications for both of these planets because it both provides an additional luminosity source and establishes composition gradients that may inhibit convection in their deep interiors (Salpeter 1973; Flasar 1973; Stevenson & Salpeter 1977b). While the P–T conditions describing this phase transition have been historically quite uncertain, and hence its relevance Jupiter and Saturn somewhat unclear, more recent *in situ* measurements of Jupiter's atmospheric helium depletion (Niemann et al. 1998; von

Zahn et al. 1998) and its related neon depletion (Mahaffy et al. 2000; Wilson & Militzer 2010) suggest that the action of helium rain is all but a certainty in cold planets at a Jupiter mass or less. The process may have conceivably even occurred in Uranus and Neptune provided that their $P \gtrsim 10^6$ bar regions possessed a supercritical mixing ratio of helium to metallic hydrogen.

The *ab initio* simulations alluded to above have been a major driver of the progress in modeling giant planets over the last decade, pushing to conditions inaccessible to laboratory experiment in order to quantitatively map out the relevant equations of state (Militzer et al. 2008; French et al. 2009; Militzer & Hubbard 2013; Becker et al. 2014; Chabrier et al. 2019), transport properties (French et al. 2012), and the conditions for hydrogen-helium immiscibility (the H-He phase diagram; Lorenzen et al. 2009, 2011; Morales et al. 2009, 2013; Schöttler & Redmer 2018), making possible a new generation models for the *static* structure of Jupiter and Saturn (Nettelmann et al. 2012, 2013; Hubbard & Militzer 2016a; Miguel et al. 2016), including those ultimately used to interpret the sensitive gravity field data gathered by *Juno* at Jupiter (Guillot et al. 2018) and by *Cassini* at Saturn (Iess et al. 2019). Models like these have yielded important insights about the interior mass distributions, as well as the groundbreaking discovery of deep differential flows in both Jupiter and Saturn.

However, the questions associated with the long-term thermal evolution of these planets remain unresolved. In particular, no entirely satisfying realization of the ideas that Stevenson & Salpeter (1977b) first presented in depth has been found, leaving open the questions: can helium rain realistically explain Saturn's large luminosity at

the solar age? Can the same physical assumptions address Jupiter's heat flow without compromising the apparently good fit obtained for homogeneous, adiabatic models? And conversely, if Jupiter and Saturn are treated as a laboratory for dense matter physics, are the *ab initio* models for hydrogen-helium systems converging on reality? Evolution models including the hydrogen-helium immiscibility in these planets have begun to shed some light on these questions (Hubbard et al. 1999; Fortney & Hubbard 2003; Nettelmann et al. 2015; Püstow et al. 2016), but a cohesive description of the heat flow and helium abundances in *both* planets at the solar age has eluded the field. Chapter 2, initially published as Mankovich et al. (2016), and Chapter 3, to be published soon after this dissertation, aim to provide such a description by applying the state of the art in the equation of state and phase diagram of hydrogen-helium mixtures. The reader is forewarned that the results of these two chapters are substantially different, owing in part to this developing state of the art in hydrogen-helium physics, and in part to a recent *Cassini* measurement of Jupiter's intrinsic flux (Li et al. 2018) that significantly changes the picture for Jupiter's cooling.

1.2 Seismology as the frontier in giant planet astrophysics

The chief constraint on the internal structures of solar system planets other than Earth is their gravity field, which for a rotating, oblate planet deviates from a simple spherical potential in a manner that depends on the internal mass distribution. The sensitive gravity field measurements made at the culmination of NASA's *Juno* (Iess et al. 2018) and *Cassini* (Edgington & Spilker 2016) missions represent a historic con-

tribution in this arena, enabling for example the discovery of deep differential rotation in both Jupiter (Kaspi et al. 2018; Guillot et al. 2018) and Saturn (Iess et al. 2019). Gravity field measurements like these are in principal sensitive to the quantities most pressing to formation and evolution questions, for instance the deep envelope metallicity and the mass of the dense rock/ice core, if one exists. However, quantitative conclusions based on interpretation of a gravity field alone are inevitably model-dependent and subject to fundamental issues of nonuniqueness and parameter degeneracy (e.g., Helled & Stevenson 2017). Thus in the interest of long-term progress there is a need to identify independent observational means of studying the interiors of these planets.

In this regard seismology is the leading prospect. Just as helioseismology revolutionized solar astrophysics in the 1970s and 1980s (Christensen-Dalsgaard 2002) and *Kepler* and *CoRoT* asteroseismology has likewise done for stellar astrophysics over the last decade (Chaplin & Miglio 2013), the interpretation of normal mode oscillations in giant planets has the potential to radically change the way we study their interiors. In simple terms, any measured frequency that can be identified with a normal mode oscillation of a planet is a powerful constraint on the parts of the interior where that mode has significant amplitude. Like the components of the planet's static gravity field, the frequency of a normal mode is sensitive to the interior mass distribution, but also to other interior properties of fundamental interest: depending on the nature of the restoring force supporting a given oscillation mode, its frequency can generally shed light directly on the type of heat transport operating in the planet's interior, as well as the interior rotation. The latter possibility is especially intriguing in the case of Saturn,

whose rotation rate—a critical input for, e.g., gravity field modeling—is otherwise poorly constrained.

Preliminary detections of Jupiter's oscillations have already been made from the ground (Mosser et al. 1993; Gaulme et al. 2011), where observations rely on spatially resolved radial velocity maps of the planet's surface. These observations are most sensitive to the acoustic overtone (p–)modes, essentially trapped sound waves the likes of which have yielded most of the information about the solar interior from global helioseismology. The general structure of the power spectrum of Gaulme et al. (2011) accords well with expectations from Jupiter interior models, but little else of use can be gleaned until a spectrum is obtained with a frequency precision sufficient to isolate individual normal modes. Astronomers appear poised for a breakthrough along these lines with the broad longitudinal baseline of the JOVIAL campaign (Schmider et al. 2013).

Meanwhile, the *Cassini* mission has delivered a different dataset that is proving quietly transformative for our ability to study the interior of Saturn in particular. Peering at bright stars through Saturn's translucent C ring, *Cassini* achieved high-resolution optical depth scans that allowed for the characterization of dozens of waves in Saturn's rings that are driven by the oscillations of Saturn itself through orbital resonances, confirming *Voyager*-era predictions (Stevenson 1982; Marley 1990, 1991; Marley & Porco 1993) that Saturn's expansive ring system could be acting as a sensitive seismograph for the planet. More than 20 such waves have now been characterized from *Cassini* stellar occultations (Hedman & Nicholson 2013, 2014; French et al. 2016, 2019; Hedman et al.

2019) in terms of their frequencies and azimuthal orders (spiral arm numbers) m. The result is the first ever giant planet power spectrum with sufficient precision to isolate individual normal modes, ushering in the era of bona fide giant planet seismology.

As a whole this dataset is well described by the theoretical formalism and quantitative predictions of Marley (1990, 1991); Marley & Porco (1993), who demonstrated that the rings would be most sensitive to forcing by Saturn's fundamental (f–) modes in particular. However, the details of the spectrum built up by *Cassini* reveal unforeseen complexity that has already yielded important discoveries for Saturn's interior. An unexpected and profound implication of the first Saturnian waves detected (Hedman & Nicholson 2013) was the presence of *clusters* of spiral density waves with the same value of m in close proximity to one another, where the f–mode spectrum predicts only a single wave. Fuller (2014) demonstrated that this could be naturally explained if Saturn hosts not only the inevitable f–modes, but also internal gravity (g–) modes in its deep interior. The presence of g–modes in Saturn is profound because these require a stable thermal stratification, a possibility excluded by the traditional assumption of the interior as fully convective. These new constraints are thus critically important with respect to the open questions about Saturn's heat flow discussed above. Nonetheless Chapter 4 below, originally published as Mankovich et al. (2019), limits its attention to the subset of *Cassini* waves that are unaffected by mode mixing—indeed the majority of the spectrum observed so far—to identify the Saturnian f–modes responsible and use their frequencies to measure Saturn's bulk rotation rate. The observed mixed modes are an important opportunity for future work and will be discussed in Chapter 5.

1.3 Outline of this work

Chapter 2 recapitulates the main ideas surrounding hydrogen-helium immiscibility, applying a recent hydrogen-helium phase diagram to thermal evolution models of Jupiter. Chapter 3 builds on these calculations by applying a more accurate equation of state and hydrogen-helium phase diagram, incorporating a new measurement of Jupiter's intrinsic flux, and extending the model to the case of Saturn; the conclusions reached therein are quite different from those in Chapter 2 owing to these substantial updates. Chapter 4 presents a different, complementary approach toward the same big-picture questions, applying normal mode seismology to examine powerful new constraints on Saturn's interior structure based on signatures left in the rings by the planet's free oscillations. Finally Chapter 5 summarizes these results and discusses lines for future inquiry.

Chapter 2

Helium rain and double-diffusive convection in Jupiter

2.1 Introduction

A Henyey-type stellar evolution calculation for a Jupiter-mass object was first performed by Graboske et al. (1975), who showed that a convective, homogeneous sphere of fluid hydrogen and helium could cool to Jupiter's observed luminosity over roughly the right timescale, and noted that among all model inputs, the equation of state (EOS) and superadiabaticity of the temperature gradient have the strongest influence on the overall cooling time.

These two fundamental physical inputs are closely related. The EOS (paired with a hydrostatic model) is necessary to translate the planet's tangible properties (surface temperature and composition; external gravity field, size and shape) into an

interior density distribution. Knowledge of the thermodynamic state of matter in these regimes includes understanding any phase transitions that can operate in a Jovian-mass planet's interior, the two most important of which are (i) the transition from molecular hydrogen to its denser, pressure-ionized "liquid metallic" phase, and (ii) the limited solubility of neutral helium in that liquid metallic hydrogen once it cools below a critical temperature (Stevenson 1975). The latter of these two effects has observable ramifications because the helium-rich phase tends to sink, releasing gravitational energy (constituting a power source beyond mere contraction) and depleting the outer envelope in helium (Salpeter 1973; Stevenson & Salpeter 1977b). Ultimately a robust theory of giant planet evolution must reconcile the atmospheric helium mass fraction $Y_{\rm atm}$ with the helium content of the protosolar nebula, and this demand constrains the plausible EOS and H-He phase diagram.

Since the critical temperature for H-He phase separation increases with pressure more slowly than the temperature along a planetary adiabat, the equilibrium helium abundance increases toward the center the planet. Thus in the limit that the hydrogen-helium mixing ratio is equal to its equilibrium value throughout the liquid metallic hydrogen part of the mantle, there exists a stabilizing helium gradient that acts to mitigate the convectively unstable temperature gradient. In this case the dynamics of the fluid (and the degree of macroscopic vertical heat transport that ensues) are dictated by the competing microscopic diffusion of heat and solute; the fluid is in the double-diffusive regime. In such a region the temperature gradient can be significantly larger than the adiabatic gradient, leading to potentially dramatic modifications to the

planet's cooling time. For example, double-diffusive convection has been invoked in recent years to explain Saturn's luminosity excess (Leconte & Chabrier 2013a; the case of a global heavy-element gradient), the inflation of hot Jupiters (Kurokawa & Inutsuka 2015), and Jupiter's late thermal evolution including helium rain (Nettelmann et al. 2015), which we are revisiting in this paper. Although differentiation alone contributes additional luminosity, extending the overall cooling time, any superadiabatic temperature structure associated with double-diffusive convection generally cools the surface more quickly. For models undergoing helium rain, cases with adiabatic $P - T$ profiles thus give an upper limit to the cooling time (Fortney & Hubbard 2003, Püstow et al. 2016). The inclusion of double-diffusive convection offers a continuum of shorter cooling times, modulated by the efficiency of the heat transport through the double-diffusive region.

Nettelmann et al. (2015) sought a solution for Jupiter's evolution to its current state assuming a superadiabatic temperature profile in the framework of layered double-diffusive convection (LDDC; Mirouh et al. 2012, Wood et al. 2013) and found that a suitable combination of LDD layer height and modifications to the H-He phase diagram could match Jupiter's observed 1-bar temperature and $Y_{\rm atm}$. However, it is likely that a quasi-stable turbulent state like the layered structures characterized by the direct hydrodynamics simulations of Wood et al. (2013) would look quite different in the presence of a phase transition and rainout of a main component. For example, in the context of helium phase separation, homogeneous layers themselves—finite volumes of (P, T) space, at effectively uniform helium abundance—are intrinsically unstable to

H-He phase separation, and the influence that droplet formation and rainout has on the merging or bifurcation of convective layers, or the transport of solute between layers, has yet to be assessed from the hydrodynamical perspective. The present work thus relaxes the assumption of layered convection, opting instead to treat the superadiabaticity with a generic parameterization, the only physical content of which is the demand that the temperature gradient lie somewhere between the minimum value for overstable double-diffusion and the upper limit imposed by the Ledoux criterion. This amounts to the criterion that gravity waves be linearly overstable, so that thermal transport is enhanced relative to the purely diffusive case by some degree of turbulence.

Despite growing confidence that helium has begun differentiating in Jupiter's recent past (and billions of years ago in the case of Saturn; see Fortney & Hubbard 2003 and Püstow et al. 2016), it is not known whether helium rain alone can resolve the gaps in our understanding of giant planet evolution given Jupiter and Saturn's luminosities and the helium content of their molecular envelopes at the present day. Although the thermodynamic conditions for phase separation of helium from liquid metallic hydrogen have been evaluated since the early work of Stevenson (1975) and Straus et al. (1977), quantitative knowledge covering the relevant pressures and H-He mixing ratios has only become available over the past several years as a result of *ab initio* simulations making use of density functional theory molecular dynamics (Morales et al. 2009; Lorenzen et al. 2009, 2011; Morales et al. 2013). The present work demonstrates that using *ab initio* results for the H-He phase diagram, a differentiating non-adiabatic Jupiter comprised of hydrogen and helium surrounding a dense core of heavy elements explain Jupiter's

evolutionary state at the solar age.

To assess the viability of the evolution models, we formulate the problem in a Bayesian framework, using Jupiter's observed $T_{\rm eff}$, $Y_{\rm atm}$, and volumetric mean radius $R_{\rm vol}$ to derive posterior probability distributions for the model parameters using a Markov chain Monte Carlo sampling algorithm. Most importantly, we make a probabilistic determination of the superadiabatic temperature gradient to be expected in the deep interior, and simultaneously estimate the temperature correction that must be applied to the Lorenzen et al. (2011) phase diagram to satisfy the *Galileo* entry probe measurement of $Y_{\rm atm}$ (Nettelmann et al. 2015). The present work thus extends the basic approach of Fortney & Hubbard (2003)—using forward thermal evolution models to infer a most likely H-He phase diagram—with the power of a Bayesian parameter estimation method and the treatment of non-adiabatic $P-T$ profiles.

In §2.2 we describe our modeling approach using Modules for Experiments in Stellar Astrophysics (MESA; Paxton et al. 2011, 2013, 2015), including our atmospheric boundary condition, treatment of helium phase separation, thermal transport, and other modifications that were necessary for our application. We describe the three free parameters in our inhomogeneous, non-adiabatic models, namely the heavy-element core mass $M_{\rm c}$, the double-diffusive superadiabaticity (or "density ratio") R_ρ, and the phase diagram temperature offset $\Delta T_{\rm phase}$. In §2.3 we present results of evolutionary calculations, first validating our models for the case of homogeneous composition, then discussing in detail the late inhomogeneous, non-adiabatic evolution as a result of helium rain. We then repeat these calculations, but treating the planet's equilibrium tempera-

ture $T_{\rm eq}$ as a fourth free parameter controlling the overall cooling time, mimicking the influence of a "colder" or "warmer" EOS than the adopted Saumon et al. (1995) EOS. Marginalizing over this parameter allows us in an indirect sense to marginalize over the plausible H-He equations of state and thus obtain the most general estimates for the remaining three parameters. In §2.4 we summarize and contextualize our findings.

2.2 Planetary evolution models

Our evolution models are computed using MESA version 8118. The models are hydrostatic, nonrotating spheres with envelopes consisting of binary mixtures of ^{1}H and ^{4}He surrounding dense inert cores of heavy elements. In the density-temperature regime relevant to giant planets with $M \lesssim M_{\rm J}$, MESA employs the Saumon et al. (1995) equation of state, interpolated over hydrogen's molecular-metallic phase transition such that the density varies smoothly between the two phases (SCvH-I). This EOS is advantageous for studies of helium phase separation because it provides the necessary state variables for arbitrary mixtures of hydrogen and helium, which is critical for solving the energy equation throughout the interior of the differentiating planet. This is one of our principal motivations for using SCvH-I over more recent H-He EOSs obtained with *ab initio* methods (e.g., Militzer & Hubbard 2013) in spite of the latter class comparing more favorably with shock experiments. Rosseland mean radiative opacities are taken from Freedman et al. (2008) and a privately communicated 2011 update. Electron conduction opacities are based on Cassisi et al. (2007).

Jupiter is oblate as a result of its rapid rotation, while our present models are

perfect spheres. A suitable mean planet radius with which to compare our model radii is the volumetric radius (Seidelmann et al. 2007)

$$R_{\rm vol} \equiv R_{\rm eq}^{2/3} R_{\rm pol}^{1/3} = 69,911 \pm 6 \text{ km}, \tag{2.1}$$

where $R_{\rm eq}$ and $R_{\rm pol}$ are Jupiter's equatorial and polar radii at 1 bar; $R_{\rm vol}$ is the radius of sphere enclosing the same volume as does Jupiter's 1-bar surface. Because the overall compactness of the planet is steeply sensitive to its heavy element mass, the high precision of this radius measurement translates into an extremely narrow range of allowed core masses. As an example, fitting the radius of our homogeneous, adiabatic Jupiter model—for which $M_{\rm c}$ is the sole free parameter—to Jupiter's $R_{\rm vol}$ at the solar age using MCMC produced $M_{\rm c} = (25.33 \pm 0.03)\ M_{\rm E}$ (the quoted value corresponding to the median and the error to the 68% confidence interval). Our models prefer large core masses because of the assumption that all heavy elements are relegated to a dense core; in reality, at least half of Jupiter's heavy element mass probably resides in the hydrogen-dominated mantle and envelope (Saumon & Guillot 2004). Thus in our findings (§2.3), $M_{\rm c}$ should be interpreted as a total heavy element mass. Indeed, the fact that our adopted equation of state is limited to hydrogen and helium is the reason why we make no effort to calculate the oblateness and associated gravitational multipole moments ($J_2,\ J_4,\ \ldots$) for our models.

The presence of heavy elements in the envelope and the action of rotation would both modify the hydrostatic structure and thus the total cooling time obtained for an evolutionary model. To assess the sensitivity to the heavy element distribution, we

computed models with fixed total heavy element mass $M_Z = M_c + M_{Z,env} = 28\ M_E$ and varying combinations of the core mass M_c and envelope heavy element content $M_{Z,env}$, modelling the heavy elements in the H-He envelope simply by taking $Y \rightarrow Y + Z$ for the purposes of this diagnostic. We find that models with more of their heavy elements mixed throughout the envelope cool more quickly (e.g., Baraffe et al. 2008a), with a characteristic spread of 70 Myr in the time for models with no H-He phase separation to cool to Jupiter's volumetric radius. This is a relatively short time compared to the $\sim 2 - 5 \times 10^8$ yr spread in cooling times obtained by varying the total heavy element content or atmospheric boundary condition, as discussed in §3. The centrifugal support provided by rotation would also modify the radius evolution, but as there are a number of complexities associated with rotation (e.g., the likely differential rotation as a function of radius or latitude, and the details of the planetary figure as a result of even rigid rotation), we do not model rotation here. It should be noted that the effect of rotation is to some degree degenerate with the total amount and distribution of heavy elements, since the tendency for centrifugal acceleration to prefer larger radii can be offset by incorporating more heavy elements.

2.2.1 Initial conditions

Adiabatic, extended (1-bar radius $R = 2\,R_J$) initial models of mass $M = M_J = 1.89861 \times 10^{30}$ g were created using MESA's `create_initial_model` capability described in Paxton et al. (2013). For each model, a fraction of the total mass was converted into a dense, nonevolving core of specified mass M_c and density ρ_c. All models in the present work adopt a constant core density $\rho_c = 15$ g cm^{-3} for simplicity.

The evolution is insensitive to the particular choice of core density; the total radius R is set by M_c nearly independent of ρ_c.

2.2.2 Hydrogen-helium phase separation

We couple our evolutionary calculations to the H-He phase diagram of Lorenzen et al. (2011), whose calculations include the simplifying assumption of ideal entropy of mixing between the two species. The group of Morales et al. (2013) instead performed direct thermodynamic integrations, thus including nonideal contributions to the entropy of mixing, but at the expense of subtantially more sparse sampling in helium number fraction x_{He}. The results of the two groups are in reasonable agreement, diverging most noticeably at temperatures $\lesssim 3000$ K, which on a present-day Jupiter (or Saturn) adiabat is well outside the transition from molecular to metallic hydrogen predicted by either group. Although it appears from their Figure 1 that the phase diagram of Morales et al. (2013) predicts that Jupiter has not yet cooled into the immiscibility region of (P, T) space for a protosolar mixture, the favored model of Hubbard & Militzer (2016b) has a cooler deep interior such that it has already undergone H-He phase separation according to both phase diagrams. These cooler deep layers are a result that Militzer et al. (2008) attributed to the important inclusion of the nonideal entropy of mixing between H and He.

Apart from the major differences in the two modern phase diagrams' behavior at $T \lesssim 3000$ K, $P \lesssim 1$ Mbar, their overall shapes at the warmer conditions relevant to Jupiter and Saturn are in rough agreement, with the major effect being an temperature offset (up to 1000 K) between the two. It is possible that this discrepancy stems from

including versus excluding the nonideal entropy of mixing between the two components. It was demonstrated by Nettelmann et al. (2015) that applying the raw phase diagram of Lorenzen et al. (2011) to Jupiter resulted in too large a loss of helium from the molecular envelope, motivating a global downward offset in the demixing temperature such that the onset of phase separation takes place later in the planet's history. It is reassuring that an offset motivated by Jupiter's observed atmospheric helium content brings the two phase diagrams into closer agreement. In this paper, we also allow for a global temperature offset $\Delta T_{\rm phase}$ to this phase diagram and estimate its value from available data; we confirm the result of Nettelmann et al. (2015) that for models computed with SCvH-I, the necessary downward offset is of order 200 K. Shifts to the published phase diagram in pressure are also conceivable, but as the phase diagrams of Lorenzen et al. (2011) and Morales et al. (2013) agree fairly closely on the minimum *pressure* for phase separation at temperatures typical of Jupiter and Saturn's molecular-metallic transitions, the temperature offset appears to be the most important correction.

The phase diagram of Lorenzen et al. (2011) adopted for the models in this paper is illustrated in Figure 2.1, wherein phase curves are shown in ($x_{\rm He}$, T) space (left panel) and in (P, T) space (right panel). The data are finely sampled in $x_{\rm He}$ but more coarsely in P, where data are available at $P = (1,\ 2,\ 4,\ 10,\ 24)$ Mbar. Our model assumes no phase separation at pressures lower than 1 Mbar where no data are available. This assumption is reasonable given the near-vertical (P, T) phase curves found by both Lorenzen et al. (2011) and Morales et al. (2013) for the relevant temperatures 4 kK $< T <$ 6 kK, although the latter phase diagram situates the boundary at slightly

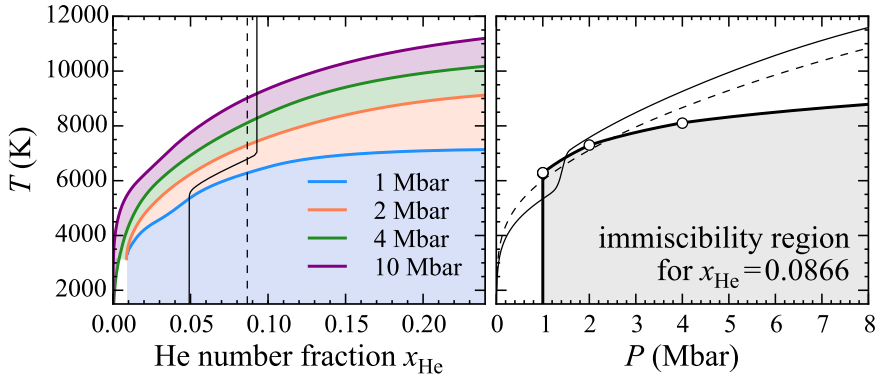

Figure 2.1: H-He phase diagram of Lorenzen et al. (2011), illustrating immiscibility regions as a function of helium number fraction $x_{\rm He}$ for four pressures (left panel), and as a function of pressure for the protosolar mixture (right panel). Immiscibility regions (shaded regions bounded by thick curves) are precluded in terms of equilibrium thermodynamics, i.e., by the criterion that the Gibbs free energy be stable with respect to perturbations in the helium concentration. The vertical dashed line in the left panel designates the protosolar mixture, $x_{\rm He} = 0.0866$ ($Y = 0.275$). Open circles in the right panel are raw data and the curve is a linear interpolation in $\log P$. A solar-age profile of a representative differentiated Jupiter ($M_{\rm c} = 30\,M_{\rm E}$, $R_\rho = 0.25$, $\Delta T_{\rm phase} = 0$) is shown in the thin black solid curves.

lower pressure $P \approx 0.8$ Mbar. To compute the equilibrium abundances for zones at arbitrary T and P, we interpolate in the tables linearly in $x_{\rm He}$ and $\log P$ to obtain $T_{\rm phase}$, and numerically solve the equation

$$T_{\rm phase}(x_{\rm He},\ P) + \Delta T_{\rm phase} - T = 0 \tag{2.2}$$

for the equilibrium helium concentration $x_{\rm He}$.

Differentiation begins once the planetary $P - T$ profile cools into the immiscibility region for the protosolar mixture, at which time one or more grid points are supersaturated in helium. For this and each subsequent timestep, we assume the thermodynamic equilibrium distribution of helium throughout the interior, which amounts

to the assumption that all helium excess is delivered efficiently by gravitational settling to lower depths such that it can exist in chemical equilibrium with its surroundings. Here "efficient" delivery means that the local supersaturation can be reduced to zero faster than the other relevant timescales, namely the planet's thermal timescale, the large-scale convective circulation time, and the simulation timestep.

The thermal timescale $\tau_{\rm th} = E_{\rm gr}/L$, with $E_{\rm gr}$ denoting the total binding energy, is roughly 10^9 yr. Timesteps in our simulations are typically 10^6 to 10^7 yr. The convective circulation time presents the strongest condition: it can be estimated with mixing length theory as (Guillot et al. 2004) $\tau_{\rm MLT} \sim 10^8$ s, or 3 yr. Stevenson & Salpeter (1977b) derived the minimum size a He-rich droplet would need to attain in order for its terminal speed to exceed the average speed of convective motions of the ambient fluid. Balancing the terminal speed from a turbulent drag law with an average convective speed estimated from mixing length theory, those authors obtained a minimum droplet length scale on the order of 1 cm. Repeating their calculation, we balance the (downward) buoyancy force with a drag force through a convective plume:

$$\Delta\rho d^3 g \approx C\rho d^2 v^2, \tag{2.3}$$

where $\Delta\rho$ is the density excess compared to the surrounding H-dominated fluid, d is the length scale of the droplet, C is a nondimensional drag coefficient, and v is the relative speed between the droplet and the medium. A minimum droplet size $d_{\rm min}$ corresponds

to a droplet having $v = v_{\rm MLT}$ so that

$$d_{\rm min} \approx \frac{C\rho v_{\rm MLT}^2}{\Delta\rho g}, \tag{2.4}$$

where $v_{\rm MLT} \approx 10$ cm s^{-1}, $\Delta\rho \approx \rho$, and $g \approx 3 \times 10^3$ cm s^2. If as in Stevenson & Salpeter (1977b) we assume turbulent flow over the scale of a droplet (Re $\equiv vd/\nu \gtrsim 10^3$), then $C = 0.5$ (Landau & Lifshitz 1959) and we arrive at a smaller minimum size $d_{\rm min} \approx 10^{-2}$ cm; the discrepancy may be the result of a dimensional error in the earlier calculation. However, given a typical kinematic viscosity $\nu = 4 \times 10^{-3}$ cm^2 s^{-1} (French et al. 2012), the Reynolds number Re $\equiv ud/\nu \approx 25$ so that a turbulent drag force is not appropriate. If instead we balance buoyancy with a Stokes drag appropriate for low Reynolds number, then (Landau & Lifshitz 1959)

$$\Delta\rho d_{\rm min}^3 g \approx 6\pi d_{\rm min}\rho v_{\rm MLT}\nu \tag{2.5}$$

and we obtain

$$d_{\rm min} = \left(\frac{6\pi\nu v_{\rm MLT}}{g}\right)^{1/2} \approx 10^{-2} \text{ cm}, \tag{2.6}$$

incidentally the same estimate as in the turbulent case.

Again following Stevenson & Salpeter (1977b), this droplet size can be translated into a droplet formation timescale if we suppose that the droplets grow by microscopic diffusion of He nuclei into the He-rich pockets. Assuming the microscopic diffusivity $D_{\rm He}$ to be of order the He-He self-diffusion coefficient obtained in the recent

ab initio simulations by French et al. (2012), the timescale to form a sinkable droplet is

$$\tau_{\text{sedimentation}} = \frac{d_{\text{min}}^2}{D_{\text{He}}} = \frac{(10^{-2}\ \text{cm})^2}{10^{-3}\ \text{cm}^2\ \text{s}^{-1}} \approx 10^{-1}\ \text{s}. \tag{2.7}$$

The strong hierarchy in timescales

$$\tau_{\text{sedimentation}} \ll \tau_{\text{MLT}} \ll \tau_{\text{th}} \tag{2.8}$$

implies that the transport of excess helium toward the center of the planet is probably efficient in spite of convection (or double-diffusive convection, which mixes material over much longer timescales), so assuming the equilibrium mixture throughout the planet at each timestep is an adequate starting point for evolutionary models.

For all timesteps in which a cell has been cooled below its critical temperature, we lower the abundance of the outermost supersaturated grid point (i.e., the first grid point with $P > 1$ Mbar) to its equilibrium value. We apply this same equilibrium abundance throughout the molecular envelope, reflecting the fact that outside of regions where phase separation is taking place, the species are being rapidly mixed by convection. Since a single timestep corresponds to millions of large-scale convection cycles, the entire molecular envelope acts as a reservoir of helium for the phase separation and rainout taking place near the molecular-metallic transition. The molecular envelope thus depletes uniformly in a given step.

Iterating inward over grid points, we enforce the local equilibrium abundance (a monotonically increasing function of depth) in each cell, and propose that same

abundance as the tentative (He-enriched) mixture to be applied to the remainder of the metallic interior. Eventually, a grid point is reached whose equilibrium abundance is greater than or equal to its proposed abundance. At this point the inward iteration ceases and the homogeneous, He-enriched interior is stable to phase separation; all that remains is to enforce conservation of helium overall. The proposed profile always has a helium deficit, which is resolved by the constraint that all helium nuclei that have rained out from above are mixed into the homogeneous interior; we raise the helium abundance of the homogeneous interior accordingly. Since this adjustment typically leaves the uppermost layers in the homogeneous interior marginally supersaturated, we repeat the iteration over all grid points as many times as necessary to achieve the equilibrium profile. In practice this takes one or two more iterations.

2.2.3 Modes of heat transport

The pioneering work of Hubbard (1968, 1969, 1970) made the case for Jupiter's envelope as a convective fluid of primarily hydrogen and helium. The short mean free path of photons and electrons in the interior imply a small thermal conductivity, with the result that convection, rather than radiation or conduction, carries nearly all the intrinsic flux. The temperature gradient is thus marginally superadiabatic; estimates from mixing length theory yield $\nabla - \nabla_{\rm ad} \lesssim 10^{-6}$ throughout the envelope and $\nabla - \nabla_{\rm ad} \lesssim 10^{-9}$ within hydrogen's molecular-metallic phase transition at megabar pressures. Our homogeneous Jupiter models indicate that convection maintains these small superadiabaticities to within an order of magnitude over the history of the planet with the exception of an early, brief radiative window similar to that described by Guillot et al. (1995).

As demonstrated by Guillot et al. (2004), the inclusion of alkali metals enhances the opacity enough to ensure convection at all depths within a present-day Jupiter. Our models, which include modern opacities and self-consistently allow for radiative transport wherever $\nabla_{\rm rad} < \nabla_{\rm ad}$, confirm this result: the intermediate radiative window is only mildly subadiabatic ($\nabla - \nabla_{\rm ad} \sim -10^{-1}$) and vanishes before $t \sim 2 \times 10^8$ yr (see also Fortney et al. 2011), and has an insignificant effect on the overall cooling time. Thus for the homogeneous phases of the evolution, our models may be directly compared to models constructed assuming $\nabla = \nabla_{\rm ad}$ always.

In the more general case allowing for stratification in the mean molecular weight μ, the Schwarzschild & Härm (1958) criterion for dynamical convection

$$\nabla > \nabla_{\rm ad} \tag{2.9}$$

must be replaced by the Ledoux (1947) criterion

$$\nabla > \nabla_{\rm ad} + \frac{\varphi}{\delta} \nabla_\mu, \tag{2.10}$$

where

$$\nabla_\mu \equiv \frac{d \ln \mu}{d \ln P} \tag{2.11}$$

is the slope of the mean molecular weight μ along the planetary profile, and φ and δ are two thermodynamic derivatives defined by

$$\varphi = \left(\frac{\partial \ln \rho}{\partial \ln \mu} \right)_{P,T}, \quad \delta = - \left(\frac{\partial \ln \rho}{\partial \ln T} \right)_{P,\mu}. \tag{2.12}$$

(Details on the novel calculation of $(\varphi/\delta)\nabla_\mu$ in MESA are given in Paxton et al. 2013 §3.3). If mean molecular weight increases toward the planet's center, as is the case for a differentiated planet, then $\nabla_\mu > 0$ and the regime

$$\nabla_{\rm ad} < \nabla < \nabla_{\rm ad} + \frac{\varphi}{\delta}\nabla_\mu \tag{2.13}$$

corresponds to the situation wherein a superadiabatic temperature profile is dynamically stabilized by the chemical stratification. The mixing that ensues in this regime is termed "semiconvection" in the stellar context (Schwarzschild & Härm 1958; Sweigart & Gross 1974) and "double-diffusive convection" in the hydrodynamic context (Turner 1974). In this case the Brünt-Väisälä frequency N of the fluid is real-valued, admitting gravity waves. These modes are in general overstable if fluid parcels can exchange a significant fraction of their heat with the environment over an oscillation period. The linear stability analysis of Kato (1966) demonstrated that in the stellar case, where radiative diffusion is efficient, the thermal diffusion timescale tends to be short compared to buoyant oscillation periods $N^{-1/2}$ so that the criterion for convective instability reduces to Equation 2.9 and marginally superadiabatic temperature gradients can be sustained by convection. Stevenson (1979) came to the same conclusion, arguing that the otherwise weak vertical heat transport provided by these overstable oscillations is mitigated by the occasional breaking of waves (Rosenblum et al. 2011), redistributing solute such that $\nabla = \nabla_{\rm ad}$ to a good approximation.

Metallic hydrogen environments in cool giant planets differ from the stellar case for two reasons: (i) the formation, rainout, and deeper redissolution of helium

droplets tends to enforce a persistent, stabilizing composition gradient, and (ii) since the (conduction-limited) diffusion of heat is quite inefficient, overstable gravity waves have relatively slow growth rates so that wave-breaking events are rare and the fluid is only weakly turbulent; vertical heat transport is thus enhanced relative to the purely diffusive case but is still much weaker than in the case of overturning convection. The resulting temperature gradient is substantially superadiabatic, possibly closer to the Ledoux limit $\nabla = \nabla_{\rm ad} + (\varphi/\delta)\nabla_\mu$ (Stevenson 1979; Mirouh et al. 2012).

2.2.4 A parametric model for double-diffusive convection

We assume the temperature gradient ∇ to be adiabatic unless there exists a stabilizing composition gradient $\nabla_\mu > 0$, in which case the temperature gradient is steeper than the adiabat by an amount proportional to ∇_μ, i.e.,

$$\nabla = \nabla_{\rm ad} + R_\rho \frac{\varphi}{\delta}\nabla_\mu \iff R_\rho = \frac{\nabla - \nabla_{\rm ad}}{(\varphi/\delta)\nabla_\mu}. \tag{2.14}$$

Equation 2.14 defines the density ratio R_ρ, which describes the relative (and competing) contributions that the temperature and composition stratifications make to the overall density stratification. We take R_ρ as a free parameter that we seek to estimate. Although the commonly cited criterion of Equation 2.13 is a necessary condition for semiconvection, it is not sufficient; the linear instability demands the somewhat more strict criterion (Walin 1964; Kato 1966)

$$1 > R_\rho > \frac{\mathrm{Pr} + \tau}{\mathrm{Pr} + 1} \equiv R_{\rm crit}. \tag{2.15}$$

Thus for the semiconvective instability to grow, the temperature gradient must be superadiabatic by a nonvanishing amount determined by the Prandtl number Pr and diffusivity ratio τ defined by

$$\mathrm{Pr} = \frac{\nu}{\kappa_T}, \qquad \tau = \frac{\kappa_\mu}{\kappa_T}, \tag{2.16}$$

where ν is the fluid's kinematic viscosity, κ_T is its thermal diffusivity, and κ_μ is the diffusivity of solute, in this case the diffusivity of helium atoms in a mixture which is predominantly metallic hydrogen. In Figure 2.2 we show values of Pr, τ, and R_{crit}, derived from the *ab initio* transport properties obtained by French et al. (2012) for a Jupiter adiabat. Here the calculation of τ (and thus R_{crit}) assumes an effective composition diffusivity κ_μ that is of order the He-He self-diffusion coefficient reported in that paper. The values of R_{crit} indicate that overstable modes can grow at 1 Mbar and deeper for density ratios $R_\rho > 10^{-1}$.

2.2.5 Energetics of evolving compositions

Enriching or depleting a Lagrangian fluid element in helium generally modifies its internal energy per gram u and does work modifying its density ρ following the fundamental thermodynamic relation

$$T\frac{ds}{dt} = \frac{du}{dt} + P\frac{d(1/\rho)}{dt}, \tag{2.17}$$

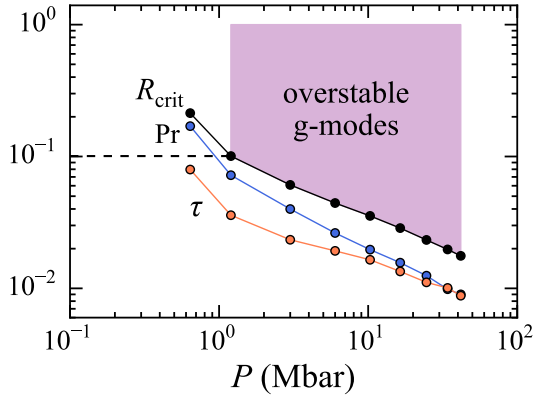

Figure 2.2: Estimates of the dimensionless quantities Pr and τ (Equation 2.16), as well as the critical density ratio $R_{\rm crit}$ for overstable double-diffusive convection (Equation 2.15). Quantities are derived from the *ab initio* transport properties of French et al. (2012) for the metallic hydrogen part of Jupiter's interior. The shaded region is the intersection of $R_{\rm crit} < R_\rho < 1$ and $P > 1$ Mbar, within which the stable stratification from helium rain admits growing-amplitude gravity waves and thus some degree of double-diffusive convection.

where s is the entropy per gram and d/dt denotes a time derivative. This change in heat content is commensurate with the energy gained or lost by the fluid element via photons:

$$\frac{dL}{dm} = -T\frac{ds}{dt} \tag{2.18a}$$

$$= -\frac{du}{dt} - P\frac{d(1/\rho)}{dt}. \tag{2.18b}$$

Here L is the local luminosity and m is the Lagrangian coordinate; other energy sources and sinks (nuclear fusion or fission, tidal dissipation, neutrino cooling) are negligible for our application. While the two forms of the energy equation Eqs. 2.18a and 2.18b are fundamental, MESA's solvers do not work with the entropy directly, and also do not work with $(u,\ \rho)$ by default (although the latter option exists). In either of the two

standard thermodynamic bases ($\rho,\ T$) or ($P,\ T$), these two variables (along with m, r, and X_i) are solved for simultaneously and then s or u are computed from the EOS post-hoc. Because s or u are not solved for directly, their finite differences over time are subject to numerical noise, and direct finite differences of either form 2.18a or 2.18b thus yield noisy luminosity profiles. The approach MESA takes by default is to instead recast Equation 2.18 into time derivatives of the quantities comprising the adopted thermodynamic basis. Since the phase diagram of Lorenzen et al. (2011) provides the equilibrium helium abundance over ($P,\ T$) space, and these are also the independent variables in the Saumon et al. (1995) EOS, we choose to adopt ($\ln P,\ \ln T$) as the thermodynamic basis for our MESA calculations. In this basis the energy equation takes the form (Paxton et al. 2013)

$$\left.\frac{dL}{dm}\right|_{X_i} = -c_P T \left(\frac{d\ln T}{dt} - \nabla_{\rm ad}\frac{d\ln P}{dt}\right), \tag{2.19}$$

where we have assumed radiation pressure is negligible as is appropriate for $T \lesssim 10^4$ K.

The standard transformation of Equation 2.18 into Equation 2.19 (e.g., Kippenhahn & Weigert 1990) ignores the fact that entropy and internal energy depend not only on P and T but also on the composition vector X_i, and hence Equation 2.19 is only accurate at fixed composition. This poses no substantial problem for energy conservation in stellar models, where large abundance changes typically only happen as a result of fusion, in which case nuclear energy generation overwhelms the $T(ds/dt)$ term in the energy equation; one important exception is the accretion of material with a composition different from the stellar surface. For our application, it is necessary to

add to Equation 2.19 the component of dL/dm that arises from composition changes at fixed P and T:

$$\left.\frac{dL}{dm}\right|_{P,\ T} = -\frac{\partial u}{\partial X_i}\frac{dX_i}{dt} - P\frac{\partial(1/\rho)}{\partial X_i}\frac{dX_i}{dt}. \tag{2.20}$$

Here the repeated indices denote summation over species $i = 1,\ \ldots,\ N-1$ where N is the total number of species in the model. (Since all N mass fractions sum to unity, only $N-1$ mass fractions are independent.) All models in this work assume a two-component mixture of ^{1}H and ^{4}He, so that Equation 2.20 reduces to just

$$\left.\frac{dL}{dm}\right|_{P,\ T} = -\frac{\partial u}{\partial Y}\frac{dY}{dt} - P\frac{\partial(1/\rho)}{\partial Y}\frac{dY}{dt}. \tag{2.21}$$

In practice we calculate this term for each cell as

$$\begin{aligned}\left.\frac{dL}{dm}\right|_{P,T} = &-\frac{u(P,T,Y_0) - u(P,T,Y_1)}{\Delta t} \\ &- P\left(\frac{\rho^{-1}(P,T,Y_0) - \rho^{-1}(P,T,Y_1)}{\Delta t}\right)\end{aligned} \tag{2.22}$$

where Y_0 and Y_1 denote the helium mass fractions before and after our helium redistribution step, and Δt denotes the (finite) timestep. Obtaining $u(P,T,Y_1)$ and $\rho^{-1}(P,T,Y_1)$ requires one additional call to the EOS module per zone per timestep.

2.2.6 Model atmospheres

The overall cooling time of an evolutionary giant planet model depends strongly on the boundary condition applied at the atmosphere, since that condition determines how rapidly the planet can radiate. We apply the self-consistent model atmospheres of

Fortney et al. (2011) as fit analytically by Leconte & Chabrier (2013a), which provide the temperature at the 10 bar level T_{10} as a function of surface gravity g and intrinsic temperature $T_{\rm int}$. The planet's effective temperature $T_{\rm eff}$ in a given timestep is given by

$$T_{\rm eff}^4 = T_{\rm int}^4 + T_{\rm eq}^4, \tag{2.23}$$

where the equilibrium temperature $T_{\rm eq}$ describes the orbit-averaged temperature of a body radiating as much energy as it absorbs from the Sun following

$$\sigma T_{\rm eq}^4 = \frac{(1-A)L}{16\pi a^2}, \tag{2.24}$$

with L the instantaneous luminosity of the star and a the planet's orbital semimajor axis. Effective temperatures for our models are calculated assuming the value for A determined by Voyager measurements in the infrared (Hanel et al. 1981b; Pearl & Conrath 1991). Although the planet's albedo is certainly a function of time as a result of changing atmospheric dynamics and chemistry (Hubbard & Smoluchowski 1973), assuming the present-day value of the albedo throughout the evolution is an acceptable (and at this stage necessary) approximation.

While Voyager 1 measured a Bond albedo $A = 0.343 \pm 0.032$, corresponding to $T_{\rm eq} = 109.9 \pm 1.3$ K, Pearl & Conrath (1991) noted that the value of A determined using Voyager 2 radiometry is larger than that determined by Voyager 1 by roughly 12%. As those authors suggested, if this discrepancy is the result of unidentified systematic error such that the true value is $6 \pm 6\%$ larger than the Voyager 1 measurement, then a revised

estimate for Jupiter's Bond albedo is $A = 0.366 \pm 0.035$. This corresponds to a modestly smaller equilibrium temperature $T_{\rm eq} = 108.5 \pm 1.4$ K. In the present work we adopt the median equilibrium temperature $T_{\rm eq} = 109.0$ K of the two Voyager determinations as ground truth. In §2.3.2 we also show our full calculations repeated with $T_{\rm eq}$ as a free parameter to address the broad modeling uncertainties—principally those associated with the EOS—that contribute to the uncertain overall cooling time for a contracting giant planet.

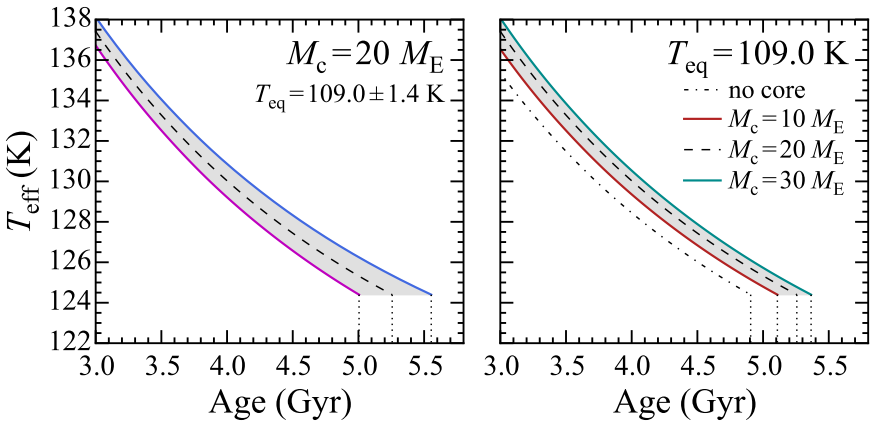

Figure 2.3: Sensitivity of the cooling time to the surface boundary condition (left panel) and heavy-element mass (right panel) for homogeneous, adiabatic Jupiter models. The dashed curve corresponds to $T_{\rm eq} = 109.0$ K, and the blue (magenta) curve corresponds to plus (minus) $\sigma_{T_{\rm eq}} = 1.4$ K.

2.3 Results of Evolutionary Calculations

We first validate our general modeling approach and implementation of the model atmospheres by computing homogeneous, adiabatic evolutionary sequences. Figure 2.3 shows evolution in the age-$T_{\rm eff}$ plane for models with core masses between 0 and

30 $M_{\rm E}$ and a range of assumed equilibrium temperatures reprensenting the uncertainty in the Voyager determination of Jupiter's Bond albedo. Models with higher equilibrium temperatures generally take longer to cool because they absorb more stellar flux, and models with greater heavy element content generally cool faster because they are more compact. Figure 2.4 provides a summary of cooling times attainable by homogeneous models across $M_{\rm c} - T_{\rm eq}$ parameter space, and demonstrates that over the cooling time depends more steeply on the atmospheric boundary condition than on the assumed heavy element mass. The total cooling times agree closely with published results also using the SCvH-I EOS (Fortney & Hubbard 2003; Saumon & Guillot 2004; Fortney et al. 2011).

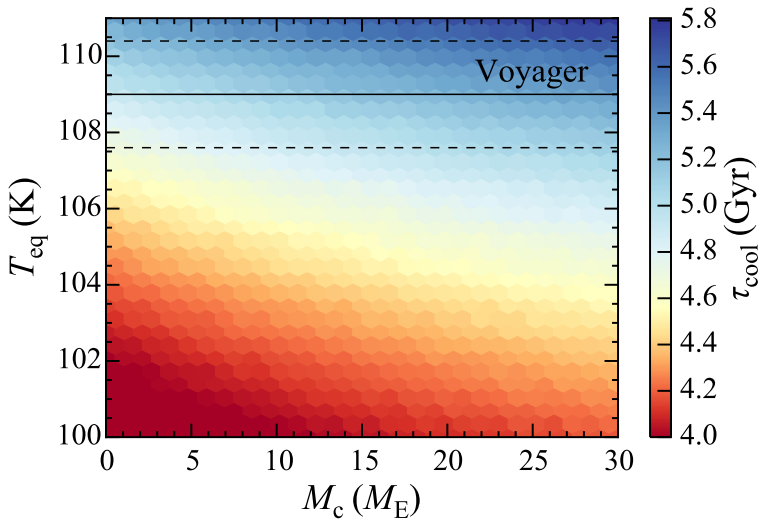

Figure 2.4: Time for homogeneous 1.0 $M_{\rm J}$ models to cool to Jupiter's $T_{\rm eff}$ as a function of their heavy-element mass $M_{\rm c}$ and equilibrium temperature $T_{\rm eq}$. The horizontal lines designate the Voyager measurement of $T_{\rm eq}$ (see §2.2.6). The color scale is piecewise linear such that yellow corresponds to the solar age 4.56 Gyr.

The SCvH-I EOS generally leads to slow cooling for the homogeneous models.

These were evolved to Jupiter's observed $T_{\rm eff}$ = 124.4 K, a temperature notably not reached within the age of the solar system (4.56 Gyr) for any of the models, even those with vanishing heavy element mass. It is clear that whatever superadiabaticity arises from helium rain in the inhomogeneous case must act to *accelerate* the planet's cooling in spite of any additional luminosity associated with differentiation. This is the first indication that inhomogeneous models computed with the SCvH-I equation of state will tend to favor fairly weak heat transport in the helium gradient region such that the temperature distribution is strongly superadiabatic and a thermal boundary layer is established. As described by Stevenson & Salpeter (1977b), in this case the molecular envelope can cool rapidly while the cooling of the deeper interior is stalled or even reversed. Indeed, sections 2.3.1 and 2.3.2 below demonstrate that best-fitting models have a steep enough temperature gradient in the stable region that the cooling of the molecular envelope is accelerated while the helium-enriched metallic interior is heated over time.

Some more recent equations of state based on *ab initio* methods (e.g., Militzer & Hubbard 2013) yield adiabats which are colder at Mbar pressures and Jupiter- and Saturn-like entropies than the adiabats obtained from the semianalytic model of Saumon et al. (1995). These "colder" equations of state compare more favorably with shock experiment, and generally predict shorter cooling times for homogeneous Jupiters because their adiabats have less total internal energy for a given global entropy. With such an EOS, if inhomogeneous evolution is to help with addressing Jupiter's luminosity constraint, then any double-diffusive convection in the deep interior must act to *lengthen*

the cooling relative to the homogeneous case. Thus for a "colder" equation of state, more modest superadiabaticities should be expected such that the differentiation luminosity overwhelms the accelerated cooling of the envelope due to the double-diffusive bottleneck at 1-2 Mbar. This situation is closer to the luminosity problem for Saturn, where the drastic underluminosity of homogeneous models is robust with respect to the assumed equation of state. In §2.3.1 we illustrate the central role that the efficiency of heat transport by ODDC plays in determining the thermal evolution. In §2.3.2 we retrieve strong superadiabaticities for our nominal SCvH-I case. Then to address the systematic modelling uncertainty associated with the H-He equation of state, we repeat our calculations with $T_{\rm eq}$ taken as a fourth free parameter to modulate the overall cooling time, with high (low) $T_{\rm eq}$ mimicking the effect of a warmer (colder) equation of state.

2.3.1 Inhomogeneous evolution

Interior profiles for Jupiter models undergoing helium rain are illustrated in Figure 2.5 for four different values of R_ρ, including the adiabatic case $R_\rho = 0$. (In the case of evolving composition profiles, $\nabla_{\rm ad} = \nabla_{\rm ad}(P,\ T,\ X_i)$ where the X_i are now functions of depth. We refer to the case where $\nabla = \nabla_{\rm ad}$ everywhere as adiabatic, although the profiles are emphatically not isentropic.) For this figure and all others in this section, unless otherwise indicated, the two remaining free parameters are arbitrarily chosen as $M_{\rm c} = 30\ M_{\rm E}$ and $\Delta T_{\rm phase} = 0$ K for illustrative purposes. The first column shows profiles at 3.5 Gyr, at which time helium rain has not yet commenced and the models are thus still in an identical state. The remaining three panels show profiles

shortly after the onset of helium rain (3.8 Gyr), then at a more typical time after helium rain onset (4.0 Gyr), and finally at the solar age (4.56 Gyr). The inset in the center left panel plots $T_{\rm eff}$ as a function of age for the four models.

Evolution in the adiabatic case $R_\rho = 0$ is simplest because there is minimal feedback between the evolving composition and temperature profiles, and thus the shape of $L(m)$ can be understood by inspecting just the composition term of dL/dm (Equation 2.21); the thermal term retains essentially the same smooth profile as before helium rain sets in. The layers with decreasing helium abundance—from the planetary surface down to the lower boundary of the helium gradient region—have an *increasing* internal energy u and specific volume $1/\rho$, and thus $dL/dm < 0$ there. Similarly, layers deeper than the bottom of the gradient region have a uniformly increasing helium abundance and thus $dL/dm > 0$ there. Hence, a global maximum in the luminosity is attained at the base of the gradient region. The adiabatic model also exhibits the most extended helium gradient region among the models considered (spanning 1 to 2.4 Mbar at the solar age), simply because a shallower $T(P)$ profile intersects the immiscibility gap over a broader range in pressure. Likewise, larger values of R_ρ represent steeper $T(P)$ profiles, which generally intersect the immiscibility gap over a more narrow range in pressure. This can be seen by comparing the two solar-age profiles in the right panel of Figure 2.1, and is manifested in the relative widths of the features in Y and ∇ in Figure 2.5.

The evolution is more complex in the case of nonzero superadiabaticity $R_\rho > 0$, owing to the feedback between the composition profile and the temperature profile. Since in this case the settling of helium directly modifies $T(P)$ via Equation 2.14, it

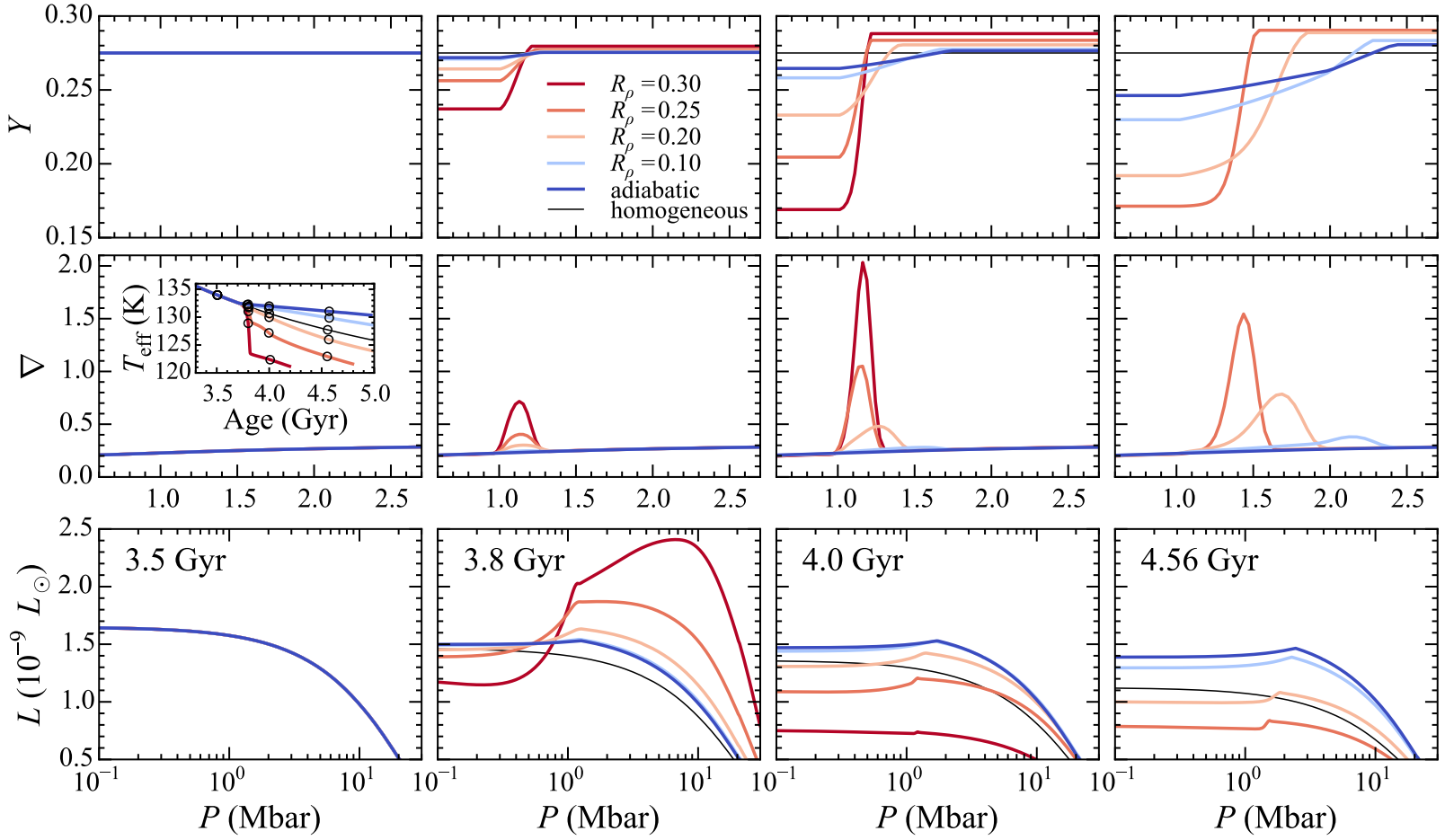

Figure 2.5: Interior profiles for differentiating Jupiter models. Shown are the helium mass fraction Y (top row), the temperature gradient $\nabla \equiv d\ln T/d\ln P$ (middle row; see Equation 2.14) and local luminosity L (bottom row) as functions of pressure for 1.0 $M_{\rm J}$ models with $M_{\rm c} = 30$ $M_{\rm E}$ and $\Delta T_{\rm phase} = 0$ K, for four different values of the fractional superadiabaticity R_ρ: 0.20 (light orange), 0.25 (dark orange), 0.30 (red), and the adiabatic case $R_\rho = 0$ (blue). Thin black curves show a model with no phase separation for reference. The four columns correspond to four points in model age as labeled in text in the lower panels, and as indicated by the open circles in the inset in the center left panel. To emphasize detail, the first two rows show Y and ∇ over a different pressure scale than the luminosity panels.

contributes to both the thermal (Equation 2.19) and composition (Equation 2.21) components of dL/dm. For cases with $R_\rho \gtrsim 0.20$, double-diffusive convection poses a sufficiently strong thermal barrier that the homogeneous, adiabatic deep interior actually heats up with time, and the reduced heat flux impinging on the bottom of the molecular envelope allows the envelope to cool relatively quickly. The temperature evolution in the vicinity of the helium gradient is illustrated for these same four values of R_ρ in Figure 2.6, and Figure 2.7 shows the evolution of the core-mantle boundary in $T - \rho$ space. Indeed since a more pronounced temperature contrast over the helium gradient region drives a steeper composition gradient as per the phase diagram, a runaway effect ensues, with $T_{\rm eff}$ and $Y_{\rm atm}$ plummeting as stronger stratifications are realized. In the most extreme case shown here ($R_\rho = 0.30$), the effective temperature decreases by 8 K over 10^8 yr in this phase, to be compared to the roughly 1 K per 10^8 yr cooling rate before the onset of helium rain. After roughly a thermal time for the homogeneous interior, the gradient region feels significant heating from below, quenching the runaway and once again assuming a state of slow evolution in which the surface cools by roughly 1 K per Gyr.

The effect of translating the phase curve in temperature is summarized in Figures 2.7 and 2.8, which show evolutionary tracks for two families of models, one with the phase diagram unmodified (solid curves) and one with a representative offset of $\Delta T_{\rm phase} = -230$ K for illustration purposes (dashed curves). The crossing of the two families of curves in Figure 2.8 demonstrates the fundamental anticorrelation between R_ρ and $\Delta T_{\rm phase}$. For instance, an effective temperature of 124 K at 4.56 Gyr can be realized

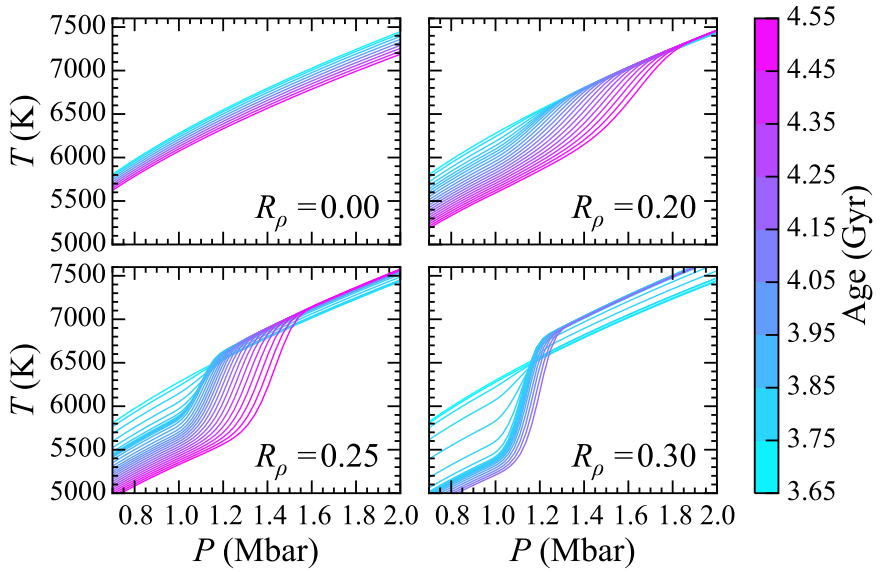

Figure 2.6: Evolution of the interior temperature profile for differentiating Jupiter models (the same models as in Figure 2.5). Each panel plots a time sequence of profiles for the model indicated. Color maps to model age.

either by a model with relatively modest superadiabaticity using the unmodified phase diagram, or by a model with a more extreme superadiabaticity and a delayed helium rain onset. However, the offset of $\Delta T_{\rm phase} = -230$ K delays the onset of helium rain by nearly 800 Myr and consequently leads to a more modest depletion of helium from the molecular envelope by the time the model reaches the solar age. As demonstrated by Nettelmann et al. (2015) and discussed in §2.2 above, a downward offset of roughly this magnitude must be applied to the Lorenzen et al. (2011) phase diagram to yield values of $Y_{\rm atm}$ at the solar age which are consistent with the *Galileo* entry probe measurement (Table 2.1). Lastly, we note that translating the phase diagram to lower temperatures also leads to a more localized helium gradient region, the $\Delta T_{\rm phase} = -230$ K case yielding a gradient roughly 1/3 the geometric thickness of the gradient established in

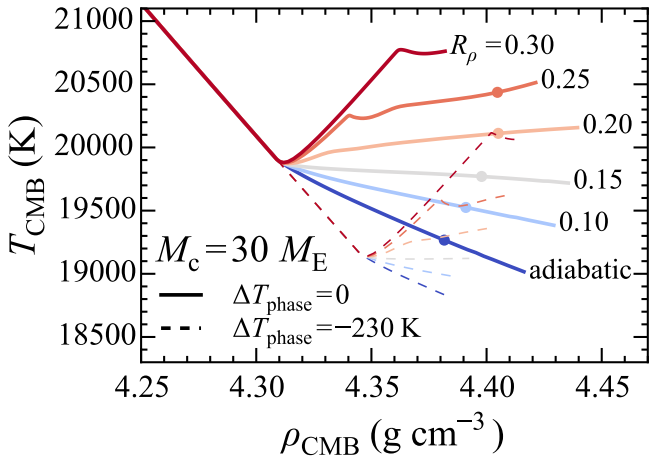

Figure 2.7: Evolution of the temperature and density at the core-mantle boundary (the innermost grid point in our simulations) for six different values of the superadiabaticity R_ρ of the temperature profile in the helium gradient region. The two families of curves are for two representative temperature offsets applied to the H-He phase diagram: the solid tracks assume $\Delta T_{\rm phase} = 0$; the dashed tracks assume $\Delta T_{\rm phase} = -230$ K. For each model with $\Delta T_{\rm phase} = 0$ that reaches the solar age, that point is indicated with a filled circle.

the $\Delta T_{\rm phase} = 0$ case for each of the R_ρ values considered here. In the following section, we leave $\Delta T_{\rm phase}$ as a free parameter alongside $M_{\rm c}$ and R_ρ and systematically estimate all three simultaneously by fitting Jupiter's $T_{\rm eff}$ and $Y_{\rm atm}$ along with its volumetric radius $R_{\rm vol}$.

2.3.2 Bayesian Parameter Estimation

We estimate model parameters and their statistical uncertainties using Markov chain Monte Carlo (MCMC). In particular, given our nonlinear three-parameter model

$$\theta \equiv \{M_{\rm c},\ R_\rho,\ \Delta T_{\rm phase}\} \tag{2.25}$$

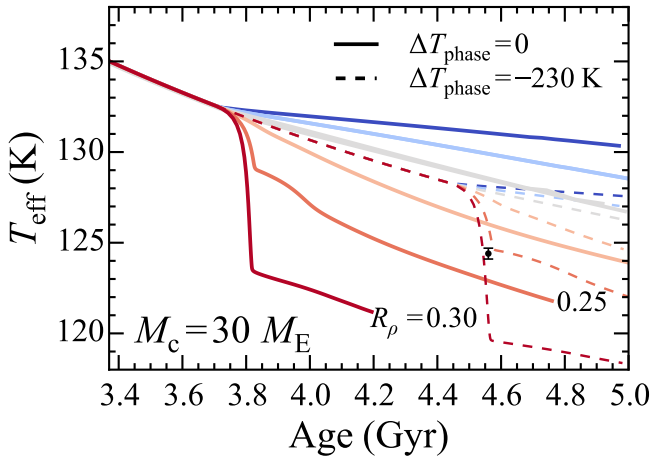

Figure 2.8: As in Figure 2.7, but showing the effective temperatures as a function of age. The marker shows Jupiter's observed $T_{\rm eff}$ at the solar age.

and fundamental Jupiter data (see Table 2.1)

$$D \equiv \{T_{\rm eff},\ Y_{\rm atm},\ R_{\rm vol}\}, \tag{2.26}$$

we calculate the posterior probability distribution from Bayes' theorem

$$P(\theta|D) \propto P(D|\theta)P(\theta). \tag{2.27}$$

In the likelihood $P(D|\theta)$ we assume Gaussian errors for the data D:

$$\begin{aligned}\ln P(D|\theta) = -\frac{1}{2}\Big[&\ln(2\pi\sigma^2_{T_{\rm eff}}) + \frac{(T_{\rm eff}-T^{\rm m}_{\rm eff})^2}{\sigma^2_{T_{\rm eff}}} \\ &+ \ln(2\pi\sigma^2_{Y_{\rm atm}}) + \frac{(Y_{\rm atm}-Y^{\rm m}_{\rm atm})^2}{\sigma^2_{Y_{\rm atm}}} \\ &+ \ln(2\pi\sigma^2_{R_{\rm vol}}) + \frac{(R_{\rm vol}-R^{\rm m})^2}{\sigma^2_{R_{\rm vol}}}\Big],\end{aligned} \tag{2.28}$$

Table 2.1: Jupiter evolutionary constraints

Age (yr)	$T_{\rm eq}$ (K)	$T_{\rm eff}$ (K)	$Y_{\rm atm}$	$R_{\rm vol}$ (km)
4.56×10^9	109.0[a]	124.4 ± 0.3[b]	0.234 ± 0.005[c]	$69,911 \pm 6$[d]

[a] §2.2.6

[b] Hanel et al. (1981b)

[c] von Zahn et al. (1998)

[c] Seidelmann et al. (2007)

where a superscript m denotes the model outcome at the solar age; each sample from the posterior distribution thus entails a full evolutionary calculation. Samples are drawn from the posterior distribution Equation 2.27 using the Python MCMC implementation `emcee` (Foreman-Mackey et al. 2013). Our prior probability distribution $P(\theta)$ is chosen to be uniform over $M_{\rm c} \geq 0$, all $\Delta T_{\rm phase}$, and $0.1 \leq R_\rho \leq 1$ following the criteria for linear instability (see §2.2.3, in particular Equation 2.15); elsewhere it is zero.

The late evolution of $T_{\rm eff}$, $Y_{\rm atm}$ and R for the a subset of the evolutionary sequences in the resulting chain are shown in Figure 2.9, which color codes tracks by their value of R_ρ. For the duration of the initial homogeneous phase, the differences in $T_{\rm eff}$ and R between tracks stem solely from the heavy element core mass $M_{\rm c}$, since that parameter adjusts the mean density and hence the total radius of the planet. As described in §2.3.1, the time at which phase separation sets in (and $Y_{\rm atm}$ first diverges from the protosolar value) is set by $\Delta T_{\rm phase}$, and the trend toward later phase separation onset with increasing R_ρ is the result of the two parameters' substantial covariance. Timesteps spanning the solar age are typically 10^7 yr, and the values of $T_{\rm eff}$, $Y_{\rm atm}$ and R were interpolated linearly within those timesteps to obtain $T_{\rm eff}^{\rm m}$, $Y_{\rm atm}^{\rm m}$, and $R^{\rm m}$.

Proposed steps in which the model terminated before the solar age (as would be expected for a model with simultaneously large R_ρ and $\Delta T_{\rm phase}$, for example) were rejected, since a calculation of the likelihood (Equation 2.28) would not be possible.

The models that terminate before 5 Gyr did so either because (i) the model cooled to $T_{\rm eff} = 120$ K, at which point we stop to avoid unnecessary computation time, or (ii) upon the onset of phase separation, the luminosity inversion described in the previous subsection (and evident in the $R_\rho = 0.30$ case in Figure 2.5) grew to the degree that a negative luminosity was realized in the interior, typically just outside the helium gradient region. This behavior follows from attempting to enforce large values of R_ρ such that the the large luminosity generated by deposition of helium into the metallic interior cannot be communicated upward through the weakly turbulent double-diffusive layer. Nettelmann et al. (2015) identified the same effect in their models with LDDC, noting that there exists a minimum layer height such that the luminosity is still positive throughout the interior. In our models this translates to an effective upper limit on the values of R_ρ attainable by models with strictly positive luminosity profiles.

The outcome of our Bayesian parameter estimation is the posterior probability distribution shown in Figure 2.10, wherein each panel plots the full joint distribution marginalized over the other two parameters. The medians of each distribution are indicated, as are the central 68% confidence regions. Typical models (as characterized by the medians) have massive cores ($M_{\rm c} = 27.7\ M_{\rm E}$), are strongly superadiabatic in the compositionally stratified region ($R_\rho = 0.31$), and have substantial downward offsets to the phase diagram ($\Delta T_{\rm phase} = -235$ K.) The posterior distribution of $\Delta T_{\rm phase}$ is nar-

rowly peaked at these large negative offsets, and quite robustly rules out the unmodified phase diagram. This result is driven by the requirement that the model's homogeneous molecular envelope retains enough helium to match the modest depletion measured by the *Galileo* entry probe (Table 2.1).

The single largest modeling uncertainty for the cooling of the giant planets is associated with the equation of state. Depending on the assumed EOS, Saumon & Guillot (2004) found that cooling times for homogeneous Jupiter models spanned 3.1 to 5.4 Gyr. (For comparison, our homogeneous models with SCvH-I cool in 5 to 5.5 Gyr for realistic heavy element masses and equilibrium temperatures; see Figures 2.3 and 2.4.) The range in cooling times obtained from applying different equations of state owes mostly to the fact that for different $P(T)$ relations, models with a given entropy possess different total thermal energy content and hence take more or less time to cool to Jupiter's present-day luminosity.

As a means of exploring how our results would be affected by the application of a different equation of state, we repeat our full calculations with a modified atmospheric boundary condition. Although the model atmosphere and equation of state are not directly related, they are degenerate in that they both dictate the overall timescale for the thermal evolution. This can be made explicit by first integrating the energy equation (equation 2.18a) over the mass of the planet to yield

$$L_{\rm int} = -\int_0^M T\frac{ds}{dt}\,dm = 4\pi R^2 \sigma_{\rm SB}\left(T_{\rm eff}^4 - T_{\rm eq}^4\right). \tag{2.29}$$

For the simplified example of a planet cooling through a sequence of isentropes, ds/dt

is independent of m and the second equality can be integrated to yield the total cooling time

$$\tau_{\rm cool} = \int_0^{\tau_{\rm cool}} dt = \int_{s_{\rm cool}}^{s_0} \left(\frac{\int_0^M T(m,s)\, dm}{4\pi R^2(s) \sigma_{\rm SB} \left(T_{\rm eff}^4(s) - T_{\rm eq}^4 \right)} \right) ds, \tag{2.30}$$

where s_0 designates an arbitrary large starting entropy, $s_{\rm cool}$ designates the planet's current entropy, and other symbols have their usual meanings. Equation 2.30, while emphatically not how our evolutionary sequences are calculated, serves as a heuristic tool to demonstrate that choosing a colder EOS (such that the mean temperature along a given adiabat is lower) and reducing the solar input $T_{\rm eq}$ have a similar effect.

Our modification of the boundary condition as a proxy for a different H-He EOS is motivated by the lack of other realistic EOS options presently available in MESA at the relevant densities and temperatures. Varying the parameter $T_{\rm eq}$ offers a simple means of producing a different total cooling time, the relation between the two being illustrated in Figure 2.4. As an example, we find that a homogeneous, adiabatic model with $M_{\rm c} = 30\ M_{\rm E}$ and $T_{\rm eq}$ reduced to 100 K cools to Jupiter's $T_{\rm eff}$ in just 4.2 Gyr. Since very large superadiabaticities tend to reduce the cooling (see Figure 2.8), differentiating models that satisfy the basic constraints of Table 2.1 in spite of a cold boundary condition must have small values for R_ρ such that the cooling is extended to the age of the solar system.

Figure 2.11 shows the late evolution of models computed with this artificially free boundary condition, with a uniform prior chosen for $T_{\rm eq}$; the posterior distributions of $M_{\rm c}$, R_ρ, $\Delta T_{\rm phase}$ and $T_{\rm eq}$ are shown in Figure 2.12. In this case the extra freedom in the boundary condition leads to a wide variety of total times spent in the homogeneous

phase of evolution, and consequently the other parameters M_c, R_ρ and $\Delta T_{\rm phase}$ have markedly wider posterior probability distributions. Most likely models have equilibrium temperatures several K cooler than the measured value $T_{\rm eq} = 109$ K such that the homogeneous cooling is more short-lived, and in the inhomogeneous evolution that follows, double-diffusive convection can proceed with temperature gradients closer to the adiabat and still satisfy the $T_{\rm eff}$ constraint at the solar age. Indeed, the models display an overall preference for the lowest possible density ratios; the marginalized posterior probability density increases uniformly toward lower values of R_ρ and peaks at the lower boundary imposed by the step-function prior $R_\rho > R_{\rm crit} = 0.1$, which was imposed in light of the linear criterion for the double-diffusive instability (see §2.2.4). As a result, the most likely evolution during the inhomogeneous phase is secular cooling of the envelope, with no dropoff of the surface temperature or helium abundance over short timescales. These models might be considered preferable to the most likely models obtained in the three-parameter case of Figures 2.9 and 2.10 because if $T_{\rm eff}$, $Y_{\rm atm}$, and $R_{\rm vol}$ were undergoing drastic changes on a 10^8 year timescale, then observing Jupiter in its present state would be somewhat serendipitous.

Freeing $T_{\rm eq}$ also allows much more modest corrections to the phase diagram, the 68% credible interval now spanning -200 to -100 K. Importantly, despite the freedom in the overall cooling time, the unmodified phase diagram is still found to be extremely unlikely with 95% of probability lying at offsets $\Delta T_{\rm phase} < -50$ K.

The posterior distribution of $T_{\rm eq}$ values in Figure 2.12 should not be interpreted as a new determination of Jupiter's $T_{\rm eq}$, as that is a measured quantity. Rather,

it contains information about a most likely equation of state: it is significant that the distribution excludes the measured value almost completely, with only 0.4% of cumulative probability within the error of the measurement (Table 2.1). If we suppose that our model contains the essential physics, this can be taken as evidence that the real EOS for hydrogen and helium predicts substantially colder interiors than does SCvH-I. For reference, a homogeneous evolutionary sequence computed with the median values $M_{\rm c} = 28.8\ M_{\rm E}$ and $T_{\rm eq} = 102.9$ K from the distributions in Figure 2.12 cools to Jupiter's $T_{\rm eff}$ in 4.46 Gyr (see Figure 2.4).

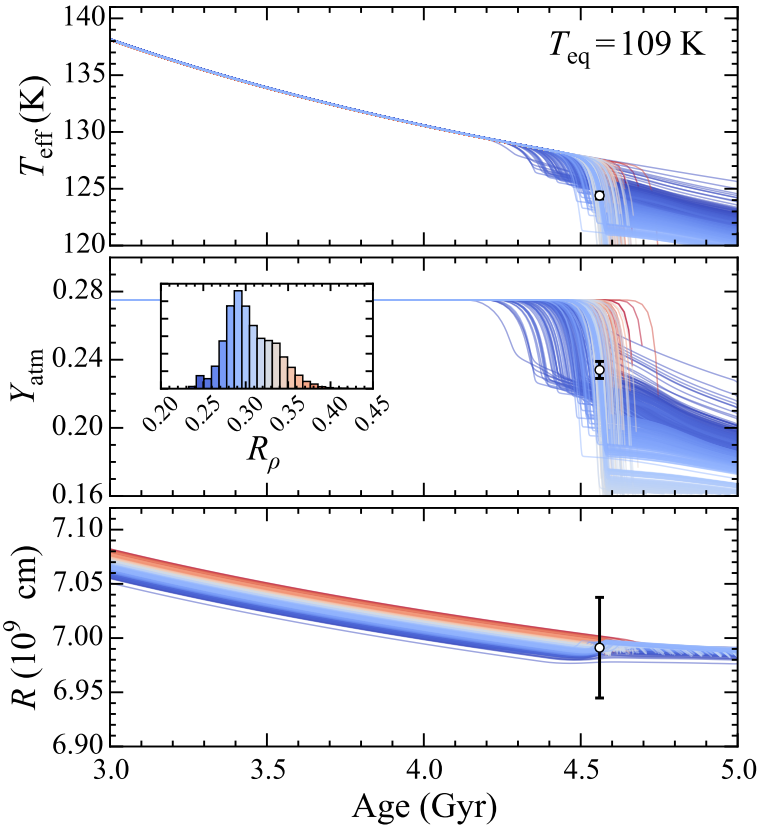

Figure 2.9: Late evolution of Jupiter models undergoing helium rain and overstable double-diffusive convection, sampled using MCMC. Open circles with error bars designate observations (Table 2.1); the error on $T_{\rm eff}$ is smaller than the marker. The color of an evolutionary a track encodes its R_ρ value as specified by the colors of the bars in the histogram (inset, center panel), which is a coarsely binned version of the marginalized posterior probability distribution in Figure 2.10. Only a random subset of tracks are shown, and more likely tracks are plotted on top of less likely ones.

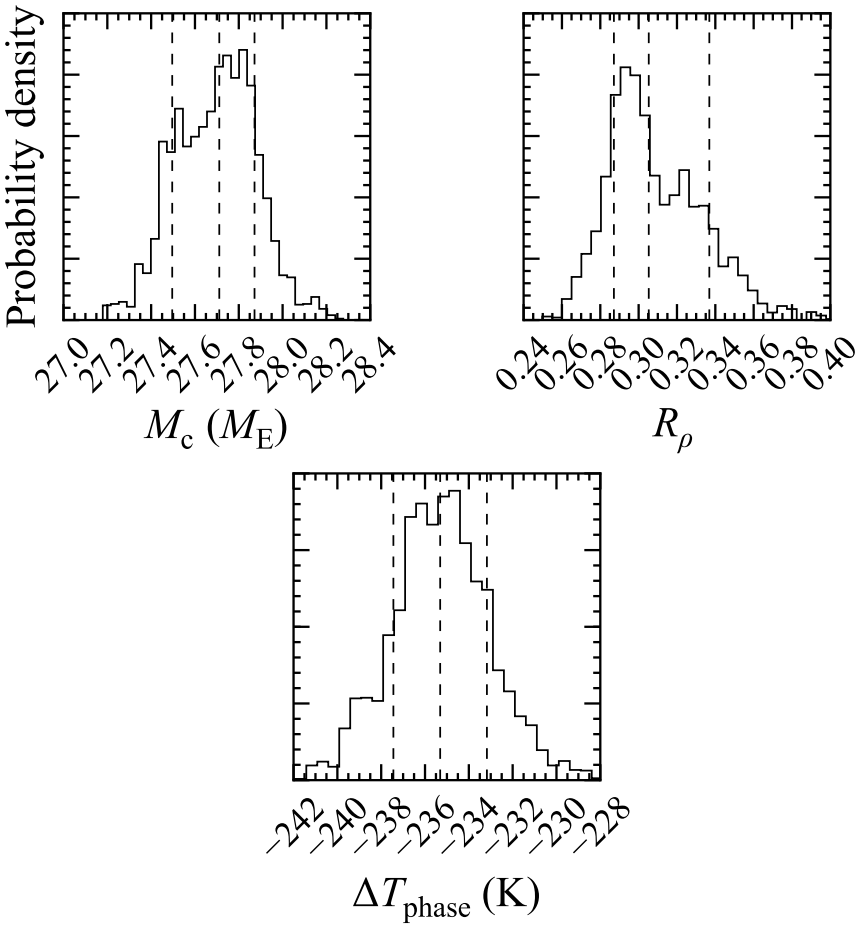

Figure 2.10: Posterior probability distributions for the heavy element mass $M_{\rm c}$, density ratio R_ρ in the helium gradient region, and phase diagram offset $\Delta T_{\rm phase}$ based on the evolutionary sequences shown in Figure 2.9. Each distribution is the full three-dimensional joint distribution marginalized over the other two parameters. The vertical dashed line near each peak designates the median, with the flanking vertical dashed lines enclosing the central 68% of cumulative probability.

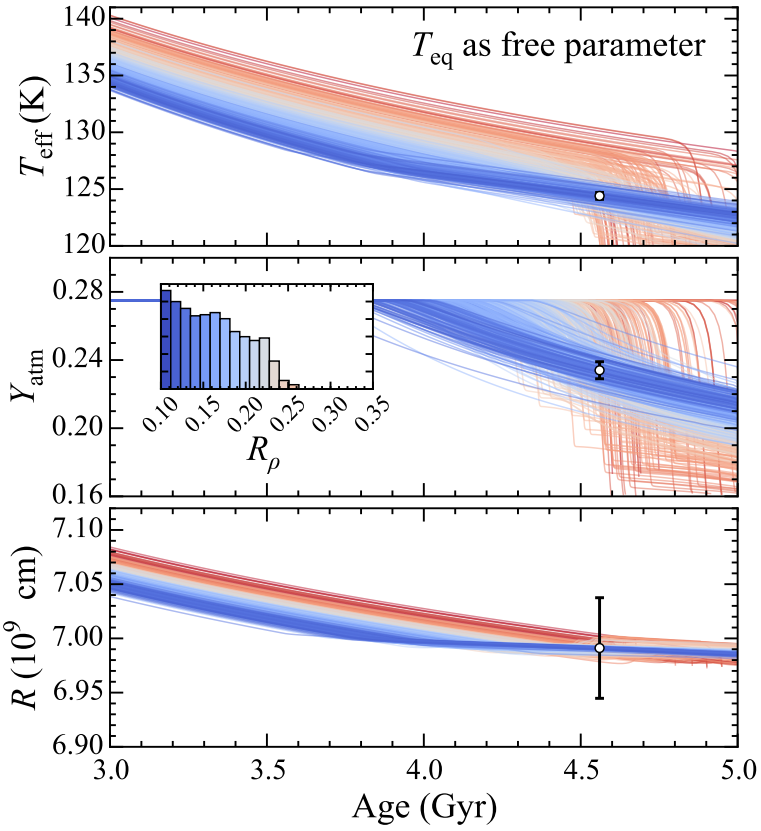

Figure 2.11: As in Figure 2.9, but including T_{eq} as a additional free parameter to mimic the effect of an EOS predicting a warmer or colder interior.

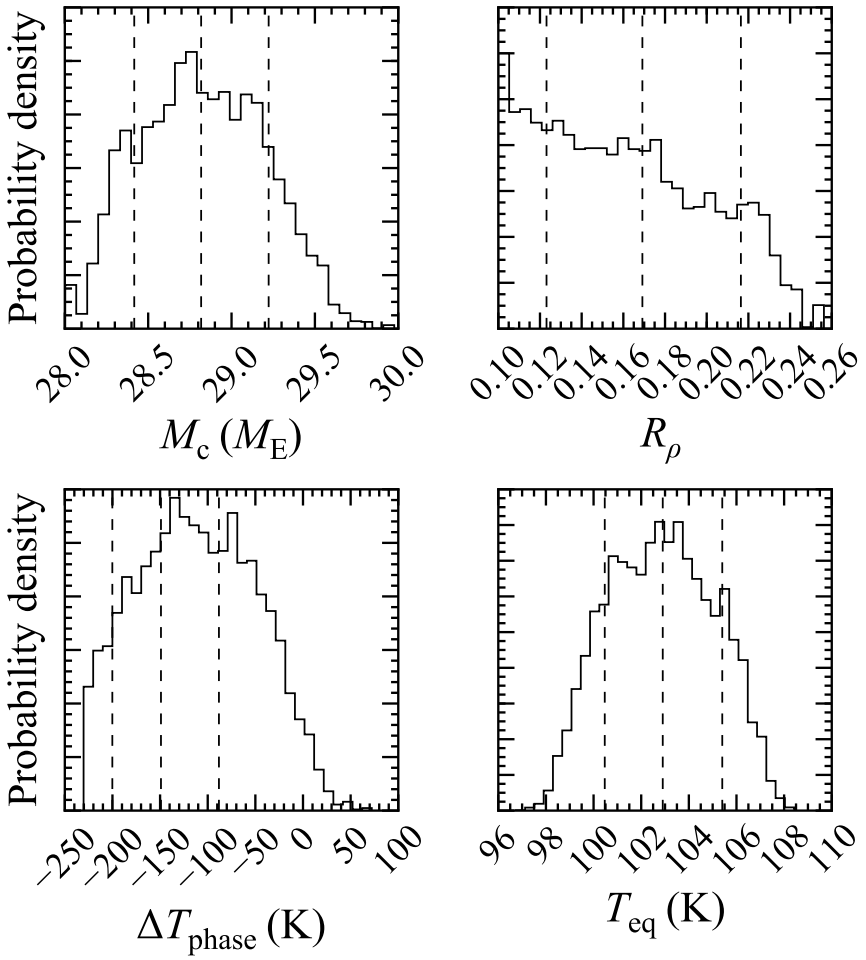

Figure 2.12: As in Figure 2.10, but including $T_{\rm eq}$ as an additional free parameter to mimic the effect of an EOS predicting a warmer or colder interior.

2.4 Discussion

The framework developed here consists of a Python class for creating instances of MESA work directories, modifying MESA inlists, executing the evolution program, and processing its output, all as part of a single likelihood calculation called by an `emcee` sampler. The method renders it straightforward to add additional parameters to the model or incorporate new or updated constraints in any quantity output by MESA directly. It is readily adaptable to a host of different problems, most obviously non-adiabatic thermal evolution models for Saturn, where the same fundamental physics operate. Beyond just the Jovian planets and H-He immiscibility, our technique has broad applicability for deriving properties of objects from giant planets to brown dwarfs and stars, e.g., retrieving the age and composition for an object with measured mass and radius. Performing these retrievals with a code as mature as MESA means that our knowledge of stellar/planetary evolution is built in, including complexities such as self-consistently determining mixing boundaries, modeling double-diffusive transport processes, or calculating nuclear energy generation rates with state of the art nuclear networks. Thus in the example of retrieving an object's composition and age from its measured mass and radius, meaningful inferences can be made about not just the bulk composition, but the composition profile, and indeed the composition profile's possible origins and evolution. The Bayesian approach automatically provides meaningful error bars for model parameters, and combining it with the open source MESA package offers more flexibility than traditional grid-based isochrone fitting because new parameters—and indeed new physics—can be added at will.

This work builds on that of Nettelmann et al. (2015) principally in two ways: first, it makes the weakest possible assumption about the temperature gradient resulting from double-diffusive convection in the deep interior, abandoning the assumption of layered convection following the flux laws derived by Wood et al. (2013) in favor of a generic model wherein any temperature gradient can be attained as long as it is consistent with the criterion for linearly overstable gravity waves. Second, performing the calculations in an MCMC framework allows a probabilistic determination of all model parameters simultaneously, and we find a multitude of models that satisfy the imposed constraints (Table 2.1). We demonstrated that SCvH-I predicts strongly superadiabatic temperature profiles in Jupiter's helium gradient region, such that the planet's surface cools rapidly as most of the metallic hydrogen interior heats up over time. Repeating the calculations with a variable boundary condition to probe the effects of using a different EOS, we found that more modest superadiabaticities are preferred, although the distribution of allowed values is still broad. We found in all cases that the unperturbed phase diagram of Lorenzen et al. (2011) is highly unlikely.

That such a diversity of models meeting the imposed constraints were obtained in Figures 2.11 and 2.12 underscores the severe uncertainties that persist in modelling the evolution of giant planets. Admittedly, the present work does not exploit all the available data. Most importantly, our models make no use of of Jupiter's gravitational harmonics or its axial moment of inertia, both of which constrain the interior density profile. As discussed in §2.2, a calculation of oblateness and the associated non-spherical components of the gravity field is beyond our scope because the only EOS currently

available for modeling giant planets in MESA, SCvH-I, is limited to hydrogen and helium. All heavy elements are in an inert core rather than partially distributed through the envelope, and as such the density profiles in our models are somewhat unrealistic and are not suited for fitting to J_2 or any higher-order moments. Our models therefore also neglect the impact that the distribution of heavy elements has on convective stability, which may also play an important role in the thermal evolution of Jupiter and Saturn (Vazan et al. 2016a). Nonetheless, we view these models as complimentary to the detailed static models computing using more realistic equations of state (e.g., Hubbard & Militzer 2016b) in that we use a forward thermal evolution model to derive estimates for Jupiter's deep superadiabatic temperature stratification and corrections to the H-He phase diagram, both of which should be taken into consideration for improving static models of the Jovian planets. Our findings support the existing body of evidence indicating that a realistic H-He equation of state departs significantly from SCvH-I.

Chapter 3

Helium in the comparative evolution of Jupiter and Saturn

3.1 Introduction

Understanding the interiors of the gas giants is a critical step toward understanding the universal processes of planet formation and evolution. Jupiter and Saturn hold special significance in this respect because of their accessibility. However, outstanding puzzles concerning their thermal evolution obscure the connection between their present-day configurations and their origins in the young solar system. Evolutionary models treating Jupiter's interior as being well-mixed and nearly adiabatic as a result of efficient convection are broadly successful in explaining the planet's luminosity at the solar age (Graboske et al. 1975; Fortney et al. 2011). However, similar models for Saturn fail to reproduce its observed heat flow (Pollack et al. 1977; Grossman et al.

1980; Fortney et al. 2011), and thus some additional luminosity source is required.

Apart from the primary luminosity from cooling baryons (Hubbard 1968), differentiation has long been appreciated as a potentially significant luminosity source for cool gas giants (Smoluchowski 1967; Flasar 1973). In particular, the limited solubility of helium in fluid metallic hydrogen eventually leads to the formation of helium-rich droplets that may rain out on a timescale short compared to their convective redistribution (Salpeter 1973). As noted by Stevenson & Salpeter (1977a), the success of homogeneous, adiabatic Jupiter models implies that the planet has begun raining out helium only recently or not at all, whereas the differentiation is probably significant in the cooler Saturn. The helium depletion subsequently observed in Jupiter's atmosphere (von Zahn et al. 1998) suggests that the planet has indeed begun differentiating helium in the recent past.

The notion that helium rain can explain Saturn's luminosity is supported by evolutionary calculations including helium immiscibility for plausible, if tentative, phase diagrams (Hubbard et al. 1999; Fortney & Hubbard 2003). Leconte & Chabrier (2013b) imagined an important alternative scenario wherein significant departures from adiabaticity due to double-diffusive convection in Saturn's deep interior can also explain that planet's luminosity without recourse to helium immiscibility. However, given the direct evidence for helium differentiation in Jupiter, it appears difficult to avoid helium differentiation in the presumably[1] colder interior of Saturn.

Work in recent years has applied many of these ideas to the evolution of Jupiter

[1] For reference, although the baseline layered-convection Saturn model of Leconte & Chabrier shows a radically different cooling history from their adiabatic case, the two possess very similar deep temperatures at the solar age (their Figure 6), i.e., colder than Jupiter's.

(Nettelmann et al. 2015; Mankovich et al. 2016) and Saturn (Püstow et al. 2016). The main goal of the present work is to simultaneously study the evolution of Jupiter and Saturn under a single model for hydrogen-helium immiscibility to judge whether a consistent picture exists for their evolution. The motivation for doing this now is twofold. First, Jupiter's Bond albedo has recently been dramatically revised following analysis of multi-instrument *Cassini* data, indicating less absorbed solar flux and more internal flux emanating from Jupiter (Li et al. 2018) than long thought based on *Voyager* infrared measurements (Hanel et al. 1981a). This updated surface condition implies a greater flux contribution from the interior, potentially attributable to helium rain. The second motivation is the recent phase diagram of Schöttler & Redmer (2018), which builds on prior work (e.g., Lorenzen et al. 2011; Morales et al. 2013) by both including nonideal entropy effects and covering the full range of possible helium fractions. As will be discussed below, this knowledge of the phase diagram over all mixtures (from helium-poor to helium-rich) is of critical importance for modeling the helium distribution within Saturn. We aim to assess to what degree this proposed phase diagram is viable in the context of Jupiter's atmospheric helium content and Jupiter and Saturn's radius and heat flow at the present epoch.

3.2 Hydrogen-helium mixtures

The phase diagram that describes the solubility of helium in fluid metallic hydrogen is uncertain in Jovian interiors, a regime that is difficult to access experimentally. The phase diagram in this regime has been increasingly mapped out by *ab ini-*

tio methods, in particular density functional theory–molecular dynamics ("DFT-MD") simulations used to predict the thermodynamic conditions for helium phase separation. Advances along these lines have been made in recent years (Lorenzen et al. 2009, 2011; Morales et al. 2009, 2013; Schöttler & Redmer 2018), the results remaining substantially uncertain because they are sensitive to the assumed electron density functional and the accuracy with which the entropy of mixing between hydrogen and helium is treated.

As described by Morales et al. (2013), the nonideal contributions to this entropy of mixing is crucial for satisfying experimental results for molecular hydrogen, and strongly affects predictions for solubility in metallic hydrogen. Because the most recent studies of helium phase separation in the evolution of Jupiter (Nettelmann et al. 2015; Mankovich et al. 2016) and Saturn (Püstow et al. 2016) made use of results assuming an ideal mixing entropy (Lorenzen et al. 2011), the more accurate phase diagram of Schöttler & Redmer (2018) warrants a reappraisal of this type of model.

3.2.1 Modeling the interior helium distributions

The central assumption of the present work is that the helium distributions are dictated by their instantaneous thermodynamic equilibrium profiles. This amounts to the assumption that metallic regions cooled to the point of becoming supersaturated lose their excess helium instantaneously, reducing the ambient abundance to the saturation value while sinking the He-rich phase (typically $Y \approx 0.9$; see Figures 3.2 and 3.3) deeper into the planet where it redissolves into the background if possible. These ideas have already been described in the literature (Stevenson & Salpeter 1977b; Fortney & Hubbard 2003; Nettelmann et al. 2015; Püstow et al. 2016), and the algorithm we use

in practice is described in detail in Mankovich et al. (2016). The major differences from that work are the application of the Schöttler & Redmer (2018, hereafter "SR18") phase diagram and extension of these models to the case of Saturn.

3.2.2 The phase boundary is a surface $T(P, Y)$

The earlier DFT-MD simulations of Morales et al. (2013) did derive the full nonideal entropy of hydrogen-helium mixtures using thermodynamic integrations, and this phase diagram has previously been applied to detailed models for the *static structure* of Jupiter (Hubbard & Militzer 2016a) and Saturn (Iess et al. 2019). Its major limitation is its lack of coverage in mixture space, the published phase diagram being restricted to a single helium number fraction $x_{\mathrm{He}} = 8\%$ representing the protosolar helium abundance (ostensibly the mean abundance of the gaseous jovian envelopes). While this is appropriate for predicting whether and where phase separation will set in for a planet initially well mixed at the protosolar helium abundance, it does not generally yield enough information to calculate the resulting helium distributions in any detail.

The basic reason for this is that if a region becomes supercooled and loses its excess helium to greater depths via dense droplets, the local helium abundance decreases to the value satisfying exact saturation. Solving for this saturation abundance requires knowledge of the phase curves corresponding to *lower* abundances than the initial value. Take for example the homogeneous protosolar-abundance adiabats indicated in Figure 3.1, where they are compared to phase curves obtained by B-spline fits to the SR18 data. The warmest adiabat indicated by the dotted curve osculates the $Y = 0.27$

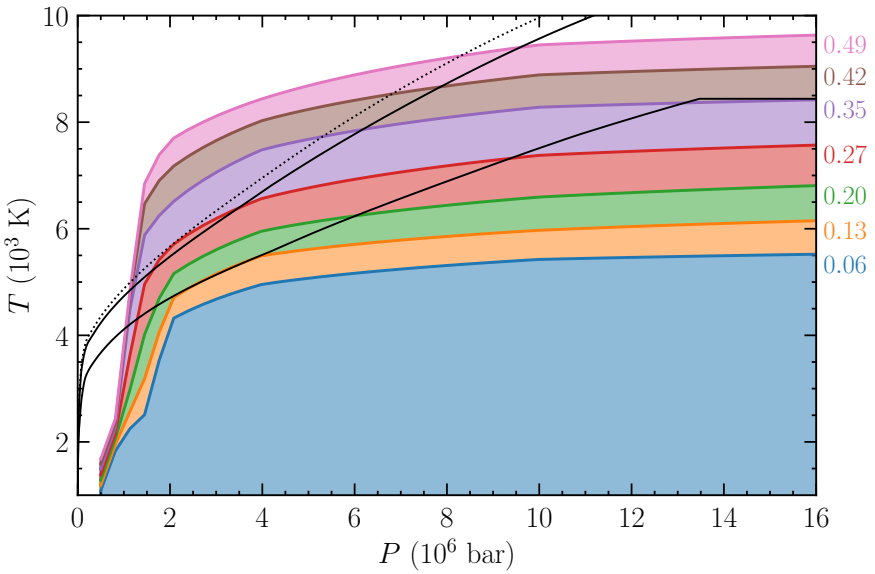

Figure 3.1: Phase curves from the *ab initio* hydrogen-helium phase diagram of Schöttler & Redmer (2018) compared with protosolar-abundance adiabats satisfying Jupiter or Saturn's observed T_1 and $T_{\rm eff}$ (solid black curves). Helium phase separation occurs in regions of the planet that cool beneath the pressure-temperature phase curve for the relevant local helium mass fraction Y, labeled to the right of each region. The diagram focuses on the helium-poor part of the phase diagram relevant for setting the helium content of a well-mixed molecular envelope in Jupiter or Saturn. A single hotter adiabat (dotted black curve) represents the onset of helium immiscibility.

phase curve at $P \approx 2$ Mbar and $T \approx 5500$ K, representing the moment that helium immiscibility sets in within the planet. From this point the initially well-mixed adiabat is supercooled in the neighborhood of $P \approx 2$ Mbar and this region will tend to lose its excess helium to lower depths via droplets. Exterior to this region, the molecular envelope is kept well-mixed by convection and thus the rainout process at $P \approx 2$ Mbar drains helium from exterior regions uniformly. The outer envelope abundance is thus given by the condition of saturation at $P \approx 2$ Mbar, i.e., the value of Y labeling the unique phase curve that osculates the planetary P–T profile there. Even without applying detailed models, visual inspection of Figure 3.1 reveals that this curve would correspond to Y between 0.20 and 0.27. Interpolating by eye, we may conclude that this phase diagram predicts an outer envelope abundance of $Y \approx 0.25$ for Jupiter. By the same reasoning, this phase diagram predicts an outer envelope abundance $Y \approx 0.13$ for Saturn.

Meanwhile at depth, droplets descending from above encounter increasingly warm surroundings, eventually redissolving into the medium (unless they reach the core or center of the planet first, a possibility discussed below). Here the helium abundance in the mixture increases. The question of whether this layer is itself now supersaturated requires knowledge of the phase curve at this *greater* local abundance. It becomes evident that, under the assumption that all excess helium is rained out to lower depths and redissolved at its first opportunity, solving for the equilibrium helium distribution throughout the interior is an iterative process that requires knowledge of the phase diagram at a potentially broad range of helium fractions. In other words, the deep

abundances are fundamentally not determined locally, and so the extent of the helium rain region cannot be determined from any single phase curve.

Jupiter's molecular envelope helium depletion relative to the protosolar abundance is modest, and the large mass ratio between Jupiter's metallic and molecular regions guarantees only a subtle helium enrichment of the deep interior. Saturn, on the other hand, has lower internal temperatures and so tends to suffer more dramatic differentiation of helium. At odds with Iess et al. (2019), we find that applying realistic phase diagrams to Saturn's present-day interior does not produce Jupiter-like helium distributions with a uniformly depleted molecular envelope that gradually transitions to a uniform, moderately enriched metallic envelope deeper down. As we will show below, we find that Saturn is cold enough that such an enriched inner envelope would itself be unstable to further phase separation when the phase diagram is queried at the correct (tentative, enriched) abundance.

Speaking in terms of an evolutionary path, we find that after immiscibility sets in, Saturn rapidly cools through a sequence of qualitatively Jupiter-like helium distributions until its helium gradient reaches the planet's dense core (or center, in the absence of such a core). After this point Saturn accumulates a shell (or core, if no core of denser material exists) of helium-rich material, an outcome of hydrogen-helium immiscibility discussed by Salpeter (1973) and Stevenson & Salpeter (1977a, their Figure 4c) and modeled explicitly by Fortney & Hubbard (2003) and Püstow et al. (2016). Figures 3.2 and 3.3 demonstrate this evolution path for our baseline Saturn model with helium rain.

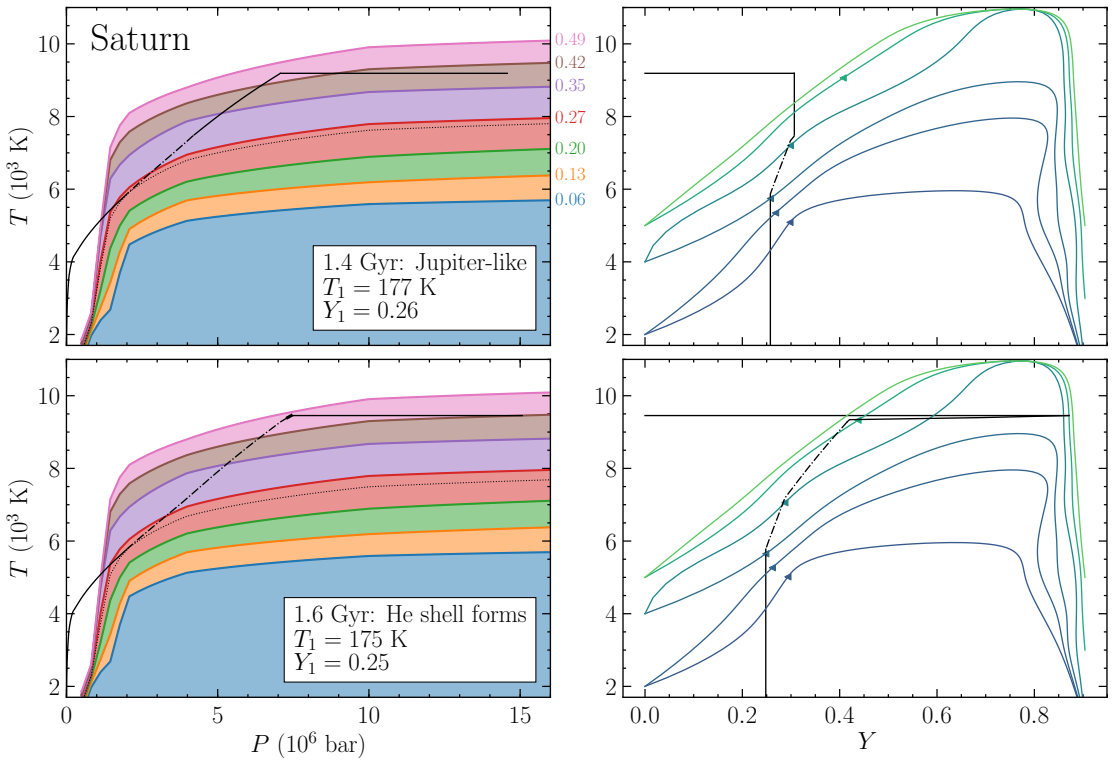

Figure 3.2: A typical sequence in evolutionary time (top to bottom) of Saturn interior profiles (black curves) superimposed with the SR18 phase curves. *Left panel:* P–T space, as in Figure 3.1. The dot-dashed portion of the planet profile indicates the continuous helium gradient region, and the thick portion indicates the extent of the helium-rich shell, when one exists. The thin dotted curve indicates the phase curve corresponding to the instantaneous outer envelope helium abundance. *Right panel:* the same Saturn profiles in Y–T space, with phase curves corresponding to $P = 1.2$, 1.5, 2, 4, 10, and 24 Mbar from bottom/blue to top/green. The triangle on each of these phase curves indicates the maximum Y in the helium-poor phase given the planet's current temperature at that pressure level. These values move to lower Y as the planet cools, driving the depletion in the outer envelope. At 1.6 Gyr the gradient region extends all the way down to the heavy-element ($Y = 0$) core, implying that helium-rich material falling from above no longer finds a warm homogeneous inner envelope in which to redissolve. From this time onward a the helium-rich ($Y \approx 0.87$) phase collects outside the core, establishing a dense shell. *(Sequence continued on the following page.)*

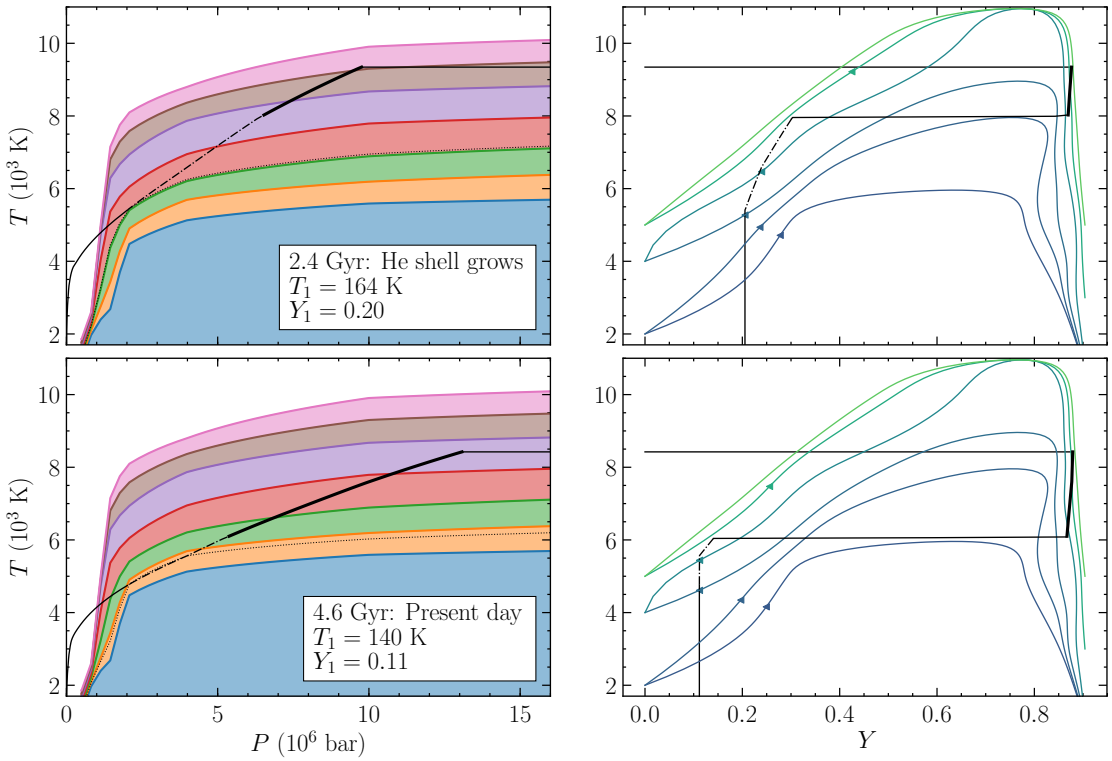

Figure 3.3: Evolution of a typical Saturn, continued from Figure 3.2.

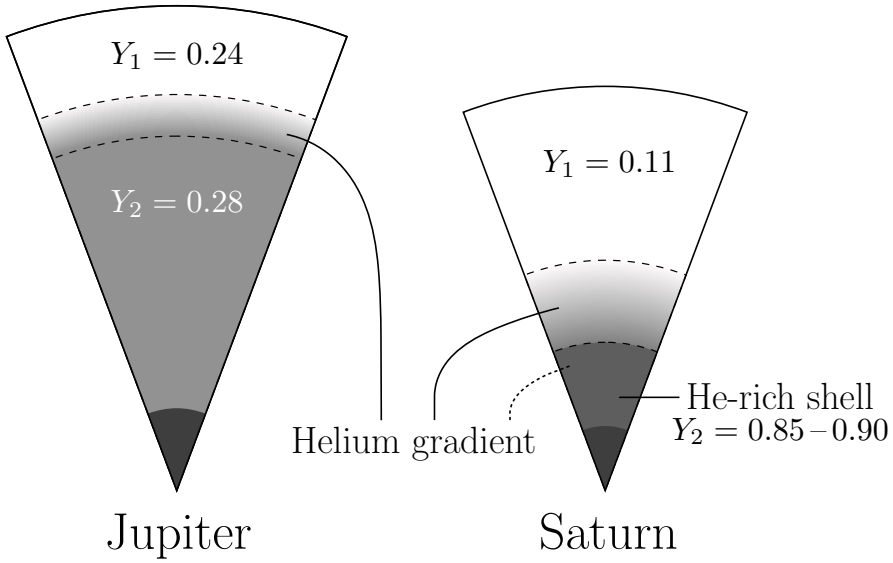

Figure 3.4: A schematic description of the present-day structures found for Jupiter and Saturn by applying the methods described in Section 3.2 and 3.3. Diagrams are to scale by radius, these specific structures corresponding to the most likely individual models from the favored samples described in Section 3.4. The dashed boundaries enclose the continuous helium gradient region within each planet. The outer boundaries at $\approx 80\%$ of Jupiter's radius and $\approx 55\%$ of Saturn's radius correspond to $P \approx 2$ Mbar where SR18 predicts the onset of hydrogen-helium immiscibility. The inner boundary at $\approx 35\%$ of Saturn's radius represents the transition to a shell of helium-rich material, discussed in Section 3.2. This shell itself possesses a weak helium gradient as can be seen from the right-hand panels of Figure 3.3.

To help guide the discussion that follows, Figure 3.4 show schematic diagrams for the present-day internal structures that we obtain for Jupiter and Saturn.

3.2.3 Overall temperature of the phase diagram

As discussed in Section 3.2.2 above, a preliminary comparison to a Jupiter adiabat reveals that SR18 predicts only subtle differentiation of helium in Jupiter. In particular the diagram predicts an atmospheric abundance $Y_1 \approx 0.25$, an overestimate relative to the abundance $Y_1 = 0.238 \pm 0.005$ measured by the *Galileo* entry probe

(von Zahn et al. 1998). This finding is consistent with Schöttler & Redmer (2018) who showed based on comparison to reference adiabats that this phase diagram predicts helium immiscibility to be marginal or even absent in Jupiter.

Assuming that hydrogen-helium immiscibility is the mechanism responsible for Jupiter's atmospheric helium depletion, the *Galileo* abundance measurement imposes a stringent constraint for discerning among viable, if still uncertain, phase diagrams. It is for this reason that, following Nettelmann et al. (2015) and Mankovich et al. (2016), we introduce a degree of freedom via an additive temperature offset $\Delta T_{\rm phase}$ modulating the overall temperature of the phase curves applied in this work, relative to SR18. This parameter allows us to explore a more general space of phase diagrams, with larger $\Delta T_{\rm phase}$ values leading to more pronounced differentiation, smaller values leading to less, and $\Delta T_{\rm phase} = 0$ recovering the SR18 phase curves as published. It also yields a convenient language of expressing our results in terms of belief about the "true" phase diagram based on how well our various thermal evolution models fare. Based on the discussion thus far, Jupiter models will require $\Delta T_{\rm phase} > 0$ to successfully match the *Galileo* helium abundance.

3.3 Gas giant evolution models

We create new evolutionary models for Jupiter and Saturn using a code derived from that of Thorngren et al. (2016) and recently applied to Saturn's static structure in Mankovich et al. (2019). The most significant update is the use of the *ab initio* hydrogen-helium equation of state (EOS) of (Militzer & Hubbard 2013, "MH13"), an

advance compared to the semianalytic model of Saumon et al. (1995) which predicted warmer metallic interiors for Jupiter and Saturn. MH13 provides data for a single mixture $Y = 0.245$. In this work EOS quantities are calculated for *arbitrary* hydrogen-helium mixtures by combining MH13 with the Saumon table for pure helium under the linear mixing approximation, as described and tabulated by Miguel et al. (2016). The influence of heavier elements is treated using the Rostock water EOS of French et al. (2009), also incorporated under the linear mixing approximation. The models in this work are initialized hot, with uniform envelopes containing a helium mass fraction $Y = 0.270$ corresponding to the protosolar value from Asplund et al. (2009). Rotation is neglected.

3.3.1 Rainout and convection

The internal flux in the models presented here is assumed to be carried purely by convection such that $\nabla = \nabla_{\rm ad}$ to a good approximation, except in cases where emergent helium gradients may partially stabilize the fluid against convection. (Here $\nabla \equiv \frac{{\rm d}\ln T}{{\rm d}\ln P}$ is the temperature gradient in the model and $\nabla_{\rm ad} \equiv \left(\frac{\partial \ln T}{\partial \ln P}\right)_s$ is the adiabatic gradient.) In such cases the double-diffusive instability may operate, and the ensuing nonlinear motions may establish superadiabatic temperature gradients $\nabla > \nabla_{\rm ad}$ consistent with a Schwarzschild-unstable, Ledoux-stable configuration.

The overall heat and compositional flux through such a configuration are sensitive to the microscopic diffusivities of heat and solute via the Prandtl number ${\rm Pr} = \nu/\kappa_{\rm T}$ and diffusivity ratio κ_μ/κ_T, where ν is the kinematic viscosity, κ_T is the thermal diffusivity set by electron conductions, and κ_μ is the diffusivity of solute. However, given

the likelihood that excess helium can aggregate by diffusion and rain out of the mixture quickly compared to convection timescales (Salpeter 1973; Stevenson & Salpeter 1977b), non-diffusive processes play an important role and it is not clear whether significant growth rates are achievable by overstable modes. In fact, if rainout of excess helium is fast even compared to the fluid's buoyancy period, then an adiabatically perturbed fluid parcel is perennially in equilibrium with its surroundings in terms of solute abundance. This lack of helium contrast between the parcel and its environment means that the buoyancy is no longer affected by helium gradients, and the condition for convective instability reduces back to the Schwarzschild criterion so that $\nabla \approx \nabla_{\rm ad}$ should be expected.

In lieu of any detailed understanding of how helium immiscibility affects the double-diffusive instability and associated secondary instabilities like layer formation (Mirouh et al. 2012; Wood et al. 2013), we apply the same simple, general model as in Mankovich et al. (2016). The temperature gradient is allowed to take on superadiabatic values in helium gradient regions, the value of the superadiabaticity assumed to be proportional to the magnitude of the helium gradient there following

$$\nabla - \nabla_{\rm ad} = R_\rho B \tag{3.1}$$

where the "density ratio" R_ρ (also labeled R_0 in the literature) is simply taken as a constant, introducing a free parameter in the model. Here B is the so-called Ledoux term accounting for the effect of composition gradients on the buoyancy frequency (e.g., Unno et al. 1989).

Regardless of their helium distributions, stabilizing Z gradients may be a general feature of gas giants as a result of the core accretion process (Helled & Stevenson 2017) or core miscibility (Wilson & Militzer 2012a,b), although outcomes in the latter vary widely depending on the stratification of the core boundary (Moll et al. 2017). If these heavy element gradients do exist, they generally dramatically affect the cooling history of the gas giants (Leconte & Chabrier 2013b; Vazan et al. 2015, 2016b, 2018) and thus deserve close attention. Nonetheless, for conceptual simplicity this work makes the strong assumption that the heavy elements are distributed trivially into a distinct $Z = 1$ core of chosen mass M_c and an envelope with uniform $Z = Z_1$. In this case the the only continuous composition gradients are in the helium mass fraction Y, and the term B of Equation 3.1 reduces to

$$B = \frac{\chi_\rho}{\chi_T} \left(\frac{\partial \ln \rho}{\partial \ln Y} \right)_{P,T} \nabla_Y \tag{3.2}$$

where

$$\chi_\rho = \left(\frac{\partial \ln P}{\partial \ln \rho} \right)_{T,Y} \quad \text{and} \quad \chi_T = \left(\frac{\partial \ln P}{\partial \ln T} \right)_{P,Y} \tag{3.3}$$

and $\nabla_Y = \frac{\mathrm{d} \ln Y}{\mathrm{d} \ln P}$ is the true Y gradient in the model.

3.3.2 Model atmospheres and Jupiter's Bond albedo

A fundamental input for a planetary evolution model is the surface boundary condition that sets how quickly the planet can cool. While the total emitted power from the jovian planets is fairly well constrained (Li et al. 2010, 2012), it is more subtle to determine what fraction is emerging from the planet's deep interior (the intrinsic flux

from contraction and interior processes) as opposed to being re-radiated from absorbed stellar light. Measuring the latter requires broad coverage in phase angle, a requirement that was met in *Cassini* ISS/VIMS observations during the spacecraft's flyby of Jupiter in 2000-2001. Li et al. (2018) analyzed these data to arrive at a new measurement of $A = 0.503 \pm 0.012$ for Jupiter's Bond albedo, a significant departure from the *Voyager* result of $A = 0.343 \pm 0.032$ (Hanel et al. 1981a). As described by Li et al. (2018), the new larger reflectivity obtained for Jupiter's atmosphere indicates that the planet's intrinsic flux is substantially higher than previously believed.

We apply the model atmospheres of Fortney et al. (2011) for Jupiter and Saturn. These models assume no particular Bond albedo, instead solving for a self-consistent radiative-convective equilibrium accounting for the absorption of stellar flux. These models are consistent with *Voyager* estimates for each planet's Bond albedo, and thus the intrinsic flux they predict for Jupiter at its present-day surface gravity and $T_{\rm eff}$ falls below the recent *Cassini* measurement. In order to apply a more realistic surface condition for Jupiter, we adjust the $T_{\rm int}$ column of the Fortney et al. (2011) Jupiter tables to instead be consistent with the Bond albedo reported by Li et al. (2018). In particular, we recompute $T_{\rm int}$ from

$$T_{\rm eff}^4 = T_{\rm int}^4 + T_{\rm eq}^4 \tag{3.4}$$

where $T_{\rm eff}$ is as given in the tables and $T_{\rm eq} = 102.5$ K is the value implied by $A = 0.503$ for the solar flux received at Jupiter's semimajor axis. The predictions of the model atmospheres modified in this way deviate from their tabulated values only at relatively late

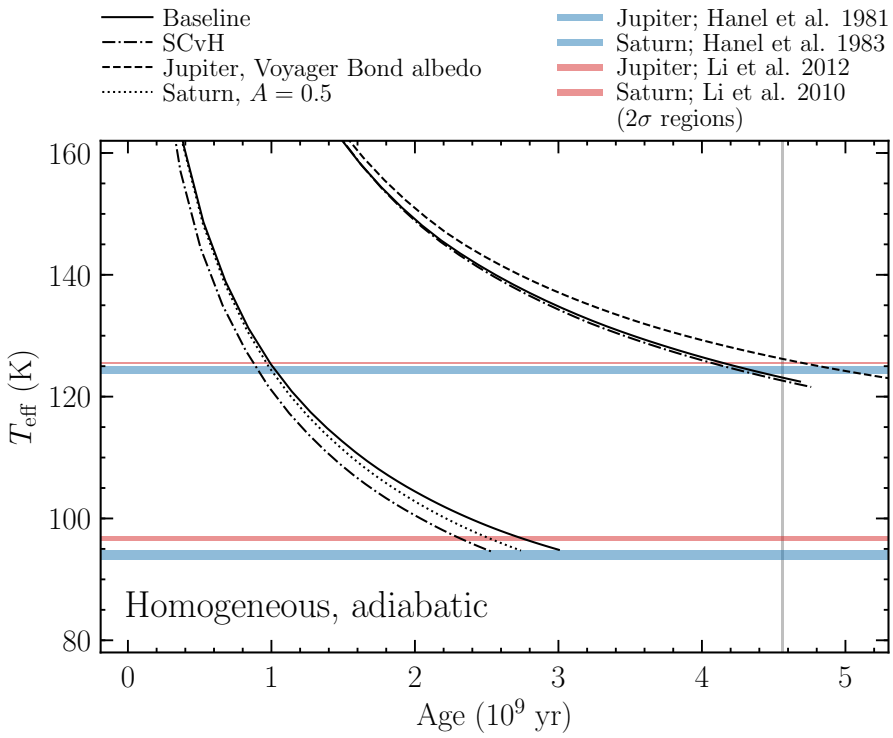

Figure 3.5: The importance of the assumed hydrogen EOS and surface boundary condition for Jupiter and Saturn cooling times. "Baseline" uses the up-to-date Bond albedos and the Militzer & Hubbard (2013) hydrogen-helium EOS combined with Saumon et al. (1995) helium as described in the text. Shaded regions mark the observed effective temperatures and the solar age $\tau_\odot = 4.56$ Gyr.

times when the absorbed solar flux (proportional to $T_{\rm eq}^4$) becomes significant compared to the intrinsic flux ($\propto T_{\rm int}^4$).

3.3.3 Expectations from simpler evolution models

To illustrate the influence of atmospheric surface condition on cooling times, we show in Figure 3.5 baseline cooling curves for Jupiter and Saturn assuming homogeneous, adiabatic interiors. The *Voyager* (Hanel et al. 1981a) and *Cassini* (Li et al. 2018) determinations of Jupiter's Bond albedo are compared. Analysis of existing *Cassini* data

may also reveal a higher albedo for Saturn, and thus for that case we compare the *Voyager* (Hanel et al. 1983) Bond albedo is to a hypothetical higher value of $A = 0.5$. Two EOSs for hydrogen (Militzer & Hubbard 2013; Saumon et al. 1995) are also compared. The assumed EOS has only a modest effect on Jupiter's cooling time, whereas the updated surface condition accelerates the time for Jupiter to cool to its observed $T_{\rm eff}$ by a significant few times 10^8 yr. For Saturn, both the EOS and the surface condition significantly modify the cooling time, but in any case homogeneous models fail to explain Saturn's heat flow at the solar age $t = \tau_\odot = 4.56$ Gyr, recovering a well-known result (Pollack et al. 1977; Grossman et al. 1980; Fortney et al. 2011).

It is significant that Jupiter's revised albedo brings cooling times for homogeneous models short of 4.56 Gyr, because it means that some amount of additional luminosity from differentiation of the planet's chemical components can be straightforwardly accommodated. Jupiter and Saturn now both require an extra luminosity source, and given our expectations for the relative amounts of helium lost from each planet's molecular envelope (Section 3.2), it appears that helium immiscibility may provide one natural explanation. The success of this scenario in explaining the observed heat flow in both planets is assessed in detail in Section 3.4 below.

3.3.4 Parameter estimation

The evolution models here contain four free parameters. The core mass $M_{\rm c}$ and envelope heavy element abundance Z_1 control the distribution of heavy elements. As described in Section 3.2.3, the phase diagram temperature offset $\Delta T_{\rm phase}$ controls the temperatures of the hydrogen-helium phase curves and thus dictates the overall amount

Table 3.1: Jupiter and Saturn evolutionary constraints

Quantity	Jupiter	Saturn	Reference
$T_{\rm eff}$ (K)[a]	96.67 ± 0.17	125.57 ± 0.07	Li et al. (2012, 2010)
R (km)[b]	$69,911 \pm 70$	$58,232 \pm 58$	Seidelmann et al. (2007)
Age (10^9 yr)	4.56±0.10		Connelly et al. (2012)
$Y_1/(X_1 + Y_1)$	0.238 ± 0.005	–	von Zahn et al. (1998)

[a]Mean value used as the condition for model-data comparison rather than fit; see Section 3.3.4.

[b]Errors are inflated to 10^{-3} times the mean value, about ten times the true volumetric radius uncertainty.

of helium differentiation. Finally the density ratio R_ρ sets the superadiabaticity of the temperature profile in regions with continuous helium gradients, providing an additional degree of freedom in setting the rate of cooling from the planet's surface by limiting the flux emerging from the metallic interior (e.g., Nettelmann et al. 2015; Mankovich et al. 2016).

We estimate these parameters independently for each planet by starting with the planets' observed mean radii and effective temperatures at the solar age 4.56 Gyr, applying Bayes' theorem assuming that the likelihood of the data given a model follows a multivariate normal distribution with trivial covariance, and sampling from the posterior probability distribution using the ensemble Markov chain Monte Carlo sampler `emcee` (Foreman-Mackey et al. 2013). Uniform priors are assigned to each of the four parameters within the ranges $0 < M_{\rm c} < 30$, $0 < Z_1 < 0.5$, $|\Delta T_{\rm phase}| < 2,000$ K, and $0 \leq R_\rho < 1$ except in cases where otherwise noted. Samples are judged to be converged based on inspection of the posterior distributions and the individual traces of each walker in the sampler. The samples described below consist of between 30,000 and 60,000 evolutionary models each.

For Jupiter models, the likelihood includes an additional term comparing the *Galileo* probe interferometric measurement of Jupiter's atmospheric helium abundance von Zahn et al. (1998) to the abundance in the well-mixed molecular envelope of the models. Because this interferometric measurement, along with the variety of estimates obtained for Saturn from thermal emission, occultation, and limb scan data, is ultimately sensitive to the He/H_2 mixing ratio, comparisons are made in terms of the helium mass fraction relative to the hydrogen-helium mixture:

$$\frac{Y_1}{X_1 + Y_1} = \frac{Y_1}{1 - Z_1}. \tag{3.5}$$

Here and in what follows X_1, Y_1 and Z_1 denote the true mass fractions of hydrogen, helium, and water respectively in the well-mixed molecular envelope of our model Jupiters and Saturns.

In reality, a slightly less intuitive approach than this is used because the 1-bar temperature T_1 is the fundamental independent variable rather than time t. In particular, our method can guarantee that a given model eventually cools to the correct $T_{\rm eff}$, but there is no guarantee that the same model will reach the solar age $t = \tau_\odot$ before it cools out of the regime covered by the model atmospheres. Therefore, although $T_{\rm eff}$ is in fact the relatively uncertain quantity and the solar age the relatively certain one, we instead cool models to their observed $T_{\rm eff}$ and then treat their age as the uncertain data point, distributed normally about 4.56 Gyr with a somewhat arbitrary standard deviation equal to 0.10 Gyr. This approach has the advantage of bestowing even poorly fitting models with meaningful likelihoods, whereas if model-data comparisons were

always made at 4.56 Gyr it would not be clear what to do with a Saturn model that cooled in, e.g., 4.4 Gyr. In practice all models are cooled through the planet's $T_{\rm eff}$, and quantities compared to data (R, Y_1, age) are linearly interpolated within the timestep spanning that $T_{\rm eff}$.

The data used as constraints for Jupiter and Saturn's thermal evolution are summarized in Table 3.1.

3.4 Results

In what follows we devote our attention to the parameters $\Delta T_{\rm phase}$ and R_ρ pertaining directly to the helium distributions and thermal histories of Jupiter and Saturn, addressing each planet in turn. Because we forgo any detailed calculations of rotation, oblateness, and the associated zonal gravity harmonics, we find as expected that $M_{\rm c}$ and Z_1 are extremely degenerate, essentially unconstrained so long as the total heavy element content is sufficient to fit each planet's mean radius at the solar age. As a result the two parameters are strongly anticorrelated.

3.4.1 Jupiter

The evolutionary paths we obtain for our baseline Jupiter model are shown in Figure 3.6, which illustrates the basic success of this model in matching Jupiter's effective temperature, mean radius, and atmospheric helium content at the solar age.

The first conclusion we can reach based on the solutions obtained for Jupiter is that our model would rule out a phase diagram as cold as SR18, which unperturbed

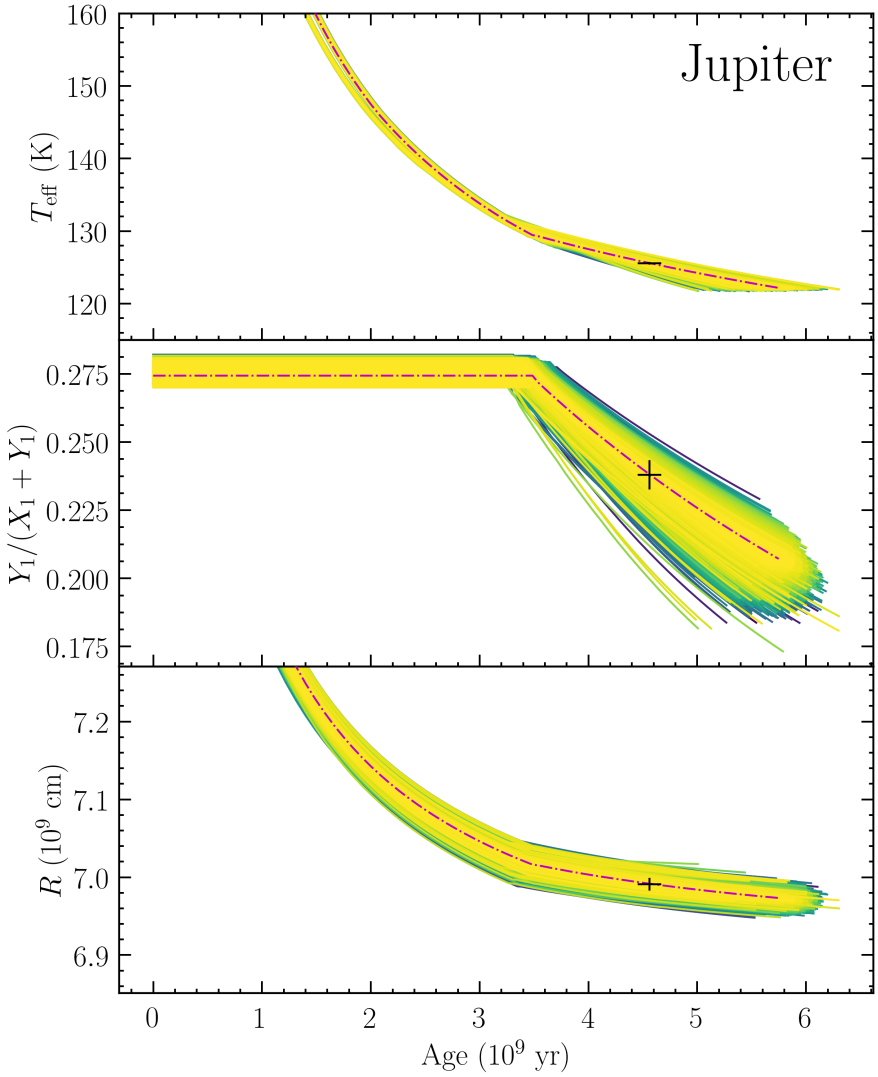

Figure 3.6: Jupiter's evolution with instantaneous helium rainout following the SR18 phase diagram. Tracks are colored by their log posterior probability with more likely models appearing yellow and progressively less likely samples appearing green to blue to purple. Black crosses signify the data summarized in Table 3.1. The most likely individual model is shown as the dot-dashed magenta curve.

($\Delta T_{\rm phase} = 0$) leads to such subtle differentiation of helium that the model overestimates Jupiter's atmospheric helium abundance relative to the *Galileo* measurement (Figure 3.7). This lends more systematic confirmation of the initial expectations of Section 3.2.3 and of Schöttler & Redmer (2018), who predicted based on a preliminary comparison to reference adiabats that helium immiscibility is marginal or absent in Jupiter. We find that translating the SR18 phase curves to modestly higher temperatures at $\Delta T_{\rm phase} = (128 \pm 24)$ K instead gives excellent agreement. Furthermore $\Delta T_{\rm phase}$ shows very weak covariance with other parameters, being constrained almost entirely by the *Galileo* measurement.

As discussed above, any superadiabatic regions associated with helium gradients bear on cooling times directly, because they can generally trap heat in the deep interior and cause the molecular envelope to cool relatively quickly. Larger R_ρ can thus generally mitigate the cooling time extension offered by helium differentiation, although speaking generally, the process can become complicated by the feedback between the temperature profile and the equilibrium helium distribution providing the stratification. Nonetheless, as in Mankovich et al. (2016), the simple picture just described is the general behavior observed in our Jupiter models after helium begins differentiating. The relationship between superadiabaticity R_ρ and cooling time is illustrated in Figure 3.8, where results for the baseline model are compared with those assuming the older *Voyager* Bond albedo from Hanel et al. (1981a). The comparison reveals that Jupiter's updated albedo allows excellent fits at low or vanishing superadiabaticity. This is qualitatively consistent with the findings in Mankovich et al. (2016), where once the Bond

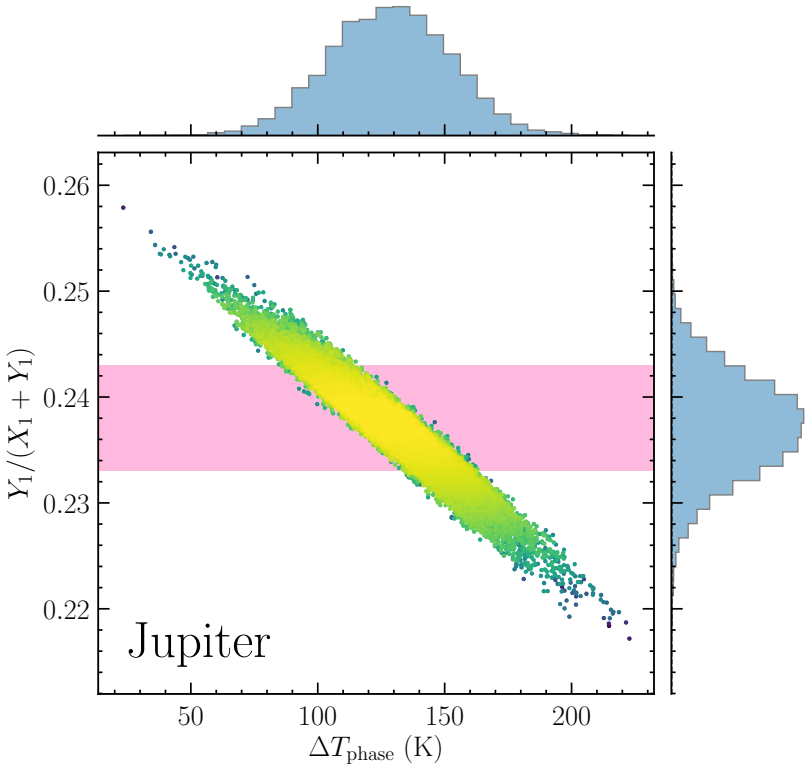

Figure 3.7: Prediction for the temperature of the true phase diagram (relative to the unperturbed SR18 diagram) based on the atmospheric helium content of Jupiter. The shaded band represents the *Galileo* probe interferometer measurement (von Zahn et al. 1998), and the color of model points maps to log posterior probability as in Figure 3.6. Shown is the baseline (superadiabatic) Jupiter sample, but other Jupiter cases (adiabatic; low albedo) yield virtually identical distributions on this diagram.

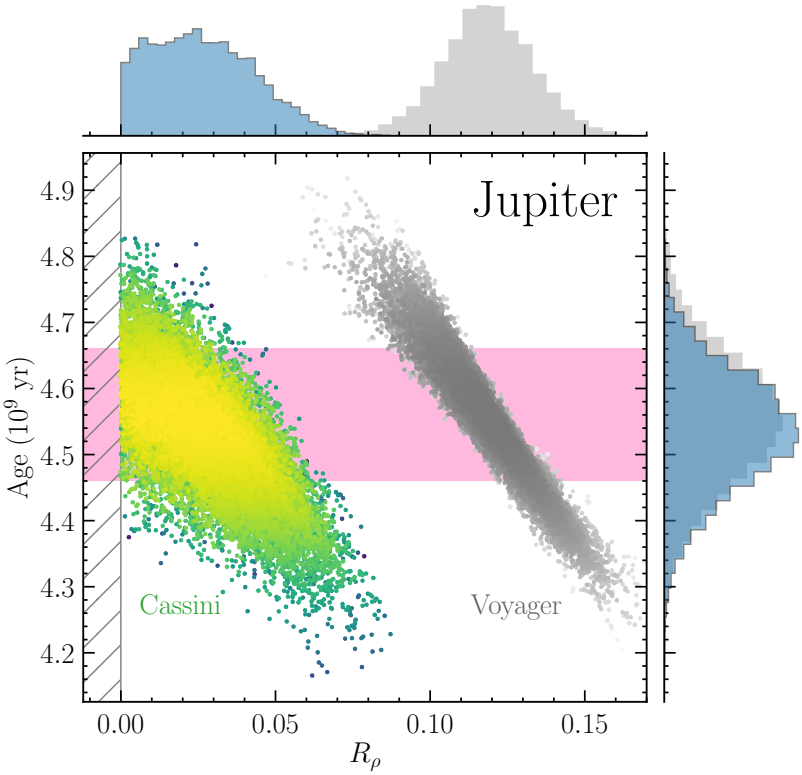

Figure 3.8: Prediction for the fractional superadiabaticity in Jupiter's helium gradient region. Two different assumptions regarding the atmospheric boundary condition are compared; one is the recent *Cassini* Bond albedo measurement from Li et al. (2018, yellow-green points and blue histograms) and the other is the *Voyager* measurement from Hanel et al. (1981a, grey points and histograms).

albedo was treated as a free parameter, solutions with larger albedos (lower $T_{\rm eq}$) and interiors closer to adiabatic were recovered. The quantitative results obtained there were different from the present results because of the more strongly restrictive prior assumed for R_ρ there (see Section 2.4 of that work), and to a lesser degree the older, likely less realistic EOS and phase diagram used in those calculations.

Need Jupiter be superadiabatic?

Even adiabatically stratified ($R_\rho = 0$) models appear to succeed for Jupiter based on Figure 3.8, raising the question, would strictly adiabatic models do any worse? To answer this, we computed samples for models assuming purely adiabatic interiors. In such a model $\nabla = \nabla_{\rm ad}$ everywhere outside the isothermal core, although it's crucial to understand that even an adiabatic envelope is no longer isentropic once helium begins differentiating and the temperature profile and helium/entropy are solved for self-consistently. We find that strictly adiabatic interiors, i.e., efficient heat transport by convection through helium gradient regions, perform no worse in terms of the quality of the best-fitting models. This is quantified in terms of an Akaike (1974) information criterion

$$\mathrm{AIC} = 2n - 2\ln\mathcal{L}_{\rm max} \tag{3.6}$$

where n is the number of free parameters in each sample and $\mathcal{L}_{\rm max}$ is the maximum likelihood obtained therein. The model yielding the minimum AIC will represent the minimally complex model that can also yield a good fit. We find AIC = 27.8568 for the adiabatic ($n = 3$) Jupiter sample compared to AIC = 29.8364 for the baseline ($n = 4$) Jupiter sample, indicating that the baseline model is probably overfit by the introduction of finite superadiabaticity R_ρ associated with helium gradients. We thus emphasize our three-parameter, adiabatic Jupiter sample as our preferred model.

3.4.2 Saturn

We find an abundance of Saturn models that successfully explain Saturn's heat flow at the solar age. Evolutionary sequences for baseline Saturns are shown in Figure 3.9. Because this sample enforces no constraint on Saturn's atmospheric helium content at the solar age, and a uniform prior probability is assigned to $\Delta T_{\rm phase}$, this sample explores a wide variety of phase diagrams via $\Delta T_{\rm phase}$. This manifests in the diversity of evolutionary paths in Figure 3.9 and the quite broad posterior $\Delta T_{\rm phase}$ distribution shown in Figures 3.10 and 3.11 with the label "unconstrained phase diagram." As is the case for Jupiter, good solutions for Saturn require that SR18 be translated to warmer temperatures, this time driven by Saturn's luminosity constraint: taken at face value, the SR18 phase curves predict insufficient differentiation for Saturn to provide the planet's observed luminosity.

In addition to the distribution of $\Delta T_{\rm phase}$ being considerably broader for this Saturn sample, there is also a distinct bimodality that was absent for Jupiter. This bimodality arises because the model cooling times exhibit a strongly non-monotone dependence on $\Delta T_{\rm phase}$, as is evident in Figure 3.11. The first mode corresponds to phase diagrams consistent with SR18 to within a few hundred K, where warmer phase curves *extend* Saturn's cooling time because they lead to more pronounced differentiation in the planet. This behavior has a limit, though, corresponding to phase curves that are so warm that they lead to the *complete* exhaustion of the helium that initially resided in the molecular envelope. This is the case for models beyond $\Delta T_{\rm phase} \approx 550$ K, where hotter phase diagrams push this exhaustion time for Saturn farther into the

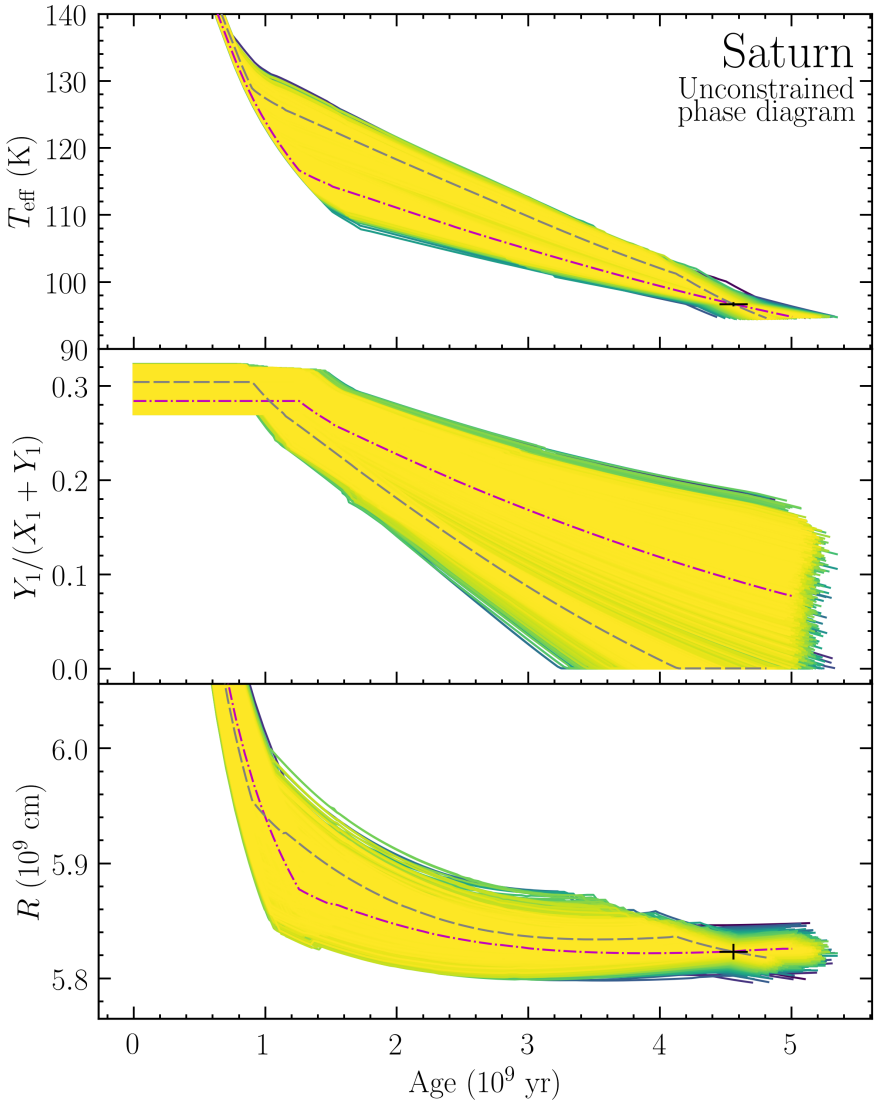

Figure 3.9: As in Figure 3.6, but for Saturn. This is our baseline (most general) Saturn sample with a uniform prior on $\Delta T_{\rm phase}$. Individual histories are plotted for two ostensibly good solutions: the most likely model with $\Delta T_{\rm phase} < 550$ K is shown in the magenta dot-dashed curve, and the most likely model with $\Delta T_{\rm phase} > 550$ K is shown in the grey dashed curve. The latter case exhausts the helium in its molecular envelope entirely at $t \approx 4.1$ Gyr; this type of evolution is not favored for reasons discussed in the text.

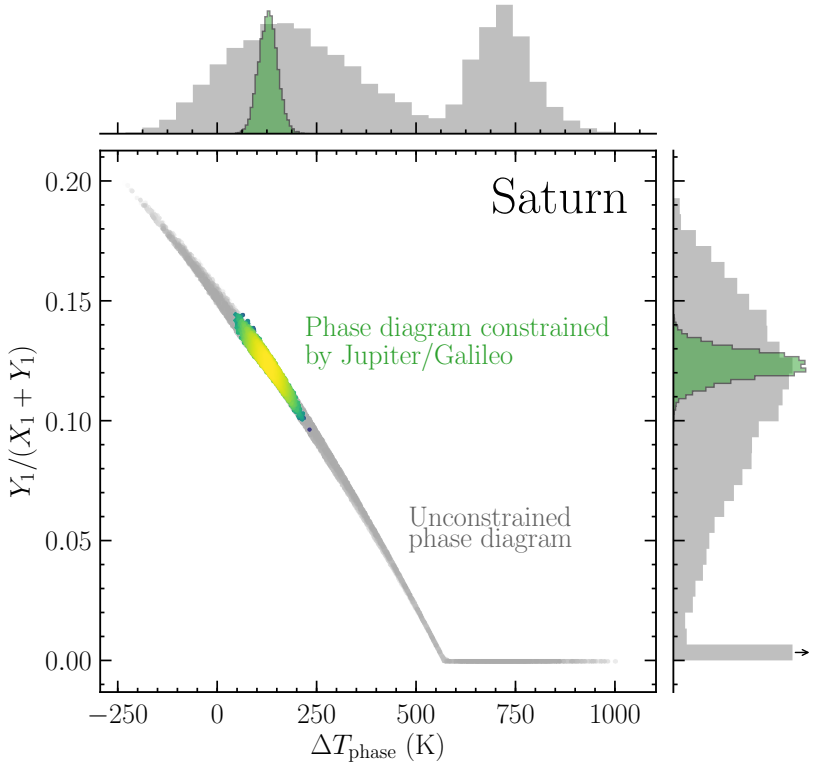

Figure 3.10: As in Figure 3.7, but for Saturn, and this time comparing two assumptions about the phase diagram via the prior assigned to $\Delta T_{\rm phase}$. Grey points and histograms show the sample obtained for a uniform prior in $\Delta T_{\rm phase}$, and colorful points and green histograms show the sample obtained using a prior distribution for $\Delta T_{\rm phase}$ derived from the Jupiter *Galileo* measurement as illustrated in Figure 3.7.

past. In this limit the models begin to again undershoot the solar age because an increasing fraction of their time is spent in a final episode of rapid cooling after their differentiation luminosity vanishes. This behavior is exhibited by the second mode visible in Figure 3.11. Individual evolution tracks typifying each of these modes are highlighted in Figure 3.9.

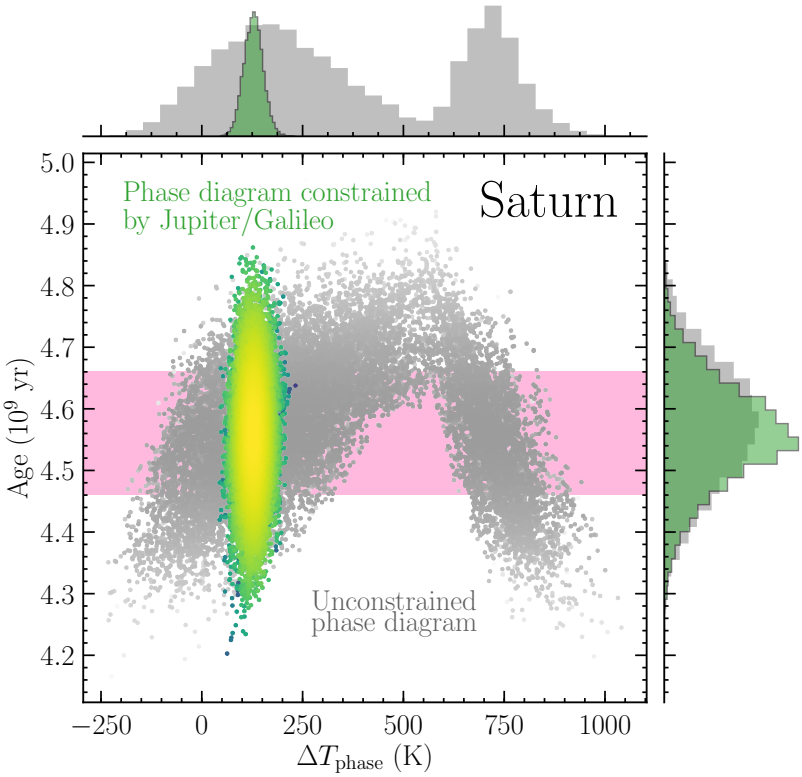

Figure 3.11: As in Figure 3.10, but this time showing the influence of $\Delta T_{\rm phase}$ on Saturn's cooling time. The non-monotone relationship for the sample with no constraint on the phase diagram is caused by the models with $\Delta T_{\rm phase} \gtrsim 550$ K losing the helium from their molecular envelopes entirely before the solar age, evolving on a rapid cooling track from that time.

A better-informed phase diagram

There are several reasons that the "hot phase diagram" mode of Saturn solutions just described is probably not realistic. First, total exhaustion of helium from the molecular envelope appears to be ruled out by a multitude of *Voyager* and *Cassini* experiments (Conrath et al. 1984; Conrath & Gautier 2000; Banfield et al. 2014; Achterberg et al. 2016; Koskinen & Guerlet 2018). Second, the scenario requires that the true phase diagram depart from SR18 by $\Delta T_{\rm phase} \gtrsim 700$ K, probably an unrealistically large departure given the level of consensus emerging from different *ab initio* groups over recent years (Lorenzen et al. 2009, 2011; Morales et al. 2009, 2013; Schöttler & Redmer 2018). The third problem with such a scenario, and the most important from the point of view of this work, is that the phase diagram that it requires would drastically underpredict Jupiter's observed atmospheric helium abundance. The same fundamental physics is at work within both planets; in the interest of applying a consistent physical model to both, we carry out a new calculation for Saturn that folds in our belief about the true phase diagram as informed by the Jupiter models that satisfy the *Galileo* measurement (see Section 3.4.1 and Figure 3.7).

This updated Saturn sample imposes a prior likelihood for $\Delta T_{\rm phase}$ proportional to the marginalized posterior distribution obtained for Jupiter and driven by the *Galileo* probe measurement of Jupiter's atmospheric helium abundance. This distribution is fit well by a normal distribution with mean 128 K and standard deviation 24 K (see Section 3.4.1). Evolutionary tracks for this more restrictive sample are summarized in Figures 3.12. Good solutions are still obtained for Saturn, as expected based on the

considerable amplitude of the unconstrained sample's posterior probability distribution in the neighborhood of $\Delta T_{\rm phase} = (128 \pm 24)$ K. Distributions for $\Delta T_{\rm phase}$ are illustrated in Figures 3.10 and 3.11 and labeled "phase diagram constrained by Jupiter/*Galileo*." As expected, the posterior distributions exclude very hot phase diagrams. Figure 3.10 emphasizes a significant result: having folded in our expectations for the temperature of the phase diagram based on Jupiter, we can make a meaningful prediction for the helium content of Saturn's molecular envelope. This prediction is illustrated in more detail and compared to abundances derived from observations of Saturn's atmosphere in Section 3.4.2 below.

Need Saturn be superadiabatic?

In Section 3.4.1 we demonstrated that superadiabaticity need not be invoked to recover satisfactory solutions for Jupiter; here we turn our attention to the same question for Saturn. The distributions in Figure 3.13 are largely consistent with $R_\rho = 0$, leading one to expect that adiabatic models perform roughly as well as the rest. Considering first Saturns with an unconstrained phase diagram, we find that an adiabatic ($n = 3$) sample yields AIC = 36.2254 while the equivalent superadiabatic ($n = 4$) sample yields AIC = 38.2254. Repeating this exercise for the case with the more realistically constrained phase diagram, we find that an adiabatic sample returns AIC = 36.3088 compared to AIC = 38.2258 for a superadiabatic sample. In all cases this reasoning suggests that the superadiabatic models introduce additional model complexity with no little to no return in terms of quality of fit. Thus our favored Saturn models are those assuming adiabatic interiors and phase diagrams constrained by Jupiter/*Galileo*.

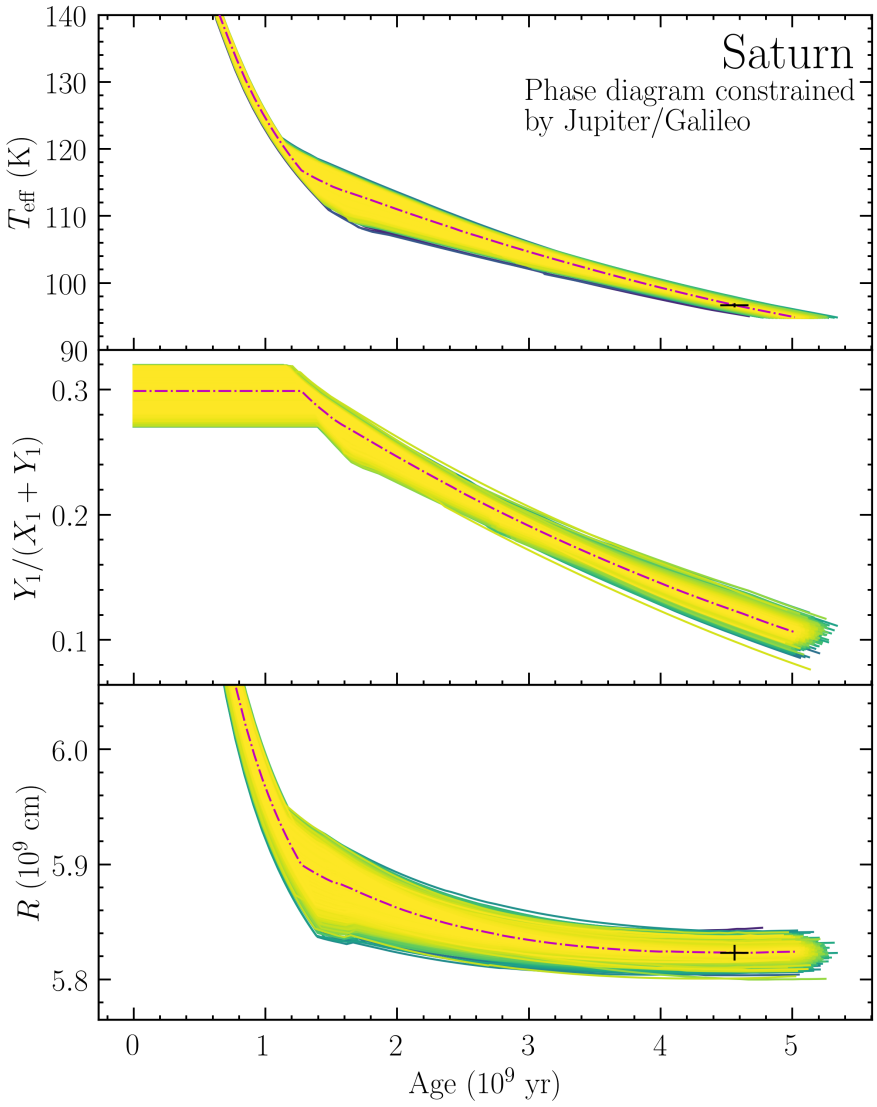

Figure 3.12: As in Figure 3.9, but applying phase diagrams that satisfy the *Galileo* measurement of Jupiter's atmospheric helium abundance.

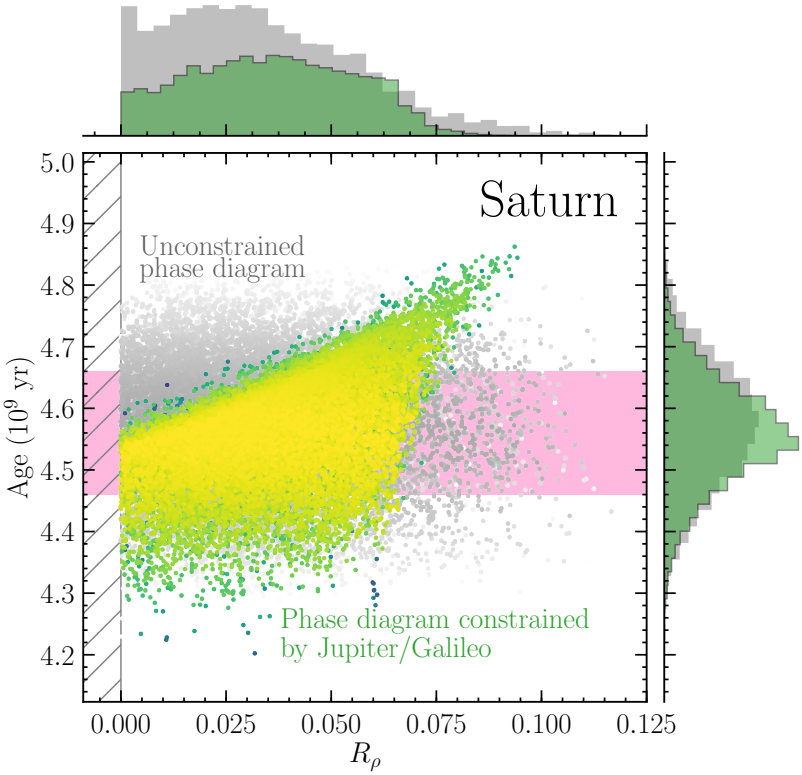

Figure 3.13: As in Figure 3.10, but showing the influence of R_ρ on Saturn's cooling time.

Implications of the success of adiabatic models will be discussed in Section 3.5.

Saturn's atmospheric helium content

The abundance of helium in Saturn's atmosphere is the central testable prediction of the models presented here. Figure 3.14 summarizes our findings in this respect, with our best guess represented by either of the two very similar distributions in the lower panel. Our prediction is consistent with, but better constrained than, the earlier theoretical predictions of Hubbard et al. (1999) and Nettelmann et al. (2015). The broad distributions in the upper panel are disfavored for the reasons described in Section 3.4.2.

Observational determinations of the He to H_2 mixing ratio have been made by various means, typically combining thermal emission spectra with vertical temperature profiles obtained from radio occultations or infrared limb scans. Values derived in this way from *Pioneer* (Orton & Ingersoll 1980), *Voyager* (Conrath et al. 1984), and *Cassini* data (Banfield et al. 2014; Achterberg et al. 2016; Koskinen & Guerlet 2018), and also from purely infrared *Voyager* data (Conrath & Gautier 2000), have yet to reach a consensus, but they are generally consistent with depletion from the protosolar helium abundance. Figure 3.14 compares these values alongside the theoretical results derived here. We predict a more pronounced depletion than implied by most of these observations. The exceptions are the low estimate of Conrath et al. (1984) (likely unreliable for reasons explained in Conrath & Gautier 2000) and the measurement reported by Achterberg et al. (2016) which agrees very well. Given the challenging systematics involved with measurements like these, a definitive validation or exclusion of our prediction may need to await an *in situ* measurement of Saturn's atmospheric helium abundance.

3.4.3 Is neon depletion energetically significant?

Besides just helium, Jupiter shows evidence for depletion of its atmospheric neon, exhibiting an abundance around 1/10 the protosolar value by number (Niemann et al. 1998). This depletion is generally understood to be a consequence of neon's tendency to dissolve into the helium-rich droplets (Roulston & Stevenson 1995; Wilson & Militzer 2010) that are lost to the interior. Thus the atmospheric neon depletion observed *in situ* at Jupiter offers a strong secondary confirmation of the notion that

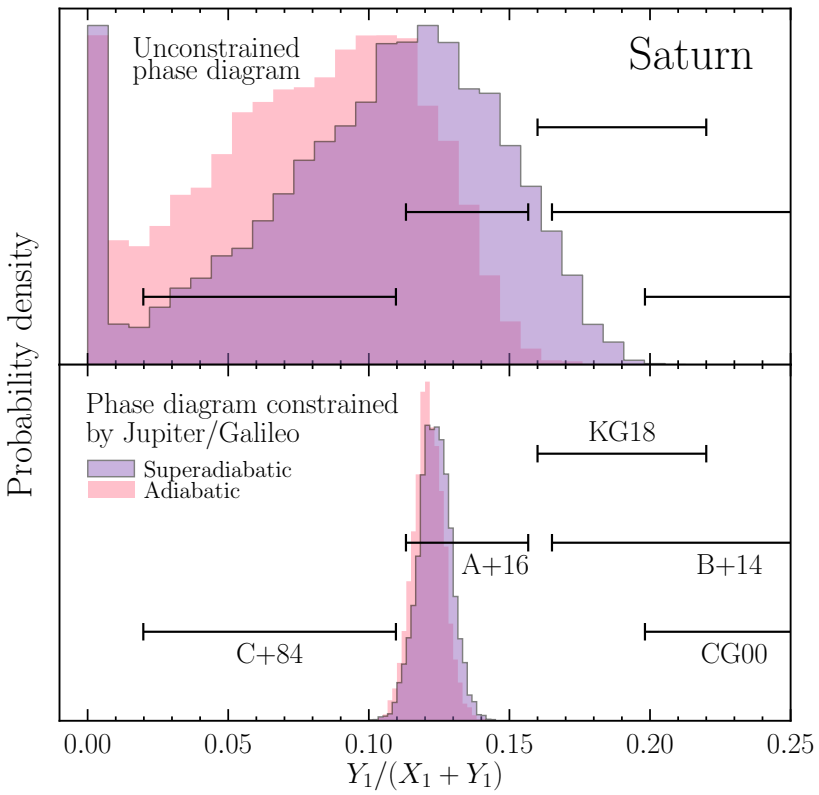

Figure 3.14: The helium mass fraction relative to total hydrogen and helium predicted for Saturn's atmosphere today. *Top:* Saturn models with uniform priors as described in the text. *Bottom:* Saturns with a prior on $\Delta T_{\rm phase}$ set by the posterior obtained for Jupiter (Figure 3.7) and driven by the *Galileo* probe helium abundance measurement (von Zahn et al. 1998). Black error bars are values derived from *Voyager* (Conrath et al. 1984; Conrath & Gautier 2000) and *Cassini* (Banfield et al. 2014; Achterberg et al. 2016; Koskinen & Guerlet 2018) data.

helium differentiation has occurred in Jupiter.

What has not been considered is the energetic significance of sinking neon along with the sinking helium. Assuming that Jupiter's global neon enrichment is similar to its observed atmospheric enrichment in the other noble gases at 2 to 3 times protosolar (Atreya et al. 2016), then Jupiter's atmospheric neon has depleted by a factor of 20-30. If we further make the assumption that neon was initially well mixed throughout the envelope after formation, and its atmospheric depletion is driven entirely by loss into helium-rich droplets at the molecular-metallic interface, then the degree of neon differentiation at the solar age is simply set by the relative masses in the helium-poor (molecular) and helium-rich (metallic) regions of the interior.

Figure 3.15 applies this reasoning to our most likely adiabatic Jupiter model, showing the enclosed helium or neon mass as a function of enclosed mass in the planet. We suppose that Jupiter's bulk neon enrichment is similar to its atmospheric argon enrichment at ≈ 3 times protosolar (Mahaffy et al. 2000; Asplund et al. 2009), implying an initial neon mass fraction $X_{\mathrm{Ne}} \approx 4 \times 10^{-3}$ in Jupiter's envelope for a total neon mass of $M_{\mathrm{Ne}} \approx 1.2\ M_{\mathrm{E}}$, approximately 0.3 M_{E} of which resides in the molecular envelope when helium immiscibility sets in. The observed atmospheric abundance at about 1/10 protosolar—the exact value is taken from Mahaffy et al. 2000—translates into a final neon mass fraction of $X_{\mathrm{Ne}} \approx 2 \times 10^{-4}$ in Jupiter's molecular envelope for a final neon mass $M_{\mathrm{Ne}} \approx 10^{-2}\ M_{\mathrm{E}}$ remaining there. The molecular envelope thus lost virtually all 0.3 M_{E} of its neon since the onset of helium immiscibility, compared to the $\approx 2.0\ M_{\mathrm{E}}$ of helium that sank to the metallic depths for the same model.

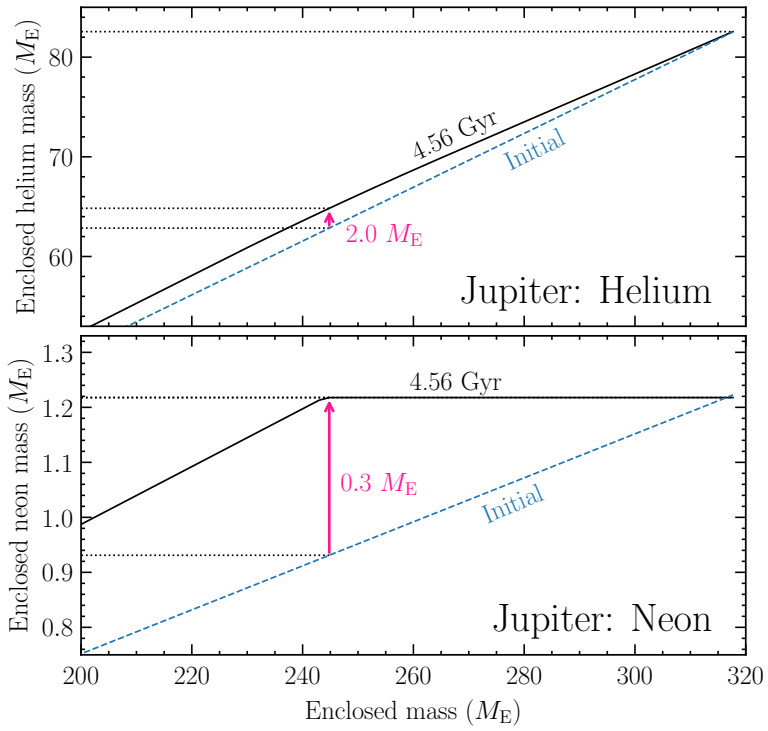

Figure 3.15: The initially well-mixed versus final, differentiated, distributions of helium (top panel) and neon (bottom panel) in Jupiter's interior for the simple models discussed in Section 3.4.3. Enclosed helium (or neon) mass is plotted as a function of the enclosed mass. The arrows and adjacent labels indicate the difference between initial and final helium (or neon) mass residing in the molecular envelope; this mass difference is lost to the deeper metallic interior starting with the onset of helium immiscibility.

Our models suggest that the differentiation of helium is more advanced in Saturn, and consequently we expect depletion of neon in Saturn's atmosphere to be more severe than in Jupiter's. For the sake of these simple estimates, we assume that Saturn's outer envelope contains a negligible mass of neon at the present day. As before we assign a fiducial bulk enrichment for neon based on measurements of different species, this time supposing that neon tracks the carbon enrichment at ≈ 10 times protosolar per the methane abundances from Fletcher et al. (2009). We assume that the dissolved neon follows helium-rich droplets all the way to the helium-rich shell; the neon transition in this simplistic model therefore takes place substantially deeper than the molecular-metallic transition. Figure 3.16 illustrates the result of applying this exercise to our most likely adiabatic Saturn model including the Jupiter/*Galileo* phase diagram prior. This model sheds 0.7 $M_{\rm E}$ of neon from its outer envelope compared to 12 $M_{\rm E}$ of helium.

Calculating the associated change in the gravitational binding energy of neon provides an estimate of the energetic significance of neon differentiation. From the composition profiles in Figures 3.15 and 3.16 we calculate initial and final values for the binding energies

$$E_{\rm He} = -\int_0^{M_{\rm He}} \frac{Gm}{r}\,{\rm d}m_{\rm He} \tag{3.7}$$

and

$$E_{\rm Ne} = -\int_0^{M_{\rm Ne}} \frac{Gm}{r}\,{\rm d}m_{\rm Ne} \tag{3.8}$$

with $m_{\rm He}$ the enclosed helium mass, $m_{\rm Ne}$ the enclosed neon mass, and m the enclosed total mass. For Jupiter, we find that $\Delta E_{\rm Ne} \sim 10^{40}$ erg compared to $\Delta E_{\rm He} \sim 10^{41}$ erg. In

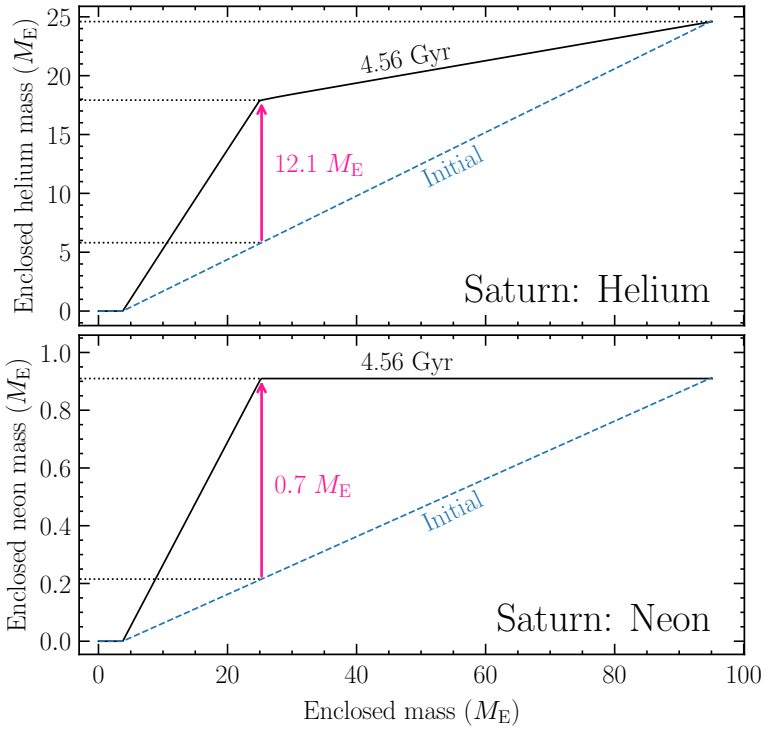

Figure 3.16: As in Figure 3.15, but for Saturn.

the case of Saturn, we find $\Delta E_{\rm Ne} \sim 3 \times 10^{39}$ erg compared to $\Delta E_{\rm He} \sim 10^{41}$ erg. We thus expect that neon sequestration could bolster the luminosity from helium differentiation by as much as $\sim 10\%$ for Jupiter and $\sim 3\%$ for Saturn, an effect not captured in the thermal evolution models of this work.

While crude, the arguments suggest that the luminosity that helium differentiation provides to each planet is augmented somewhat by the accompanying sequestering of neon, at least in a time-averaged sense. Apart from the unknown bulk neon abundances for Jupiter and Saturn, there is an additional layer of complexity associated with the precise time evolution. Considering Jupiter's pronounced neon depletion in spite of helium immiscibility having set in only recently, it seems possible that Saturn's neon was sequestered rapidly after immiscibility set in $\gtrsim 3$ Gyr ago. In this case the luminosity source may have been episodic in nature—potentially on timescales close to the thermal timescale—and deducing its influence on Saturn's cooling time as a whole would require a more detailed thermal evolution model as well as a more detailed hydrogen-helium-neon immiscibility model. For these reasons, explicit treatment of neon in the evolutionary models is beyond the scope of this work, but deserves closer attention as models like these are refined.

3.5 Discussion

This work provides a self-consistent physical picture for the thermal evolution of Jupiter and Saturn in detail, an outcome that had so far proven elusive. These models are built on the premise that some degree of hydrogen-helium immiscibility—and

rainout of the resulting helium-rich phase—occurs in both planets, a notion supported by decades of work spanning dense matter physics (e.g., Stevenson 1975; Hubbard & Dewitt 1985; Morales et al. 2009; Lorenzen et al. 2009) and planetary science (e.g., Smoluchowski 1967; Stevenson & Salpeter 1977b; von Zahn et al. 1998; Conrath & Gautier 2000). The evolution models presented here apply recent advances in the equation of state of hydrogen (Militzer & Hubbard 2013), the phase diagram describing miscibility of hydrogen-helium mixtures (Schöttler & Redmer 2018), and the atmospheres of the gas giants (Fortney et al. 2011; Li et al. 2018). Sampling parameter space systematically using Markov chain Monte Carlo, we are able to arrive at solutions that naturally explain the radii and heat flow of both Jupiter and Saturn at the solar age, as well as Jupiter's observed atmospheric helium depletion.

The value in this final constraint is that it puts stringent limits on allowable phase diagrams. The parameter estimation performed in this work provides statistically meaningful distributions of model parameters, estimating for instance that based on Jupiter's helium depletion, the true phase diagram is warmer than the most current *ab initio* phase diagram (Schöttler & Redmer 2018) by a mere (124 ± 24) K (1σ error) at the ≈ 2 Mbar pressures that it predicts for the onset of helium immiscibility in metallic hydrogen. That this correction is so modest suggests that the *ab initio* dense matter results may be converging on truth. (For comparison, Jupiter models built on a previous generation of phase diagram that assumed ideal hydrogen-helium mixing entropy predicted the necessary temperature offset to be between 200 and 300 K, in the opposite direction (Nettelmann et al. 2015; Mankovich et al. 2016).) These findings imply

a rather precise prediction for Saturn's atmospheric helium abundance summarized in Figure 3.14. The posterior predictive Y_1 distribution for our favored model is well fit by a Gaussian producing a helium mass fraction, relative to hydrogen and helium, of 0.12 ± 0.01 (2σ error). The corresponding He/H_2 mixing ratio is 0.066 ± 0.006, consistent with one measurement made from multi-instrument *Cassini* data but inconsistent with others. An *in situ* determination of Saturn's atmospheric helium abundance provided by an entry probe (e.g., SPRITE; Simon et al. 2018) would be decisive test of the evolutionary picture developed here.

Another important result is that although superadiabaticity resulting from some flavor of double-diffusive convection in metallic regions possessing helium gradients does modulate the cooling time for Jupiter and Saturn, equally good solutions are found for both planets assuming purely adiabatic envelopes corresponding to essentially perfect convection. This runs contrary to the expectation from earlier modeling efforts (e.g., Hubbard et al. 1999; Fortney & Hubbard 2003; Fortney et al. 2011; Nettelmann et al. 2015; Mankovich et al. 2016) that Jupiter required some mechanism (non-adiabatic interiors or otherwise) to speed its evolution rather than prolong it[2]. This development is due to the major improvement in our understanding of the internal heat flow of Jupiter in light of recent *Cassini* results (Li et al. 2018).

The success of even adiabatic models in explaining Jupiter and Saturn's heat flow is rather significant with respect to the remarks in Section 3.3.1: in the limiting case that rainout of the denser helium-rich phase can proceed rapidly with respect

[2]Recognizing this tension, Mankovich et al. (2016) ultimately treated Jupiter's Bond albedo as a free parameter, recovering a median value consistent with the subsequent *Cassini* measurement.

to buoyancy timescales, then the influence of a background helium gradient on fluid buoyancy is lost completely. In this case the condition for convective instability reduces to the Schwarzschild criterion, and so convection in the planet is uninhibited. Thus the success of these adiabatic models can be taken as circumstantial evidence that the rainout process does indeed proceed rapidly compared to any relevant timescale.

Finally the energetic significance of neon differentiation is examined. Assuming that Jupiter's atmospheric neon depletion is driven by dissolution into the helium-rich material lost to the metallic interior, and making an informed guess about the planet's bulk neon abundance, we estimate that Jupiter's time-averaged differentiation luminosity may be increased by $\sim 10\%$ relative to just the helium differentiation treated in the thermal evolution models in this work. Assuming similar bulk abundance patterns for Saturn and assuming that its outer envelope is devoid of neon by the solar age, Saturn's differentiation luminosity could be augmented by a $\sim 3\%$.

3.6 Conclusions

An explanation for Saturn's surprisingly high luminosity has been sought for decades. Models that provide plausible evolution pathways for Saturn invoke either an additional luminosity source beyond straightforward contraction, or interiors that deviate significantly from adiabaticity because of some degree of non-convective heat transport. On the other hand, Jupiter's luminosity is fairly well explained by simple models, but its precisely constrained atmospheric abundances reveal the presence of interior processes that sequester helium and neon. This work applies identical assump-

tions to Jupiter and Saturn, calculating new thermal evolution models in the context of recent results regarding hydrogen-helium immiscibility physics and a significantly updated measurement of Jupiter's intrinsic heat flow. We have showed that these models naturally address the observed heat flow from both Jupiter and Saturn at the solar age, as well as Jupiter's atmospheric helium depletion. Even purely adiabatic interiors are successful in these respects. These findings provide a consistent picture for the evolution of both planets simultaneously, and make a precise prediction for Saturn's atmospheric helium abundance. Measuring this quantity *in situ* would provide an observational test of the picture developed here.

Chapter 4

Saturn ring seismology

4.1 Introduction

The prototypical gas giants Jupiter and Saturn offer an opportunity to study the processes at work during planet formation and the chemical inventory of the proto-solar disk, and also constitute astrophysical laboratories for warm dense matter. Inferences about these planets' composition and structure rely on interior models that are chiefly constrained by the their observed masses, radii and shapes, surface abundances, and gravity fields (Stevenson 1982a; Fortney et al. 2016). While the latter have been measured to unprecedented precision by *Juno* at Jupiter and the *Cassini* Grand Finale at Saturn, in the interest of long term progress there is a need to identify independent observational means of studying the interiors, and seismology using the planets' free oscillations appears to be the most promising such avenue.

While preliminary detections of Jupiter's oscillations have been made from the ground by Gaulme et al. (2011), the resulting power spectrum lacked the frequency res-

olution necessary to identify specific normal modes responsible for the observed power, a necessary step before the frequencies can be used to probe the interior in detail. Saturn, on the other hand, provides a unique opportunity for seismic sounding of a Jovian interior owing to its highly ordered ring system, wherein gravity perturbations from Saturn's free oscillations can resonate with ring orbits. Saturn ring seismology is the focus of this work.

4.1.1 Background

The concept of ring seismology was first developed in the 1980s. Stevenson (1982) suggested that Saturnian inertial oscillation modes, for which the Coriolis force is the restoring force, could produce regular density perturbations within the planet that might resonate with ring particle orbits and open gaps or launch waves, but he did not calculate specific mode frequencies. Later in the decade in a series of abstracts, a thesis, and papers Marley, Hubbard and Porco further developed this idea. Marley et al. (1987), relying on Saturn oscillation frequencies computed by Vorontsov (1981), suggested that acoustic mode oscillations, which differ from inertial modes in that their restoring force is ultimately pressure, could resonate with ring particle orbits in the C ring. They recognized that mode amplitudes of a few meters would be sufficient to perturb the rings. Marley & Hubbard (1988) focused on low angular degree ℓ f–modes which have no radial nodes in displacement from surface to the center of the planet (unlike p–modes) as the modes which had the potential to provide the most information about the deep interior of a giant planet. Marley et al. (1989) compared the predicted locations resonance locations of such modes with newly discovered wave

features in the C ring found in radio occupation data by Rosen (1989). They suggested that the Maxwell gap and three wave features found by Rosen which had azimuthal wave numbers and propagation directions consistent with such resonances were in fact produced by Saturnian f–modes with $\ell \leq 4$. As we will summarize below, we now know that these specific f–mode–ring feature associations were correct, although the story for the $\ell = 2$ and $\ell = 3$ waves is complicated by g–mode mixing (Fuller et al. 2014; Fuller 2014).

These ideas were ultimately presented in detail in Marley (1990, 1991) and Marley & Porco (1993). Marley computed the sensitivity of Saturn oscillation frequencies to various uncertainties in Saturn interior models, including core size and regions with composition gradients, and discussed the sensitivity of ring resonance locations to these uncertainties. As we will show below, the overall pattern of resonance locations within the rings first presented in Marley (1990) agrees well with subsequent discoveries. While Marley recognized the impact of regions with non-zero $B-V$frequency N on f–mode frequencies and the possibility of g–modes (for which the restoring force is buoyancy), he did not consider mode mixing between f– and g–modes. Marley & Porco (1993) presented the theory of resonances between planetary oscillation modes and rings in detail and derived expressions for the torque applied to the rings at horizontal (Lindblad) and vertical resonances and compared these torques to those of satellites. They also suggested several more specific ring feature-oscillation mode associations, many of which have subsequently turned out to be correct. Marley and Porco concluded by noting that because the azimuthal wave numbers of the Rosen wave features were uncertain,

only additional observations by the planned future Saturn mission *Cassini* could ultimately test the hypothesized connection between oscillation modes and ring features. Consequently there was essentially a two-decade pause in ring seismology research until those results became available.

Optical depth scans of the C ring from *Cassini* radio occultations and Ultraviolet Imaging Spectrograph stellar occultations presented by Colwell et al. (2009) and Baillié et al. (2011) confirmed all the unexplained waves reported by Rosen et al. (1991b) and identifying many more. Hedman & Nicholson (2013) followed up with VIMS stellar occultations, combining scans taken by *Cassini* at different orbital phases to determine wave pattern speeds and azimuthal wavenumbers m at outer Lindblad resonances, making seismology of Saturn using ring waves possible for the first time. As alluded to above, the detection of multiple close waves with $m = 2$ and $m = 3$ waves deviated from the expectation for the spectrum of pure f–modes. In light of this result, Fuller et al. (2014) investigated the possibility of shear modes in a solid core, finding that rotation could mix these core shear modes with the f–modes and in principle explain the observed fine splitting, although they noted that some fine tuning of the model was required. The most compelling model for the fine splitting to date was presented by Fuller (2014), who showed that a strong stable stratification outside Saturn's core would admit g–modes that could rotationally mix with the f–modes and rather robustly explain the number of strong split $m = 2$ and $m = 3$ waves at Lindblad resonances, and roughly explain the magnitude of their frequency separations.

Subsequent obervational results from the VIMS data came from Hedman &

Nicholson (2014), who detected a number of additional waves including an $m = 10$ wave apparently corresponding to Saturn's $\ell = m = 10$ f–mode. French et al. (2016) characterized the wave in the ringlet within the Maxwell gap (Porco et al. 2005) and argued it to be driven by Saturn's $\ell = m = 2$ f–mode, supporting the prediction by Marley et al. (1989). The remainder of C ring wave detections that form the observational basis for our work are the density waves reported by Hedman et al. (2019) and the density and bending waves reported by French et al. (2019).

4.1.2 This work

Here we seek to systematically understand the ring wave patterns associated with Saturn's normal modes. In particular, we aim to identify the modes responsible for each wave, make predictions for the locations of other Saturnian resonances in the rings, and ultimately assess what information these modes carry about Saturn's interior. We describe the construction of Saturn interior models in Section 4.2. §4.3 summarizes our method for solving for mode eigenfrequencies and eigenfunctions, as well as our accounting for Saturn's rapid rotation. In §4.4 we recapitulate the conditions for Lindblad and vertical resonances with ring orbits and describe which f–modes can excite waves at each. §4.5 presents the main results, namely f–mode identifications and a systematic comparison of predicted f–mode frequencies to the pattern speeds of observed waves and its implications for Saturn's interior, principally its rotation. The separate question of mode amplitudes and detectability of ring waves is addressed in §4.6, which also lists the strongest predicted waves yet to be detected. Discussion follows in §4.7 and we summarize our conclusions with §4.8.

4.2 Interior Models

Our hydrostatic planet interior models are computed using a code based on that of Thorngren et al. (2016) with a few important generalizations. To model arbitrary mixtures of hydrogen and helium, we implement the equation of state of Saumon et al. (1995) (the version interpolated over the plasma phase transition, henceforth "SCvH-I"). Heavier elements are included using the ab initio water EOS of French et al. (2009), extending the coverage to $T < 10^3$ K using the analytical model of Thompson (1990) for water. The density $\rho(Y, Z)$ is obtained assuming linear mixing of the three components following

$$\rho^{-1}(Y, Z) = \frac{Z}{\rho_Z} + \frac{1 - Z}{\rho_{\mathrm{HHe}}(Y)}, \tag{4.1}$$

where in turn

$$\rho_{\mathrm{HHe}}^{-1}(Y) = \frac{Y}{\rho_{\mathrm{He}}} + \frac{1 - Y}{\rho_{\mathrm{H}}}. \tag{4.2}$$

Here Y and Z are the mass fractions of helium and heavier elements, respectively, and the densities ρ_{H}, ρ_{He}, and ρ_{Z} are tabulated as functions of pressure P and temperature T in the aforementioned equations of state.

The outer boundary condition for our interior models is simply a fixed temperature at $P = 1$ bar, namely $T_1 = 140$ K, close to the value derived by Lindal et al. (1985) from *Voyager* radio occultations and mirroring that used in previous Saturn interior modeling efforts (e.g., Nettelmann et al. 2013). The envelope is assumed to be everywhere efficiently convective so that the deeper temperature profile is obtained by

integrating the adiabatic temperature gradient:

$$T(m_r \geq M_c) = T_1 + \int_M^{m_r} \nabla_{ad}(P,\, T,\, Y)\, T\ \mathrm{dln}\, P, \tag{4.3}$$

with the core itself assumed isothermal at $T(M_c)$. Here m_r denotes the mass coordinate and the adiabatic temperature gradient $\nabla_{ad} \equiv \left(\frac{\partial \ln T}{\partial \ln P}\right)_{ad}$ is assumed to be that of the hydrogen-helium mixture alone [3].

Following common choices for models of Saturn's interior (e.g., Nettelmann et al. 2013), the distribution of constituent species with depth follows a three-layer piecewise homogeneous structure: heavy elements are partitioned into a core devoid of hydrogen and helium ($Z = 1$) and a two-layer envelope with outer (inner) heavy element mass fraction Z_1 (Z_2). The helium content is likewise partitioned with outer (inner) helium mass fraction Y_1 (Y_2) subject to the constraint that the mean helium mass fraction of the envelope match the protosolar nebula abundance $Y = 0.275$. The Z and Y transitions are located at a common pressure level P_{12}, a free parameter conceptually corresponding to the molecular-metallic transition of hydrogen, although in SCvH-I itself this is explicitly a smooth transition. We only consider $Z_2 > Z_1$ and $Y_2 > Y_1$ to avoid density inversions and to reflect the natural configuration of a differentiated planet.

The particular choice of this three-layer interior structure model is motivated

[3] This simplification is necessary because the water tables of French et al. (2009) do not provide an entropy column. While these tables have been extended with entropies calculated from separate thermodynamic integrations (N. Nettelmann, private communication), the entropies are accurate only up to an additive offset and so cannot be used to write the total entropy of even an ideal H-He-Z mixture. Within the core where $Z = 1$, the entropy is straightforward to calculate and there we use these extended tables to calculate the sound speed in pure water. See Baraffe et al. (2008b) for a discussion of the significance of heavy elements in setting ∇_{ad} in the envelope.

by the desire for a minimally complicated model that simultaneously (a) satisfies the adopted physically-motivated EOS, (b) includes enough freedom to fit Saturn's low-order gravity field J_2 and J_4, and (c) does not introduce significant convectively stable regions in the envelope, such as those that might arise in cases where composition varies continuously. Requirement (c) precludes a viable class of configurations for Saturn's interior (e.g., Leconte & Chabrier 2013b, Fuller 2014, Vazan et al. 2016b), but it significantly simplifies the formalism and interpretation because in this case the normal modes in the relevant frequency range are limited to the fundamental and acoustic overtone modes. While the isothermal cores of our models are stably stratified and so do admit g–modes, the stratification is such that the maximum $B-V$ frequency attained there is only $N \approx \sigma_0$, where $\sigma_0 = (GM/R)^{1/2}$ is Saturn's dynamical frequency. Since g–modes have frequencies at most N, and f–mode frequencies follow $\sigma \approx \ell^{1/2}\sigma_0$ (Gough 1980), g–modes in such a core will not undergo avoided crossings with the $\ell \geq 2$ f–modes. As will be discussed in §4.5 below, a spectrum of purely acoustic modes is sufficient to explain the majority of the spiral density and bending waves identified in the C ring that appear to be Saturnian in origin.

4.2.1 Gravity field

We generate rigidly rotating, oblate interior models by solving for the shape and mass distribution throughout the interior using the theory of figures formalism (Zharkov & Trubitsyn 1978). The theory of figures expresses the total potential, including gravitational and centrifugal terms, as a series expansion in the small parameter $m_\Omega = \Omega^2 R^3/GM$ where Ω is the uniform rotation rate, R is the planet's volumet-

ric mean radius, and GM is the planet's total gravitational mass. Retaining terms of $\mathcal{O}(m_\Omega^n)$ provides a system of n algebraic equations that describe the shape and total potential as integral functions of the two-dimensional mass distribution, while the mass distribution is in turn related to the potential by the condition of hydrostatic balance. A self-consistent solution for the shape and mass distribution in the oblate model is obtained iteratively, yielding the corresponding gravitational harmonics J_{2n} in the process. To this end we use the shape coefficients given through $\mathcal{O}(m^4)$ by Nettelmann (2017) and implement a similar algorithm. For our Saturn models we adopt $R = 58,232$ km (Seidelmann et al. 2007) and $GM = 37,931,207.7$ cm^3 s^{-2} (Jacobson et al. 2006).

For a given combination of the parameters Z_1, Z_2, Y_1, P_{12}, and m_Ω, an initially spherical model is relaxed to its rotating hydrostatic equilibrium configuration. The mean radii of level surfaces are adjusted during iterations such that the equatorial radius a of the outermost level surface for a converged model matches $a = 60,268$ km following Seidelmann et al. (2007). As the mean radii are adjusted and the densities are recalculated from the EOS, the total mass of the model necessarily changes; therefore the core mass M_c is simultenously adjusted over the course of iterations such that the converged model matches Saturn's total mass. These models include 4096 zones, the algorithm adding zones late in iterations if necessary to speed convergence to the correct total mass.

The values for the gravity used for generating interior models are those of Jacobson et al. (2006), appropriately normalized to our slightly smaller adopted reference equatorial radius according to $J'_{2n} = (a/a')J_{2n}$. Although dramatically more precise

harmonics obtained from the *Cassini* Grand Finale orbits will soon be published, the values of J_2 and J_4 from Jacobson et al. (2006) are already precise to a level beyond that which can be used to put meaningful constraints on the deep interior using our fourth-order theory of figures, where in practice solutions are only obtained with numerical precision at the level of $|\delta J_2/J_2| \approx |\delta J_4/J_4| \lesssim 10^{-4}$.

For the purpose of fitting the gravity field, we create models using $m_\Omega = 0.13963$ corresponding to the 10h 39m 24s (10.657h) rotation period measured from *Voyager* kilometric radiation and magnetic field data by Desch & Kaiser (1981). We sample interior models from a bivariate normal likelihood distribution in J_2 and J_4 using `emcee` (Foreman-Mackey et al. 2013) assuming a diagonal covariance for these gravity harmonics. Because the numerical precision to which our theory of figures can calculate J_2 exceeds its observational uncertainty, the former is used in our likelihood function. We take uniform priors on Z_1 and Z_2 subject to the constraint that $0 < Z_1 < Z_2 < 1$, a uniform prior on $0 < Y_1 < 0.275$, and a uniform prior over 0.5 Mbar $< P_{12} <$ 2 Mbar. The mass distributions and sound speeds for models in this sample are illustrated in Figure 4.1.

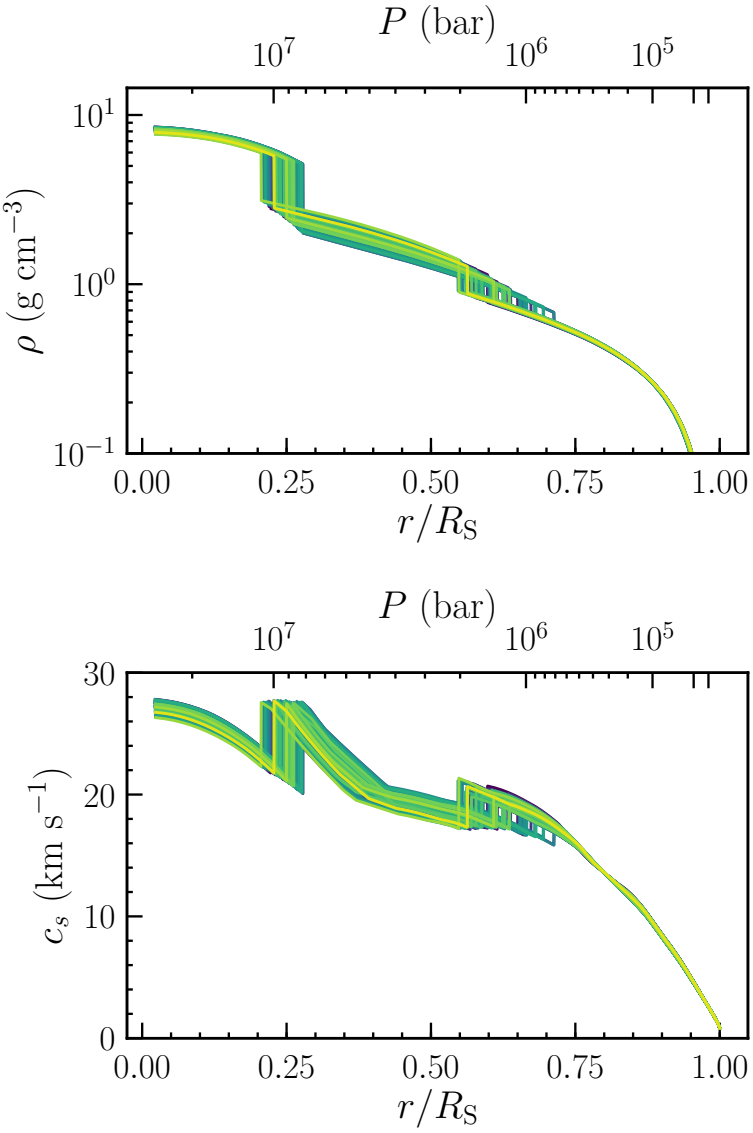

Figure 4.1: Saturn interior models with two-layer envelopes of varying Y and Z distributions, surrounding pure-Z cores. Models are sampled based on J_2 and J_4 from Iess et al. (2019). Mass density (top panel) and sound speed (bottom panel) are shown as functions of the mean radii of level surfaces (bottom horizontal axes) and pressure coordinate (top horizontal axes).

4.3 Mode eigenfrequencies and eigenfunctions

Our approach is to perform the pulsation calculation for spherical models corresponding to the converged theory of figures models, with the various material parameters defined on the mean radii r of level surfaces. The influence of Saturn's rapid rotation is accounted for after the fact using a perturbation theory that expresses the full solutions in the presence of Coriolis and centrifugal forces and oblateness in terms of linear superpositions of the solutions obtained in the non-rotating case.

For spherical models, we solve the fourth-order system of equations governing linear, adiabatic oscillations (Unno et al. 1989) using the open source GYRE stellar oscillation code suite (Townsend & Teitler 2013). The four assumed boundary conditions correspond to the enforcement of regularity of the eigenfunctions at $r = 0$ and the vanishing of the Lagrangian pressure perturbation at the planet's surface $r = R$ (Unno et al. 1989, Section 18.1). The three-layer nature of the interior models considered in this work involve two locations at which the density and sound speed are discontinuous as a result of discontinuous composition changes (see Figure 4.1). Additional conditions are applied at the locations of these discontinuities; these amount to jump conditions enforcing the conservation of mass and momentum across these boundaries.

As will be discussed in §4.5, comparison with the full set of observed waves in the C ring requires f–modes with angular degree in the range $\ell = 2$–14, and we tabulate results through for the f–modes through $\ell = 15$.

In what follows, we adopt the convention that $m > 0$ corresponds to prograde modes—those that propagate in the same sense as Saturn's rotation—so that the time-

dependent Eulerian perturbation to, e.g., the mass density corresponding to the ℓmn normal mode in the planet is written as

$$\rho'_{\ell mn}(r,\theta,\varphi,t) = \rho'_{\ell mn}(r) Y_\ell^m(\theta,\varphi) e^{-i\sigma_{\ell mn} t}, \tag{4.4}$$

where $\sigma_{\ell mn}$ is the mode frequency in the frame rotating with the planet, and r, θ, and φ denote radius, colatitude, and azimuth respectively. Analogous relations hold with the pressure P or gravitational potential Φ in place of density. The $Y_\ell^m(\theta,\varphi)$ are the spherical harmonics, here defined in terms of the associated Legendre polynomials P_ℓ^m as

$$\begin{aligned} Y_\ell^m(\theta,\varphi) =& (-1)^{\frac{m+|m|}{2}} \left[\left(\frac{2\ell+1}{4\pi} \right) \left(\frac{(\ell-|m|)!}{(\ell+|m|)!} \right) \right]^{1/2} \\ & \times P_\ell^m(\cos\theta) e^{im\varphi}. \end{aligned} \tag{4.5}$$

The solution for the displacement itself has both radial and horizontal components, with the total displacement vector given by

$$\begin{aligned} \boldsymbol{\xi}(r,\theta,\varphi,t) = & \left[\xi_r(r)\,\hat{r} + \xi_h(r) \left(\hat{\theta} \frac{\partial}{\partial\theta} + \hat{\varphi} \frac{1}{\sin\theta} \frac{\partial}{\partial\varphi} \right) \right] \\ & \times Y_\ell^m(\theta,\varphi) e^{-i\sigma_{\ell mn} t}. \end{aligned} \tag{4.6}$$

4.3.1 Rotation

In reality, Saturn's eigenfrequencies are significantly modified by the action of Saturn's rapid rotation because of Coriolis and centrifugal forces and the ellipticity of level surfaces. We account for these following the perturbation theory given by

Vorontsov & Zharkov (1981) (see also Saio 1981) and later generalized by Vorontsov (1981) to treat differential rotation, using the eigenfunctions obtained in the non-rotating case as basis functions for expressing the full solutions. In this work we calculate corrected eigenfrequencies for a range of rotation rates, treating Saturn as a rigidly rotating body.

Denoting by $\tilde{\sigma}_{\ell mn}$ the eigenfrequency obtained for the ℓmn mode in the non-rotating case, we write the corrected eigenfrequency as an expansion to second order in the small parameter

$$\lambda \equiv \frac{\Omega_{\rm S}}{\tilde{\sigma}_{\ell mn}} \tag{4.7}$$

so that the corrected frequency as seen in inertial space is given by

$$\sigma_{\ell mn} = \tilde{\sigma}_{\ell mn} \left[1 + \sigma_{\ell mn,1}\lambda + \sigma_{\ell mn,2}\lambda^2 + \mathcal{O}(\lambda^3)\right] . \tag{4.8}$$

For Saturn's f–modes, $\lambda \approx 0.3$ for $\ell = 2$ and decreases to $\lambda \approx 0.1$ by $\ell = 15$. The dimensionless factor $\sigma_{\ell mn,1}$ includes the effects of the Coriolis force and the Doppler shift out of the planet's rotating reference frame. $\sigma_{\ell mn,2}$ includes the effects of the centrifugal force and ellipticity of the planet's figure as a result of rotation. In the limit of slow rotation, it is appropriate to truncate the expansion at first order in λ, in which case Equation 4.8 reduces to the well-known correction of Ledoux (1951) in which the Coriolis force breaks the frequency's degeneracy with respect to the azimuthal order m.

Expressions for $\sigma_{\ell mn,1}$ and $\sigma_{\ell mn,2}$ are obtained through the perturbation theory; in practical terms they are inner products involving the zeroth-order eigenfunctions

and operators describing the Coriolis and centrifugal forces and ellipticity. Corrections related to the distortion of equipotential surfaces require knowledge of the planetary figure as a function of depth, and these are provided directly by the theory of figures as described in §4.2.1.

This formalism is constructed to retain the separability of eigenmodes in terms of the spherical harmonics Y_ℓ^m, so that each corrected planet mode may still be uniquely specified by the integers ℓ, m and n and the expressions 4.4 and 4.6 hold for the corrected eigenfunctions. Generally speaking, distinct modes whose frequencies are brought into close proximity by the perturbations from rotation may interact, yielding modes of mixed character. In the second-order theory applied to rigid rotation, selection rules limit these interactions to pairs of modes with the same m and with ℓ differing by -2, 0, or $+2$. Vorontsov & Zharkov (1981) found that for f– and p–modes with $\ell \leq 8$ these additional frequency perturbations do not exceed 0.5%, roughly an order of magnitude smaller than the second-order corrections themselves, and indeed generally smaller than the truncation error associated with neglecting higher-order correction terms (see below). There is thus little to be gained from incorporating mode-mode interactions given the accuracy of the present theory, but mode-mode interactions could be meaningfully taken into account in a third-order perturbation theory. The present work neglects mode-mode interactions.

Further details on the calculation of these rotation corrections are given by Marley (1990), which the present implementation follows closely[4]. The interior density

[4]Marley (1990) corrected several typographical errors from Vorontsov & Zharkov (1981) and Vorontsov (1981), and one error was introduced: Equation (A1.27) for the ellipticity correction I_5 is missing a factor of two in the second term.

and sound speed discontinuities described above necessitate additional second-order corrections accounting for the ellipticity of these transitions and the gravitational potential perturbation felt throughout the planet as a result (Vorontsov & Zharkov 1981, Section 5).

Equation 4.8 provides the mode frequency as seen in inertial space. This frequency can in turn be related to a pattern speed—the rotation rate of the full m-fold azimuthally periodic pattern—according to

$$\Omega_{\rm pat} = \frac{1}{m}\sigma_{\ell mn}, \tag{4.9}$$

which is suitable for direct comparison with the pattern speeds observed for waves in the rings. For completeness, the mode frequency in the planet's corotating frame is related to the frequency seen in inertial space by

$$\sigma_{\ell mn} = \sigma^{\rm corot}_{\ell mn} + m\Omega_{\rm S} \tag{4.10}$$

i.e., modes that are prograde in the planet's frame ($m > 0$) modes appear to have larger frequencies in inertial space as a result of Saturn's rotation.

As an illustration of the relative importance of these various contributions to the modeled pattern speed, we may substitute the frequency expansion 4.8 into 4.9 to write

$$\Omega_{\rm pat} = \frac{\tilde{\sigma}_{\ell mn}}{m} + \frac{\sigma_{\ell mn,1}\Omega_{\rm S}}{m} + \frac{\sigma_{\ell mn,2}\Omega_{\rm S}^2}{m\tilde{\sigma}_{\ell mn}}. \tag{4.11}$$

These three contributions are shown in Figure 4.2, which demonstrates that the second-

order rotation corrections affect the pattern speeds at the level of $\gtrsim 50$ deg day^{-1} for modes with ℓ below 15. These corrections are thus essential for comparison with the observed wave pattern speeds, whose uncertainties are no larger than approximately 0.1 deg day^{-1} (P.D. Nicholson, private communication).

Higher order terms in the series expansion are potentially also significant. A third-order theory would include in the expansion 4.11 a λ^3 term

$$\Omega_{\rm pat}^{(3)} \equiv \frac{\sigma_{\ell mn,3}\Omega_{\rm S}^3}{m\tilde{\sigma}_{\ell mn}^2}, \tag{4.12}$$

where the nondimensional prefactor $\sigma_{\ell mn,3}$ involves significant mathematical complexity (Soufi et al. 1998; Karami 2008). To establish an upper limit for the magnitude of third-order corrections, noting that $|\sigma_{\ell mn,2}| < |\sigma_{\ell mn,1}|$ for all modes we consider, we suppose that similarly $|\sigma_{\ell mn,3}| \leq |\sigma_{\ell mn,2}|$ and thus adopt $|\sigma_{\ell mn,3}| = |\sigma_{\ell mn,2}|$ as an upper limit. The resulting upper limits on third-order contributions to f–mode pattern speeds are indicated in Figure 4.2, which demonstrates that the truncation error associated with our second-order theory may be as large as 30 deg day^{-1} for $\ell = m = 2$, but decaying with increasing m. As discussed §4.5 below, these error estimates are taken into account in our analysis to ensure that the systematic dependence of the truncation error on m does not bias our estimate of Saturn's bulk rotation rate.

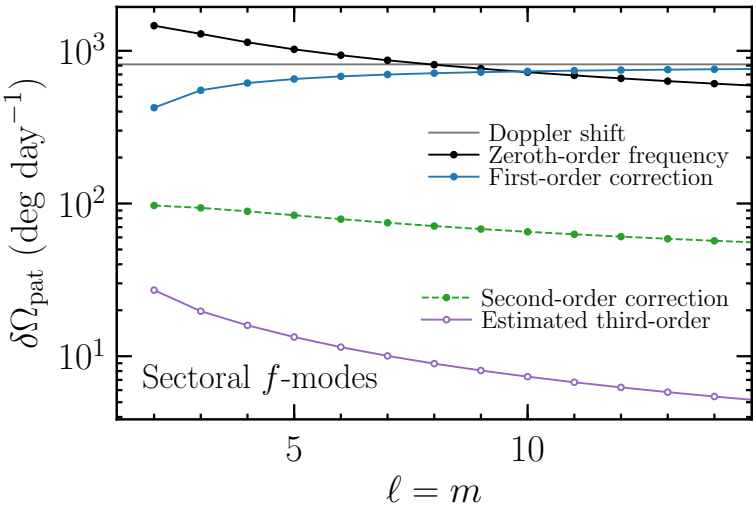

Figure 4.2: Magnitude of the contributions made to the modeled pattern speed by each of the four terms in Equation 4.11, as well as the estimate (4.12) for the magnitude of third-order corrections. For these prograde modes the first-order corrections (Doppler plus Coriolis; blue solid curve) take positive values, the second-order corrections (centrifugal force and ellipticity; green dashed curve) take negative values, and the estimated third-order intrinsic corrections (purple solid curve) have no assumed sign.

4.4 Saturnian f–modes in the rings

This section briefly summarizes the formalism (Marley & Porco 1993) connecting Saturn's nonradial oscillations with orbital resonances in the rings.

4.4.1 Resonance conditions

The condition for a Lindblad resonance is (Goldreich & Tremaine 1979)

$$m(\Omega - \Omega_{\rm pat}) = \pm q\kappa \tag{4.13}$$

with the upper sign corresponding an inner Lindblad resonance (ILR) and the lower sign corresponding to an outer Lindblad resonance (OLR), and with q a positive integer.

Taking the lower sign in Equation 4.13 to consider an OLR, it physically represents the condition that the perturbing pattern overtakes an orbiting ring particle once every m/q epicycles. This prograde forcing in phase with the ring particles' epicycles leads to a deposition of angular momentum that may launch a spiral density wave propagating toward the planet, assuming self-gravity is the relevant restoring force. At an ILR an orbiting particle instead overtakes the slower perturbing pattern once every m/q epicycles, leading to a removal of angular momentum that may launch a spiral density wave that propagates away from the planet. Such waves are common in Saturn's rings at mean motion resonances with Saturnian satellites.

Vertical resonances satisfy an analogous condition, namely that the perturbing pattern speed relative to the ring orbital frequency is simply related to the characteristic vertical frequency μ in the rings:

$$m(\Omega - \Omega_{\rm pat}) = \pm b\mu, \tag{4.14}$$

where b is a positive integer and the vertical frequency $\mu(r)$ in the ring plane can be obtained from (Shu et al. 1983)

$$\mu^2 + \kappa^2 = 2\Omega^2. \tag{4.15}$$

As with Lindblad resonances, there exist both inner and outer vertical resonances (IVRs and OVRs), depending on the sign of $\Omega - \Omega_{\rm pat}$. Self-gravity waves excited at vertical resonances generally propagate in the opposite sense from those excited at Lindblad

resonances, so that bending waves at IVRs propagate toward the planet and those at ILRs propagate away. IVRs are common in the rings as a result of Saturnian satellites, namely those whose inclinations provide resonant vertical forcing.

In the above, the positive integer q or b is sometimes referred to as the 'order' of the resonance. This work focuses on first-order ($q = 1$ or $b = 1$) resonances; higher-order resonances are possible (Marley 2014) but the wave structures they produce may destructively interfere (P.D. Nicholson, private communication) and these resonances do not appear to need to be invoked to explain the present data (see §4.5 below). Furthermore, in what follows we limit our attention to OLRs and OVRs because in practice, the prograde f–modes of modest angular degree have pattern speeds that exceed $\Omega(r)$ throughout the C ring.

The orbital and epicyclic frequencies Ω and κ for orbits at low inclination and low eccentricity can generally be written as a multipole expansion in terms of the zonal gravitational harmonics J_{2n}, namely

$$\Omega^2(r) = \frac{GM}{r^3}\left[1 + \sum_{n=1}^{\infty} A_{2n} J_{2n} \left(\frac{a}{r}\right)^{2n}\right] \tag{4.16}$$

and

$$\kappa^2(r) = \frac{GM}{r^3}\left[1 + \sum_{n=1}^{\infty} B_{2n} J_{2n} \left(\frac{a}{r}\right)^{2n}\right], \tag{4.17}$$

with the J_{2n} values scaled to the appropriate reference equatorial radius a. The A_{2n} and B_{2n} are rational coefficients and are tabulated by Nicholson & Porco (1988). We

use the even harmonics of Iess et al. (2019) through J_{12} for the purposes of locating resonances in the ring plane, although the gravity field only affects radial locations of resonances and has no bearing on f–mode pattern speeds. We therefore use the latter for quantitative comparison between model f–modes and observed waves.

The above relations constitute a closed system allowing the comparison of planet mode frequencies to the frequencies of waves observed at resonances in the rings. In cases where we do compare resonance *locations*, the resonant radius for a Lindblad or vertical resonance is obtained by numerically solving Equation 4.13 or 4.14.

4.4.2 Which modes for which resonances?

Each planet mode can generate one of either density waves or bending waves. The type of wave that the ℓmn mode is capable of driving depends on its angular symmetry, and in particular the integer $\ell - m = (0, 1, 2, 3, \ldots)$. Modes with even $\ell - m$ are permanently symmetric with respect to the equator, and so are not capable of any vertical forcing. However, they are antisymmetric with respect to their azimuthal nodes, and so do contribute periodic azimuthal forcing on the rings. The reverse is true of modes with odd $\ell - m$, whose perturbations are antisymmetric with respect to the equator and so do contribute periodic vertical forcing on ring particles. Meanwhile their latitude-average azimuthal symmetry as experienced at the equator prevents them from forcing ring particles prograde or retrograde.

In what follows, we restrict our attention to prograde f–modes, namely the normal modes with $m > 0$ and $n = 0$. Acoustic modes with overtones ($n > 0$; p–modes) are not considered because that they contribute only weakly to the external potential

perturbation due to self-cancellation in the volume integral of the Eulerian density perturbation; see Equation A.11. We further limit our consideration to prograde modes because while f–modes that are retrograde in the frame rotating with the planet can in principle be boosted prograde by Saturn's rotation (see Equation 4.10), we find that the resulting low pattern speeds ($\lesssim 500$ deg day^{-1}) would place any Lindblad or vertical resonances beyond the extent of even the A or B rings. Finally, azimuthally symmetric ($m = 0$) modes do not lead to Lindblad or vertical resonances.

4.5 Results for rigid rotation

Figure 4.3 summarizes the OLR and OVR locations of prograde model Saturn f–modes with $\ell - m$ between zero and five, together with locations of 17 inward-propagating density waves and four outward-propagating bending waves observed in *Cassini* VIMS data. A visual comparison in this diagram provides a strong indication that the f–modes are responsible for the majority of the wave features shown. In particular, we can make unambiguous identifications for the f–modes at the origin of 10 of the 17 density waves, and all four of the bending waves; these visual identifications are summarized in Table 4.5.

The remaining seven density waves at $m = 2$ and $m = 3$ exhibit frequency splitting that is likely attributable to mixing with deep g–modes as proposed by Fuller (2014), and which our model, lacking a stable stratification outside the core, does not attempt to address. We thus omit all $m = 2$ and $m = 3$ waves from the quantitative analysis that follows, although we note that the predicted $\ell = m = 2$ and $\ell = m = 3$

f–mode OLR locations do generally coincide with the locus of observed density waves for these m values, the sole exception being the close-in W76.44. This wave was only recently detected in VIMS data (French et al. 2019), and while coupling with deep g–modes is a possible interpretation (E. Dederick, private communication), this wave may be particularly challenging to explain due to its large splitting from the other three $m = 2$ waves. We also note that the frequency and m value of the outermost $m = 2$ density wave in the ringlet within the Maxwell gap (French et al. 2016) were predicted by Fuller (2014).

As discussed in §4.3, the density and sound speed discontinuities inherent to the three-layer interior structures assumed for Saturn affect the f–mode frequencies. Their effect is strongest for the lowest-degree f–modes, which have significant amplitude at these deep transitions. This is evident in Figure 4.3 in the considerable spread of predicted locations for resonances with the $\ell = \{2, 3\}$ f–modes. By $\ell \gtrsim 4$ the f–modes have low enough amplitudes at these deep density transitions that their frequencies are not strongly affected.

The model f–modes whose resonance locations coincide with the remainder of the observed waves contain a striking range of radial and latitudinal structures, including the rest of the sectoral ($\ell = m$) sequence up to $\ell = m = 10$, as well as seven non-sectoral ($\ell \neq m$) modes with $\ell - m = \{1, 2, 3, 4, 5\}$. These waves are evidently the result of time-dependent tesseral harmonics resulting from Saturn's nonradial oscillations.

Although general agreement for these is evident at the broad scale of Figure 4.3, the observed wave pattern speeds are known to a precision better than 0.1 deg day^{-1}

for the weakest waves yet measured (P. D. Nicholson, private communication). This high precision warrants a closer inspection of the pattern speed residuals with respect to our predictions. What follows in the remainder of this section is an analysis of these residuals and their dependence on the assumed interior model and rotation rate.

4.5.1 Saturn's seismological rotation rate

Saturn's bulk rotation rate has to date been deduced from a combination of gravity field and radiometry data from the Pioneer, *Voyager* and *Cassini* spacecrafts (e.g., Desch & Kaiser 1981, Gurnett et al. 2005, Giampieri et al. 2006, Anderson & Schubert 2007). Along different lines, Helled et al. (2015) optimized interior models to the observed gravity field and oblateness to extract the rotation rate. Since we have demonstrated that the frequencies of Saturnian f–modes depend strongly on $\Omega_{\rm S}$ through the influence of the Coriolis and centrifugal forces and the ellipticity of level surfaces, a natural question is, what interior rotation rate is favored by the waves detected so far that appear to be associated with modes in Saturn's interior?

Given an observed C ring wave with a pattern speed $\Omega_{\rm pat}^{\rm obs}$ that appears to be associated with a predicted Saturn model f–mode resonance with pattern speed $\Omega_{\rm pat}$ and azimuthal order matching the observed number of spiral arms m, we calculate the pattern speed residual $\Delta\Omega_{\rm pat} \equiv \Omega_{\rm pat} - \Omega_{\rm pat}^{\rm obs}$. For each Saturn interior model and rotation rate considered, we calculate a weighted root-mean-square (RMS) value of $\Delta\Omega_{\rm pat}$ over

Table 4.1: C ring wave patterns and Saturn f–mode associations

			Observed			Model prediction		
Reference[a]	Wave	Symbol[b]	m	$\Omega_{\rm pat}$[c]	Type	ℓ	$\Omega_{\rm pat}$[c]	$\Delta\Omega_{\rm pat}$ (model − obs)[c]
F+18	W76.44[d]	□	2	2169.3	OLR	—	—	—
HN13	W84.64[d]	♢	2	1860.8	OLR	—	—	—
HN13	W87.19[d]	♢	2	1779.5	OLR	—	—	—
F+16	Maxwell[d]	△	2	1769.2	OLR	—	—	—
HN13	W82.00[d]	♢	3	1736.7	OLR	—	—	—
HN13	W82.06[d]	♢	3	1735.0	OLR	—	—	—
HN13	W82.21[d]	♢	3	1730.3	OLR	—	—	—
HN13	W80.98	♢	4	1660.4	OLR	4	1657.87–1673.41	−2.49–13.05
H+18	W81.02a	▽	5	1593.6	OLR	5	1592.08–1596.05	−1.54–2.43
H+18	W81.43	▽	6	1538.2	OLR	6	1537.10–1539.51	−1.13–1.28
H+18	W81.96	▽	7	1492.5	OLR	7	1491.73–1493.72	−0.73–1.26
F+18	W76.46	□	7	1657.7	OLR	9	1655.86–1657.35	−1.86 to −0.37
H+18	W82.53	▽	8	1454.2	OLR	8	1453.93–1455.23	−0.30–1.00
H+18	W83.09	▽	9	1421.8	OLR	9	1421.83–1422.55	−0.01–0.71
F+18	W76.02	□	9	1626.5	OLR	13	1626.48–1627.46	−0.02–0.96
HN14	W83.63	♢	10	1394.1	OLR	10	1394.03–1394.71	−0.03–0.65
H+18	W81.02b	▽	11	1450.5	OLR	13	1451.53–1453.07	1.04–2.58
F+18	W74.93	□	4	1879.6	OVR	5	1871.22–1875.42	−8.42 to −4.22
F+18	W74.67	□	7	1725.8	OVR	10	1723.99–1725.28	−1.77 to −0.48
F+18	W76.24	□	8	1645.4	OVR	11	1644.89–1645.81	−0.54–0.38
F+18	W74.94	□	9	1667.7	OVR	14	1667.72–1668.85	−0.01–1.12

[a] HN13 denotes Hedman & Nicholson (2013), HN14: Hedman & Nicholson (2014), F+16: French et al. (2016), H+18: Hedman et al. (2019), F+18: French et al. (2019).

[b] cf. Figure 4.3

[c] deg day^{-1}

[d] Member of a multiplet of waves of the same type having the same m but different frequencies, probably the result of resonant coupling between the f–mode of the same m identified here and a deep g–mode as demonstrated by Fuller (2014). Thus no unambiguous identification with our pure f–mode predictions is possible. See discussion in §4.5; for the relevant $\ell = m = 2$ f–mode we predict $1743.34 - 1845.28$ deg day^{-1} and for the $\ell = m = 3$ f–mode we predict $1729.29 - 1777.28$ deg day^{-1}.

the set of mode-wave pairs according to

$$\text{RMS } \Delta\Omega_{\rm pat} \equiv \left[\sum_i w_i \left| \Delta\Omega_{\rm pat,\,i} \right|^2 \right], \tag{4.18}$$

where the weights w_i are assigned in inverse proportion with the maximum magnitude of third-order corrections as described in §4.3.1, the weights sum to unity, and i indexes the set of waves that we have identified with Saturn f–modes, namely those with ℓ values and model pattern speeds listed in Table 4.5. The resulting curves are shown in Figure 4.4 for rotation periods between 10h 30m and 10h 42m. The relation between RMS $\Delta\Omega_{\rm pat}$ and $\Omega_{\rm S}$ always exhibits a distinct minimum, owing to the strongly correlated response of the f–mode frequencies to varying $\Omega_{\rm S}$. In particular, the predicted pattern speeds increase uniformly with faster Saturn rotation.

The optimal Saturn rotation period depends on the interior model chosen, as does the quality of that best fit: interior models favoring longer rotation periods generally achieve a slightly better bit. To account for this in our esimate of Saturn's bulk rotation period, we weight the optimized rotation period from each interior model in inverse proportion to the value of RMS $\Delta\Omega_{\rm pat}$ obtained there. The cumulative distribution of rotation rates resulting from our sample of interior models is shown in Figure 4.4. This distribution may be summarized as $P_{\rm S} = 10.561^{+0.031}_{-0.022}\,{\rm h} = 10{\rm h}\,33{\rm m}\,38{\rm s}^{+1{\rm m}\,52{\rm s}}_{-1{\rm m}\,19{\rm s}}$ where the leading value corresponds to the median and the upper (lower) error corresponds to the 95% (5%) quantile. This may be expressed in terms of a pattern speed as $2\pi/P_{\rm S} = 818.13^{+2.41}_{-1.70}\,{\rm deg\ day}^{-1}$.

Although these seismological calculations vary the assumed rotation rate, the

underlying interiors randomly sampled against J_2 and J_4 using the theory of figures as described in §4.2.1 assumed the Desch & Kaiser (1981) *Voyager* rate, in principle an inconsistency of the model. As a diagnostic we generate a new sample from the gravity field, but adopting $m_\Omega = 0.14201$ consistent with the 10.561h median rotation period derived here. Repeating the remainder of this analysis we find a very similar distribution of optimal rotation periods, the median shifting to longer periods by approximately one minute as a result of the slightly different interior mass distributions obtained. The frequencies of the f–modes themselves are inherently more sensitive to Saturn's assumed rotation rate than are the low-order gravity harmonics J_2 and J_4, a consequence of the f–modes extending to relatively high m where Saturn's rotation imparts a larger fractional change to the frequency (see Figure 4.2).

4.5.2 Is rigid rotation adequate?

The lack of any perfect fit among the range of interior structures and rotation rates we have considered is evident in Figure 4.4, where the RMS pattern speed residuals reach approximately 1.2 deg day^{-1} at best, an order of magnitude larger than the typical observational uncertainty of approximately 0.1 deg day^{-1} associated with even the weakest waves we compare to here (P.D. Nicholson, private communication). The absolute residuals are shown mode by mode in Figure 4.5, including the full span of residuals obtained over the sample of interior models, each one evaluated at its optimal rotation rate. Points lie on both sides of zero by construction, but again no model provides an entirely satisfactory fit.

First, it is notable that the model pattern speed covariance (the diagonal ele-

ments of which set the vertical spans in the residuals of Figure 4.5) varies so strongly and non-monotonically with m. This can be understood as a consequence of the trade-off between the decreasing zeroth-order frequency and the increasing contribution from the first-order rotation correction with increasing ℓ, as can be seen from Figure 4.2 for the sectoral modes. At high ℓ, the zeroth-order frequency loses out to the first-order correction. Since the latter is proportional to Ω_S, the overall pattern speeds vary more strongly with rotation than at intermediate ℓ. At low ℓ, where the frequency is dominated by the zeroth order contribution and so rotation plays a smaller role, the large model covariance is due mostly to sensitivity to the locations of the core boundary and envelope transition, sensitivity that decays rapidly with increasing ℓ as modes are confined increasingly close to the planet's surface.

A significant observational development has been made by Hedman et al. (2019) in their detection of density waves corresponding to the full set of Saturn's sectoral f–modes from $\ell = m = 2$ up to $\ell = m = 10$, constituting frequency measurements for modes that possess the same latitudinal symmetry but sample an uninterrupted sequence of depths within Saturn. On the other hand, the non-sectoral ($\ell \neq m$) f–mode waves reported by Hedman et al. (2019) and French et al. (2019) extend the detections up to $\ell = 14$ but also importantly sample a variety of *latitudinal* structures inside the planet by virtue of the range in their values of $\ell - m$. Thus in principle the available modes serve to constrain differential rotation inside Saturn.

With this in mind, the second panel of Figure 4.5 is a valuable illustration because any strong differential rotation as a function of depth or latitude would gen-

erally manifest as systematic trends in the residuals $\Delta\Omega_{\rm pat}$ as a function of ℓ or $\ell - m$ respectively when referred to the rigid model. Instead, the residuals exhibit no obvious systematic dependence on ℓ, although small systematic departures as a function of $\ell - m$ may indicate the presence of differential rotation as a function of latitude. In particular, in each of the four cases where two modes belonging to the same multiplet have been observed ($\ell = 5,\ 9,\ 10,$ and 13), the two frequencies are offset by between 1 and 5 deg day^{-1}.

More firm conclusions regarding the presence or strength of differential rotation are not possible given the present theoretical accuracy limitations discussed in §4.3.1. A more accurate treatment of rotation effects could potentially increase the predicted pattern speeds of the low-m modes by as many as tens of deg day^{-1} (see Figure 4.2) which could produce a spectrum consistent with a spin frequency increasing by several percent toward the planet's surface. Indeed, this systematic uncertainty motivates the weighted fit that we carry out in our estimate of Saturn's bulk rotation in §4.5.1. Ultimately a more accurate perturbation theory, or else non-perturbative methods (e.g., Mirouh et al. 2018), will be required to fully interpret the implications for differential rotation inside Saturn.

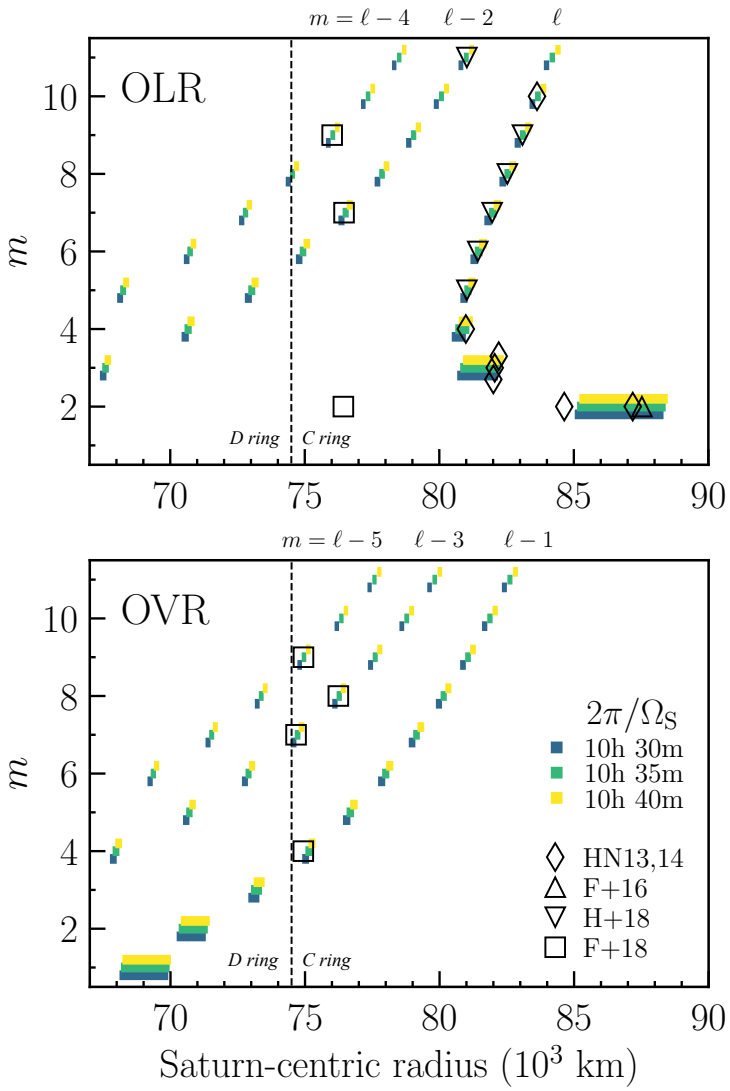

Figure 4.3: Locations of resonances with our model Saturn's f–modes (colorful horizontal spans) and wave features observed in Saturn's C ring using stellar occultations in *Cassini* VIMS data (open symbols; see references in Table 4.5). The number of spiral arms m (or equivalently, the azimuthal order of the perturbing planet mode) is shown versus distance from Saturn's center in the ring plane. *Top panel:* Outer Lindblad resonances, which can excite inward-propagating spiral density waves in the rings. The three roughly vertical model sequences correspond to modes with $m = \ell$, $m = \ell - 2$, and $m = \ell - 4$ from right to left. The three observed $m = 3$ density waves are offset vertically for clarity. *Right panel:* Outer vertical resonances, which can excite outward-propagating bending waves in the rings. The three vertical model sequences correspond to $m = \ell - 1$, $m = \ell - 3$, and $m = \ell - 5$ from right to left. Model resonances are colored by the assumed Saturn rotation rate as described in the legend; the resonances indicated for each rotation rate are slightly offset vertically for clarity.

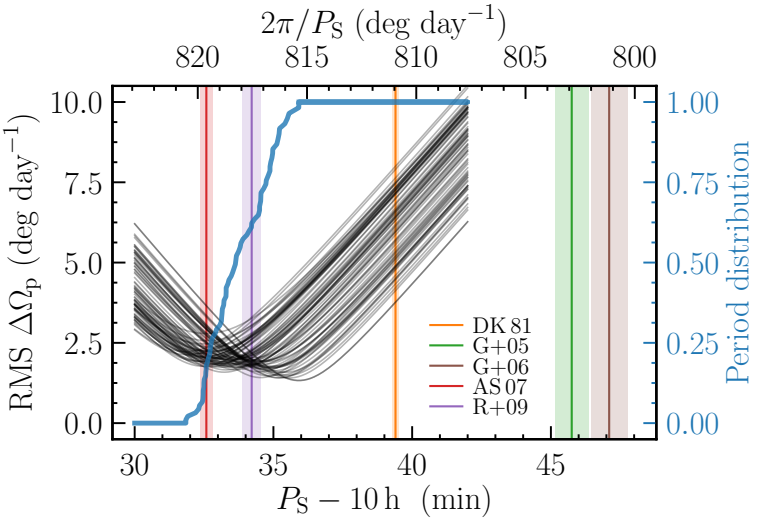

Figure 4.4: Saturn's rotation rate from fits to the set of observed C ring waves identified with Saturnian f–modes. RMS pattern speed residuals across the full set of waves are shown as a function of Saturn's assumed rotation rate. Each black curve corresponds to a single interior model from the sample shown in Figure 4.1. The thick blue curve shows the cumulative distribution of rotation periods minimizing the weighted RMS pattern speed residuals for each model; its median and 5%/95% quantiles are given in §4.5.1. Vertical lines with shaded errors indicate Saturn rotation rates in the literature, references to which are given in the text. For visual clarity the Helled et al. (2015) result of 10h 32m (45 ± 46)s referred to in the text is omitted from the diagram.

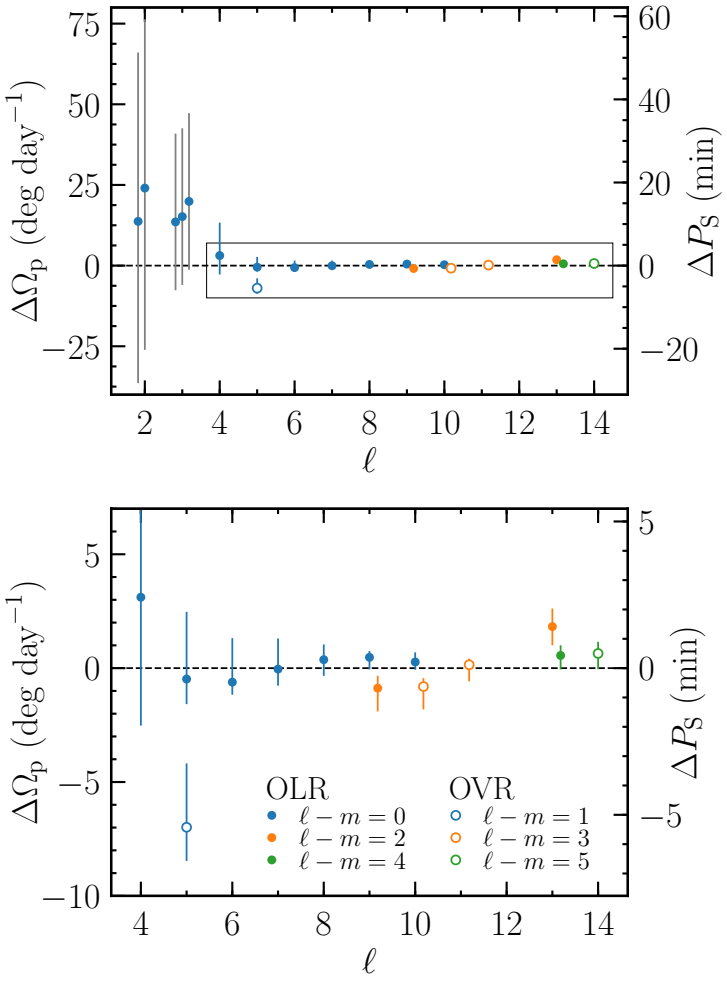

Figure 4.5: Pattern speeds residuals (predicted minus observed) for models each calculated at their optimal Saturn rotation period. *Top panel:* All residual frequencies, including those for the $m = 2$ and $m = 3$ sectoral f–modes for which identification with specific $m = 2$ or $m = 3$ density waves is not possible. For these modes residuals are shown with respect to each of the nearby density waves having the correct m value. The domain of the right panel is indicated. *Bottom panel:* Frequency residuals for the 14 waves identified with Saturn f–modes and used to constrain Saturn's rotation. Circular markers are for one interior model randomly chosen from our sample, while vertical lines show the span of residuals obtained for the full sample. These vertical spans thus indicate the amount of freedom available from the low-order gravity field as applied to three-layer Saturn models, when the rotation rates are tuned using the seismology. Note that these spans do not represent random uncertainties because the residuals for the various modes are highly correlated. The vertical axis at right expresses the residuals in terms of minutes of Saturn rotation, i.e., the degree to which Saturn would need to be spun up or down to fit a given wave's observed pattern speed. Four pairs of modes that are members of same-ℓ multiplets are evident (see discussion in §4.7); the pairs with $\ell = 9$, 10, and 13 are slightly offset horizontally for clarity.

4.6 Strength of forcing

The adiabatic eigenfrequency calculation that forms the basis for this work provides no information about excitation or damping of normal modes, processes which have yet to be adequately understood in the context of gas giants.

Stochastic excitation of modes by turbulent convection such as in solar-type oscillations is one obvious candidate for Jupiter and Saturn, where convective flux dominates the intrinsic flux in each planet. However, the expectation from simple models for resonant coupling of f– and p–modes with a turbulent cascade of convective eddies (e.g., Markham & Stevenson (2018) following the theory of Kumar (1997)) is that these modes are not excited to the amplitudes necessary to provide the mHz power excess that Gaulme et al. (2011) attributed to Jovian p–modes.

Recent work from Dederick & Jackiewicz (2017) demonstrated that a radiative opacity mechanism is not able to drive the Jovian oscillations, although they noted that driving by intense stellar irradiation is possible for hot Jupiters. Dederick et al. (2018) and Markham & Stevenson (2018) each focused on water storms as a mode excitation mechanism, finding this too insufficient for generating a power spectrum akin to that reported by Gaulme et al. (2011). Markham & Stevenson (2018) further demonstrated that deeper, more energetic storms associated with the condensation of silicates were viable.

In lieu of a complete understanding of the amplitudes of acoustic modes in gas

giants, we simply adopt equal mode energy across the f–mode spectrum following

$$E_{\ell mn} \propto \sigma_{\ell mn}^2 |\boldsymbol{\xi}|^2 = \text{constant}, \tag{4.19}$$

corresponding to the "strong coupling" case cited by Marley & Porco (1993). Less efficient coupling of the turbulence with the f–modes could result in a steeper decline of equilibrium mode energy with frequency; Marley & Porco (1993) adopted $E_{\ell mn} \propto \sigma_{\ell mn}^{-13/2}$ as a limiting case.

Because the scaling relation 4.19 is only a proportionality, it remains to set an overall normalization by choosing the amplitude of a single mode. Marley & Porco (1993) proposed that the $\ell = m = 2$ f–mode OLR is the origin of the Maxwell gap, and accordingly anchored their amplitude spectrum by assuming that this mode had an amplitude sufficient to produce the OLR torque $T^L/\Sigma \sim 10^{16}$ cm^4 s^{-2} necessary to open a gap (Rosen et al. 1991a). The corresponding displacement amplitude was of order 100 cm; we follow suit and adopt 100 cm as the amplitude of this mode[5].

In what follows we normalize our f–mode eigenfunctions in accordance with the amplitude estimate of Equation 4.19 and derive the resulting torques applied at OLRs and OVRs. While this amplitude law is but one of many plausible scenarios, any similar scaling relation will yield the same general dependence of Lindblad and vertical torques on ℓ, m, and position in the ring plane. In particular, the magnitudes of the

[5]While the connection between the $\ell = m = 2$ f–mode and the Maxwell gap itself has yet to be fully understood, it is tantalizing as this mode yields the largest gravity perturbations out of any of Saturn f–modes for any simple amplitude spectrum (see §4.6.1). Furthermore, the ringlet within the gap harbors an $m = 2$ density wave (French et al. 2016) as predicted from the Saturn mode spectrum calculated by Fuller (2014).

torques decline monotonically with ℓ for a given $\ell - m$, and also with $\ell - m$ for a given m. This is sufficient for a basic prediction of the *relative* strengths of waves at the f–mode resonances calculated here, which will allow us to identify locations that may harbor hitherto-undetected waves.

4.6.1 Torques and detectability

In deriving the magnitudes of torques applied at ring resonances we follow the approach of Marley & Porco (1993). In a ring of surface mass density Σ, the linear torque applied at a Lindblad resonance is (Goldreich & Tremaine 1979)

$$T^L_{\ell mn} = -\frac{m\pi^2\Sigma}{\mathscr{D}_L}(2m+\ell+1)\left(\Phi'_{\ell mn}\right)^2, \tag{4.20}$$

where

$$\begin{aligned}\mathscr{D}_L = &-\left(3 - \frac{9}{2}J_2\left(\frac{a}{r_L}\right)^2\right)\Omega^2(1\mp m)\\ &+\frac{21}{2}J_2\left(\frac{a}{r_L}\right)^2\Omega^2 + \mathcal{O}(J_2^2, J_4)\end{aligned} \tag{4.21}$$

and $\Phi'_{\ell mn}$ is the magnitude of the perturbation to the gravitational potential caused by the ℓmn mode, evaluated at the Lindblad resonance $r = r_L$ in the ring plane $\cos\theta = 0$. Similarly the linear torque applied at a vertical resonance $r = r_V$ is (Shu et al. 1983; Marley & Porco 1993)

$$T^V_{\ell mn} = \frac{m\pi^2\Sigma}{\mathscr{D}_V}\left(\frac{d\Phi'_{\ell mn}}{d\theta}\right)^2, \tag{4.22}$$

where

$$\mathscr{D}_V = -\left(3 + \frac{9}{2}J_2\left(\frac{a}{r_V}\right)^2\right)\Omega^2(1 \mp m) - \frac{21}{2}J_2\left(\frac{a}{r_V}\right)^2\Omega^2 + \mathcal{O}(J_2^2, J_4) \tag{4.23}$$

and $(d\Phi'_{\ell mn}/d\theta)$ is to be evaluated at the vertical resonance $r = r_V$ and $\cos\theta = 0$. In the expressions for $\mathscr{D}_L$ and $\mathscr{D}_V$ the upper (lower) signs correspond to inner (outer) Lindblad or vertical resonances, as in Equations 4.13 and 4.14. An expression for $\Phi'_{\ell mn}$ is derived as in Marley & Porco (1993); this is reproduced in Appendix A for completeness. These expressions rely on integrals of the Eulerian density perturbation $\rho'_{\ell mn}$ over the volume of the planet. While accuracy to second order in Saturn's smallness parameter m_Ω would demand that this density eigenfunction include second-order corrections from the perturbation theory described in §4.3.1, the fact that only an order of magnitude calculation of the torques is required for the present purpose leads us to simply calculate these using the zeroth-order density eigenfunctions.

To illustrate which modes are likely to excite the strongest ring features, Figure 4.6 summarizes the torques applied by the f–modes at OLRs and OVRs in the C and D rings assuming mode amplitudes follow equipartition per Equation 4.19. Because the torques (Equations 4.20 and 4.22) are proportional to ring surface mass density Σ, itself strongly variable across the rings at a variety of spatial scales, we instead plot the normalized torques T_L/Σ and T_V/Σ. These are straightforward quantities to calculate even with imperfect knowledge of the mass density itself. When comparing to detected wave patterns should be kept in mind that Σ can play an important role in whether a

given wave is likely to be driven to detectable amplitudes.

Saturnian waves can also be obscured by more prominent eccentric features, such as those associated with satellite resonances. Of particular importance is the strong Titan 1:0 apsidal resonance, which Nicholson et al. (2014) studied in *Cassini* radio and stellar occultations and found responsible for driving the $m = 1$ wave in the Titan/Colombo ringlet (77,879 km) and also dozens of other $m = 1$ features from 74,000-80,000 km. Their test-particle model (cf. their Figure 19) predicts maximum radial deviations in excess of 100 m as much as 3,500 km away from that resonance, posing a serious challenge for the reconstruction of weaker wave features from stellar occultation profiles obtained at different phases. This substantial region of the C ring thus may be concealing waves driven at Saturn resonances, and Figure 4.6 accordingly indicates the region where the maximum radial deviations are larger than 300 m according to the model of Nicholson et al. (2014).

For context, the torques associated with four satellite resonances that open gaps or launch waves in the C ring are also shown in Figure 4.6. Prometheus 2:1 ILR opens a gap in the C ring while the Mimas 4:1 ILR launches a wave. The Mimas 3:1 IVR opens a gap, while the Titan -1:0 nodal resonance launches a wave. Estimates for the strengths of these satellite torques are taken from Rosen et al. (1991a,b) and Marley & Porco (1993).

Conspicuously missing waves?

Inspection of Figure 4.6 reveals a few f–mode resonances that this simple excitation model predicts to experience strong forcing, but where no waves have yet

been detected. Four of the OLRs with $m = \ell - 2$ have normalized torques predicted to be greater than that of the detected $(\ell, m) = (13, 11)$ OLR. The most obvious of these is the $(8, 6)$ OLR, which this model predicts to lie at 74,940 km, happening to be almost exactly coincident with the detected W74.93 and W74.94 OVR features (French et al. 2019). The fact that these OVR waves apparently dominate the signal at this position betrays some tension with the spectrum of amplitudes we have assumed, which predicts W74.93 and W74.94 to have torques one to three orders of magnitude lower than that predicted for the $(8, 6)$ OLR. Given the close proximity of these resonances, an appeal to the spatial dependence of Σ seems unlikely to resolve this tension.

Of the remaining $m = \ell - 2$ OLRs stronger than $(13, 11)$, none among $(10, 8)$, $(11, 9)$, or $(12, 10)$ have had associated wave detections. This may be attributable to strong perturbations from the Titan apsidal resonance as discussed above. Among the predicted $m = \ell - 4$ resonances, the $(12, 8)$ OLR at 74,556 km is quite close to the inner boundary of the C ring where there are a series of gaps that have yet to be fully understood. Falling in such a gap could render such a resonance unobservable, although within the model uncertainty, this resonance could lie between the gaps or on gap edges.

As for the OVRs, the only resonances that yield waves that have been detected so far in the C ring are the four that fall closest to Saturn, and indeed the strongest predicted waves in each $\ell - m$ have been observed. It warrants closer attention that three of the four strongest OVRs predicted in the C ring have not been associated with any wave feature, while waves have been observed at what should be weaker OVRs with $\ell - m = 3$ and $\ell - m = 5$. These three "missing waves" correspond to the $(\ell, m) = (6, 5)$,

Table 4.2: Predicted OLRs and OVRs in the C ring without wave detections

ℓ	m	Type	$\Omega_{\rm pat}$ (deg day^{-1})	Remark (see §4.6)
11	11	OLR	1368.5–1371.5	
12	12	OLR	1346.9–1349.7	
13	13	OLR	1327.7–1330.1	
8	6	OLR	1742.1–1747.6	Coincident with W74.93, W74.94
10	8	OLR	1586.9–1591.0	Near Titan apsidal
11	9	OLR	1532.9–1536.4	Near Titan apsidal
12	10	OLR	1488.4–1491.6	
14	12	OLR	1419.3–1421.8	
12	8	OLR	1695.6–1699.5	Among gaps
14	10	OLR	1568.6–1571.6	Near Titan apsidal
15	11	OLR	1521.4–1524.1	Near Titan apsidal
6	5	OVR	1737.0–1743.6	Near Titan apsidal
7	6	OVR	1646.4–1652.1	Near Titan apsidal
8	7	OVR	1578.0–1582.8	
9	8	OVR	1523.9–1528.1	
10	9	OVR	1479.8–1483.5	
11	10	OVR	1443.0–1446.3	
12	9	OVR	1581.1–1584.6	Near Titan apsidal
13	10	OVR	1530.1–1533.1	Near Titan apsidal
15	10	OVR	1604.7–1607.6	

Note. — Pattern speeds can be mapped to physical locations given Saturn's equatorial radius and J_{2n} using the relations in §4.4.1.

$(7, 6)$, and $(8, 7)$ Saturn f–modes. Because of their location, it is possible that these waves are present but obscured by the Titan apsidal resonance.

To aid in the search for Saturnian resonances in the C ring, Table 4.2 lists the pattern speeds of all model OLRs and OVRs in the C ring with predicted torques comparable to or larger than than the smallest predicted torque associated with a wave that has already been observed. Likewise, Table 4.3 reports resonances predicted to lie in the D ring, although it is not clear whether any wave patterns there will ultimately be detectable given the ring's faintness.

Table 4.3: Predicted OLRs and OVRs in the D ring

ℓ	m	Type	$\Omega_{\rm pat}$ (deg day^{-1})
5	3	OLR	2314.3–2324.3
6	4	OLR	2034.3–2042.2
7	5	OLR	1861.1–1867.6
9	5	OLR	2063.1–2069.4
10	6	OLR	1901.5–1906.8
11	7	OLR	1784.6–1789.0
2	1	OVR	3359.2–3400.7
3	2	OVR	2423.7–2433.4
4	3	OVR	2061.8–2070.8
7	4	OVR	2177.3–2185.2
8	5	OVR	1968.1–1974.5
9	6	OVR	1826.1–1831.4
11	6	OVR	1970.5–1975.6
12	7	OVR	1841.5–1845.9
13	8	OVR	1743.8–1747.5

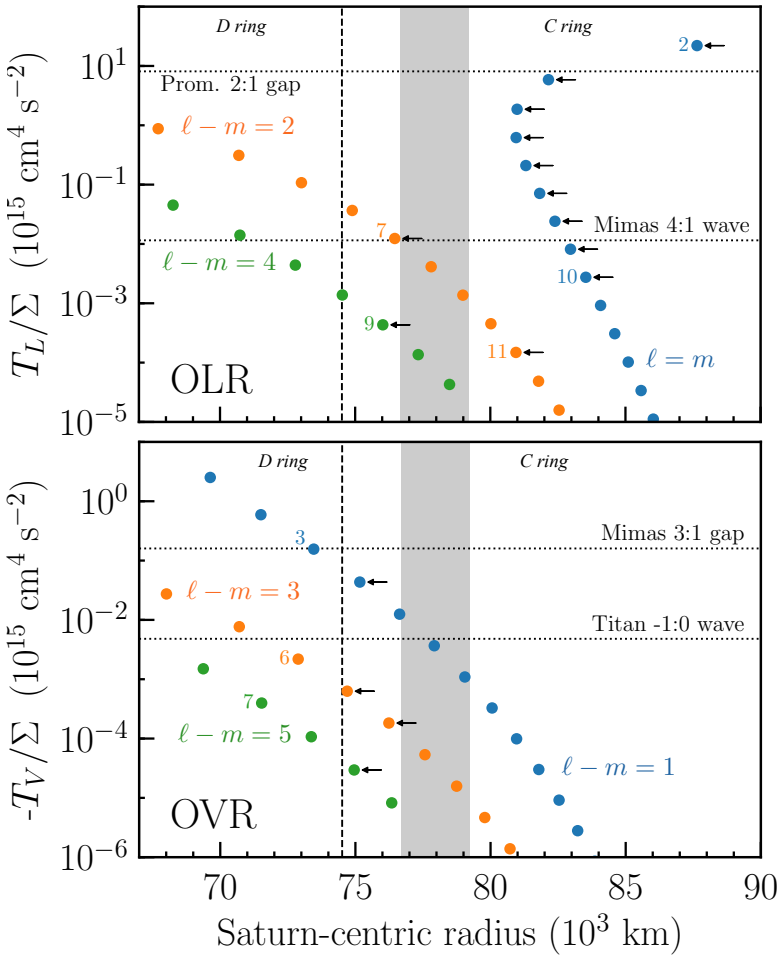

Figure 4.6: Strengths of torques per surface mass density exerted on the C and D rings by model Saturnian f–modes, with amplitudes assigned according to equal energy per mode following Equation 4.19. Model points (filled circles; shown for one randomly drawn interior model) are colored by their value of $\ell - m$. Arrows highlight model f–modes that we have identified with observed waves as in Table 4.5. The grey shaded region in both panels represents the region where maximum radial variations in ring orbits caused by the Titan 1:0 apsidal ILR exceed 300 m, making the detection of wave features more difficult; see §4.6. A subset of resonances have been labeled to their left by their azimuthal wavenumber m for ease of identification. Torques associated with waves or gaps at example satellite ILRs or IVRs in the C ring are indicated with dotted horizontal lines.

4.7 Discussion

This work offers interpretations for the set of inward-propagating density waves and outward-propagating bending waves observed in Saturn's C ring in terms of resonances with Saturnian f–modes. It also demonstrates that Saturn's rotation state is of critical importance for Saturn ring seismology, a fact made evident by the systematic mismatch with the observed pattern speeds of these waves obtained assuming that Saturn rotates rigidly at the *Voyager* System III magnetospheric period of Desch & Kaiser (1981) or slower (see Figure 4.4). The interior configurations considered to arrive at this conclusion accounted somewhat generously for the freedom in the low-order gravity field, because the likelihood function used to obtain our posterior distribution of interior models assumed an inflated variance on J_2 to accord with the numerical precision of our theory of figures implementation (see §4.2.1). Because the resulting distribution included a diversity of heavy element and helium distributions, envelope transition locations, and core masses, the seismology suggests a tension with the *Voyager* rotation rate commonly assumed for Saturn's interior that different three-layer interior models seem unlikely to resolve. This conclusion based on the ring seismology adds support to the notion that periodicities in Saturn's magnetospheric emission (e.g., Desch & Kaiser 1981; Gurnett et al. 2005; Giampieri et al. 2006) may not be consistently coupled to the rotation of Saturn's interior (e.g., Gurnett et al. 2007; Read et al. 2009).

The present model is potentially oversimplified in two major ways. First, the model is not suited to address the close multiplets of waves observed to have the same azimuthal wavenumber m, namely the multiplets of waves in the C ring with $m = 2$

and $m = 3$. The bulk of these seem naturally explained by the model of Fuller (2014), wherein avoided crossings between the f–modes and deep g–modes of higher angular degree give rise to a number of strong perturbations with the same m value. However, in the wealth of new OLR and OVR wave patterns that have been measured from increasingly low signal to noise VIMS data since Hedman & Nicholson (2014), it seems that only two waves add to the mixed-mode picture, both with $m = 2$: the close-in W76.44 wave, and the Maxwell ringlet wave whose frequency and m number were predicted by Fuller (2014). The f–modes of higher angular degree have less amplitude in the deep interior and so are less likely to undergo degenerate mixing with any deep g–modes strongly. Indeed, there is not yet any direct evidence for f–modes with $\ell > 3$ undergoing avoided crossings with deep g–modes, although the outlying $(5, 4)$ OVR warrants closer scrutiny in the mixed-mode context.

The second major simplification of the present model is the assumption that Saturn rotates rigidly. While upper limits can be established for the depth of shear in Jupiter or Saturn's envelopes on magnetohydrodynamic grounds (Liu et al. 2008; Cao & Stevenson 2017), evidence gathered from spacecraft indicate that zonal wind patterns do penetrate to significant depths (Smith et al. 1982; Kaspi et al. 2018). It has been proposed that the insulating molecular regions of these planets may be rotating differentially on concentric cylinders (Busse 1976; Ingersoll & Pollard 1982; Ingersoll & Miller 1986), the zonal winds being the surface manifestation of these cylinders of constant angular velocity. The mode identifications made in §4.5 and Table 4.5 reveal that the seismological dataset now samples a variety of radial (via the angular degree

ℓ) and latitudinal (via the latitudinal wavenumber $\ell - m$) structures within Saturn and so should strongly constrain differential rotation in Saturn's interior. If our rigid model systematically underpredicted f–mode frequencies toward high ℓ, this would indicate that Saturn's outer envelope rotates faster than the bulk rotation. Such a result would be qualitatively consistent with the expectation for rotation on cylinders or an eastward equatorial jet that extends to significant depth, as well as with the rotation profiles that Iess et al. (2019) deduced from the *Cassini* Grand Finale gravity orbits. As discussed in §4.5.2, the lack of any such obvious systematic dependence of wave pattern speed residuals on ℓ (see Figure 4.5) offers a preliminary indication that Saturn does *not* experience strong differential rotation as a function of radius within the volume sampled by the $\ell \geq 4$ f–modes considered in this analysis, although we emphasize that the inclusion of higher order rotation corrections is necessary to confirm this.

The modes identified here also contain four instances of a pair of modes belonging to the same multiplet, i.e., a pair described by the same angular degree ℓ but different azimuthal order m. This carries significance for the prospect of deducing Saturn's rotation profile from the frequency splitting within each multiplet, although the important centrifugal forces and ellipticity due to Saturn's rapid rotation complicates the picture compared to the first-order rotation kernels commonly applied to helioseismology (Thompson et al. 2003) and asteroseismology (e.g., Beck et al. 2012). The frequency offsets that remain between modes with the same ℓ but different $\ell - m$ may point to a latitude-dependent spin frequency, although the manner in which this would fit in with a radius-independent spin frequency is unclear. Quantitative constraints on

differential rotation via the f–modes awaits future work.

4.8 Conclusions

We have presented new Saturn interior models and used them to predict the frequency spectrum of Saturn's nonradial acoustic oscillations. Comparison with waves observed in Saturn's C ring through *Cassini* VIMS stellar occultations reveals that the majority of these waves that are driven at frequencies higher than the ring mean motion are driven by Saturn's fundamental acoustic modes of low to intermediate angular degree ℓ.

The frequencies of Saturn's f–modes probe not only its interior mass distribution, but also its rotation state, especially those modes of higher ℓ. We used the frequencies of the observed wave patterns to make a seismological estimate of Saturn's rotation period assuming that it rotates rigidly. Using these optimized models, we proposed that small but significant residual signal in the frequencies of the observed waves as a function of ℓ suggests that Saturn's outer envelope may rotate differentially, although we are unable to draw quantitative conclusions given the accuracy with which the present theory accounts for rotation in predicting the f–mode frequencies.

Saturn ring seismology is an interesting complement to global helioseismology, ground-based Jovian seismology, and asteroseismology of solar-type oscillators. Because the rings are coupled to the oscillations purely by gravity, they are fundamentally sensitive to the modes without nodes in the density perturbation as a function of radius, and the observation of modes from $\ell = 2$ to $\ell \sim 15$ stands in contrast with helioseismol-

ogy where the vast majority of detected modes are acoustic overtones (p–modes) and f–modes only emerge for $\ell \gtrsim 100$ (e.g., Larson & Schou 2008). Likewise ground-based Jovian seismology accesses the mHz-range p–modes and Saturn ring seismology fills in the picture for frequencies down to ~ 100 μHz. Because of their point-source nature, main sequence and red giant stars with *CoRoT* and *Kepler* asteroseismology means that typically only dipole ($\ell = 1$) or quadrupole ($\ell = 2$) modes are observable because of geometric cancellation for modes of higher ℓ (Chaplin & Miglio 2013). In contrast, the proximity of the C and D rings to Saturn renders them generally sensitive also to higher ℓ so long as the modes exhibit the correct asymmetries. We finally reiterate that Saturn is a rapid rotator ($\Omega_S/\sigma_0 \sim 0.4$), more in line with pulsating stars on the upper main sequence (Soufi et al. 1998) than with stars with *CoRoT* and *Kepler* asteroseismology, and to our knowledge this is the most complete set of modes characterized to date for such a rapidly rotating hydrostatic fluid object.

This work buttresses the decades-old hypothesis (Stevenson 1982) that Saturn's ordered ring system acts as a sensitive seismograph for the planet's normal mode oscillations. The set of Saturnian waves detected in the C ring so far thus provide important contraints on Saturn's interior that are generally independent from those offered by the static gravity field. Future interior modeling of the solar system giants will benefit from joint retrieval on the gravity harmonics and normal mode eigenfrequencies.

Chapter 5

Summary and Future Directions

5.1 Summary

This thesis examined the structure and long-term evolution of Jupiter and Saturn. Chapter 2 addressed hydrogen-helium immiscibility as it applies to the thermal evolution of Jupiter, applying a Bayesian method to probabilistically estimate (i) the uncertain temperature of the true hydrogen-helium phase transition, which is tightly constrained by the observed helium depletion in Jupiter's atmosphere, and (ii) to what degree if any Jupiter's helium gradient must suppress convection in order to explain the planet's observed heat flow. Chapter 3 incorporated new observational and physical inputs and extended this technique to include Saturn as well, providing a model that reconciles the thermal evolution of Jupiter and Saturn simultaneously. These results represent the first self-consistent explanation for both planets' present-day heat flow in the context of helium rain, demonstrating that neither metallicity gradients nor superadiabatic interiors need be invoked to obtain satisfactory solutions for the cooling

of the gas giants. These models predict Saturn's atmospheric helium mass fraction (relative to hydrogen and helium) to be $Y = 0.12 \pm 0.01$ corresponding to a He/H_2 mixing ratio 0.066 ± 0.006.

Chapter 4 endeavored to interpret a very different dataset, applying models for the static structure of Saturn in order to understand the wealth of new seismic constraints obtained by *Cassini* observations of waves in the rings. Apart from a minority of special cases that will be discussed below, these waves proved to have frequencies and azimuthal wavenumbers in excellent agreement with the fundamental (f–)mode oscillations supported by these Saturn models, confirming the prediction by Marley & Porco (1993) that these Saturnian oscillations resonate with orbits in the C ring. Doppler and Coriolis effects render these frequencies extremely sensitive to Saturn's rotation, allowing a new seismological measurement of Saturn's bulk spin period as $10^{\mathrm{h}}33^{\mathrm{m}}38^{\mathrm{s}}{}^{+1\mathrm{m}52\mathrm{s}}_{-1\mathrm{m}19\mathrm{s}}$. This result brings a new line of evidence in support of the idea that the longer periods evident in Saturn's kilometric radiation do not in fact track the planet's interior rotation. This work highlights the value of the unique "Kronoseismology" dataset, the interpretation of which has only just begun.

5.2 Future directions

The work in this thesis touches on a number of unresolved questions that will be addressed in the coming years.

5.2.1 A stable stratification in Saturn?

Chapter 4 offered specific f–mode interpretations for 14 of the 21 "fast" C ring waves reported in the literature so far (Hedman & Nicholson 2013, 2014; French et al. 2016, 2019; Hedman et al. 2019). The remainder are waves with low azimuthal order ($m = 2$–3) that manifest in *clusters* of waves with a single value of m but with finely split frequencies—a behavior totally uncharacteristic of f–modes that suggests an origin in a more complex oscillation within Saturn. Fuller (2014) demonstrated that the earliest detected among these waves (not incidentally some of the strongest) could be understood as resonances with *mixed* modes inside Saturn. In this scenario the modes responsible for the peculiar ring waves are in fact mixed modes caused by avoided crossings between the f–modes and internal gravity (g–)modes, similar to mixed modes in red giant stars (Chaplin & Miglio 2013) but enhanced by Saturn's rapid rotation (Fuller et al. 2014).

The presence of g–modes in Saturn is profound because these require an interior that is at least partially stably stratified and thus non-adiabatic, a possibility excluded by the traditional assumption of the interior as fully convective. In reality stable stratifications may be a general feature of giant planet interiors given the possibilities of core erosion (Guillot et al. 2004; Wilson & Militzer 2012b,a), the concurrent accretion of solids with gas during core accretion (Helled & Stevenson 2017), and the helium phase separation (Stevenson & Salpeter 1977b) that has been studied at length here. In fact, recent work has argued that Saturn's unexpectedly high luminosity can be explained by a strongly stably stratified interior, such as could be established by a primordial metallicity gradient (Leconte & Chabrier 2013b). Chapter 3 of this work

demonstrated on the contrary that adiabatic, or else only weakly superadiabatic, interiors can also provide satisfactory solutions for Saturn when helium rain is accounted for. If the conclusion of Fuller (2014) is correct then the mixed-mode seismology unambiguously rules out such a fully adiabatic interior, and models for Saturn's thermal evolution and internal structure must be generalized to address nontrivial metallicity distributions and hydrogen-helium immiscibility both.

Beyond the mere existence of f–g mixed modes in Saturn, their actual frequencies are powerful quantitative constraints for the deep interior. The frequencies of g–modes are dictated by the location and strength of the stable stratification via the magnitude of the buoyancy frequency N and the radial extent of the region where $N^2 > 0$. The frequencies of the seven known $m = 2$ and $m = 3$ waves that appear to be driven by Saturnian mixed modes may therefore offer a singular opportunity to ascertain the physical origin of Saturn's deep stable stratification because the profile of N expected as a result of, say, helium rain is different from that expected for an eroded core. While a simplistic model developed by Fuller (2014) demonstrated proof of concept, no realistic interior model has incorporated these new constraints. While the interpretation of these frequencies is somewhat more involved than the interpretation of the low-order zonal gravity harmonics usually used to constrain Saturn's deep interior, in the long run they may be more informative.

5.2.2 Saturn's seismological rotation

Even putting aside Saturn's mixed modes at $m = 2$–3, the 14 waves interpreted in Chapter 4 have more to say. The rigid rotation assumption of the models therein is

a fair assumption for the conductive metallic interior (Liu et al. 2008; Cao & Stevenson 2017) but almost certainly an oversimplification for the molecular hydrogen envelope above, especially in light of the conclusions of Iess et al. (2019) based on *Cassini* Grand Finale gravity field measurements. While rigid models yielded a satisfactory fit to the *ensemble* of wave frequencies corresponding to f–modes, the best fit betrays small but potentially significant residuals (Figure 4.5) that may contain the signature of differential rotation in the interior. However, these models treated rotation using a perturbation theory accurate only to second order in Saturn's spin frequency, precluding any categorical statement about Saturn's differential rotation. A theory more accurately treating effects associated with Saturn's rapid rotation, be it through a higher-order perturbation theory (e.g., Karami 2008) or through non-perturbative methods (e.g., Mirouh et al. 2018), will offer either a confirmation of the deep differential rotation inferred by Iess et al. (2019) or an indication that a different profile is required.

5.2.3 Excitation of gas giant oscillations

The mechanism or mechanisms responsible for exciting gas giant oscillations to observable levels remains unsolved. Stochastic solar-like excitation by turbulent convection fails to explain the $\gtrsim 10$ cm displacement amplitude modes that ring seismology suggests in Saturn and ground-based seismology suggests in Jupiter (Gaulme et al. 2011). Recent theoretical efforts have explored driving by an opacity mechanism (Dederick & Jackiewicz 2017), moist convection (Dederick et al. 2018; Markham & Stevenson 2018), and giant impacts (Wu & Lithwick 2019). Finding that water storms are energetically insignificant for driving the Jovian oscillations reported by Gaulme et al. (2011),

Markham & Stevenson posited that deeper storms associated with silicate condensation could be viable, although no obvious means exists for testing that scenario. Wu & Lithwick argued that in the case of Saturn, the leading sources of damping for observed f–modes are the very ring waves that reveal their existence in the first place. In this case the theory describing the driving of spiral density waves at Lindblad resonances (Goldreich & Tremaine 1979) straightforwardly predicts their mode lifetimes. These lifetimes may be of order 10^4–10^7 yr for modes spanning $\ell = 2$–10, long enough that their lifetimes span the expectation for impacts by bodies whose sizes span 8–80 km. Such large impacts appear to yield a scaling that naturally explains Saturn's trend of increasing f–mode energy with increasing $\ell \gtrsim 5$, but fail to explain the major secondary peak in mode energy at $\ell \leq 4$. These large amplitudes at low ℓ suggest a missing excitation mechanism—weaker damping seems unlikely because the ring wave damping is well understood—the nature of which remains a mystery. Theoretical work on this problem may need to account for the fact that these are the same modes that are affected by mode mixing, although at first glance that seems likely to only enhance their dissipation.

An important implication of the model advanced by Wu & Lithwick is that given the stochastic nature of forcing by giant impacts—both in terms of timing of impulses and in terms of impact angle—f– and p–modes with a wide variety of angular structure (ℓ and m) should be excited. The vast majority of these modes in Saturn would not satisfy resonances with ring orbits and hence would not suffer this resonant dissipation. Indeed in Jupiter, whose past included larger, more frequent impacts, there

is no significant ring system to speak of. Thus unless all of these modes experience some source of damping that has not been identified, Jupiter and Saturn should both be ringing quite resoundingly. Wu & Lithwick showed that the corresponding modes may be detectable, with a gravity signal dominated by the f–modes and a radial velocity signal dominated by the p–modes. In particular the potential perturbation expected for the Jupiter's f–modes is marginally within the *Juno* gravity sensitivity for odd ℓ, a possibility already considered by Durante et al. (2017) but in need of revisiting given these dramatically larger estimates for mode amplitudes. Likewise for Saturn, the proximal orbits by *Cassini* have already evinced a complex gravitational potential that has been challenging to interpret (Iess et al. 2019), and future work should determine whether strong f–modes otherwise concealed from view are playing a part.

5.2.4 Stable stratifications and jovian dynamos

The question of stable stratifications in the jovian interiors if of critical importance from the perspective of their dynamos. Jupiter shows a strong, complex external magnetic field in line with expectations for a field supported by turbulent convection in the metallic interior. Saturn, on the other hand, shows a weak field that is curiously almost perfectly azimuthally symmetric, with recent measurements from *Cassini* quoting an upper bound on the overall tilt of Saturn's magnetic dipole moment of mere arcseconds (Dougherty et al. 2018). Following Cowling (1933) the deep magnetic field certainly has a more complicated structure, and the common feature of the models explaining the surprisingly restrained external field (Stevenson 1982b; Stanley 2010; Cao et al. 2012) is an appeal to a stable stratification *outside* an inner, electrically con-

ducting, fully convective dynamo generation region. The stably stratified layer could support differential flows that tend to attenuate the non-axisymmetric components of the magnetic field, giving rise to the highly ordered field observed outside the planet. This picture for Saturn's internal structure is generally different from those considered so far to interpret Saturn's thermal evolution (Fortney & Hubbard 2003 and Chapters 2 and 3 of this dissertation, or the quite different models of Leconte & Chabrier 2013b or Vazan et al. 2016a), oscillations (Fuller 2014 and Chapter 4 of this work), and static gravity field (Nettelmann et al. 2013; Iess et al. 2019). Different datasets, when taken piecemeal, inspire fundamentally different interior models, an idea demonstrated schematically for Saturn in Figure 5.1. It remains a longer-term goal to bring the full wealth of independent magnetic, gravitational, and seismic information to bear simultaneously on our understanding of Saturn's complicated interior.

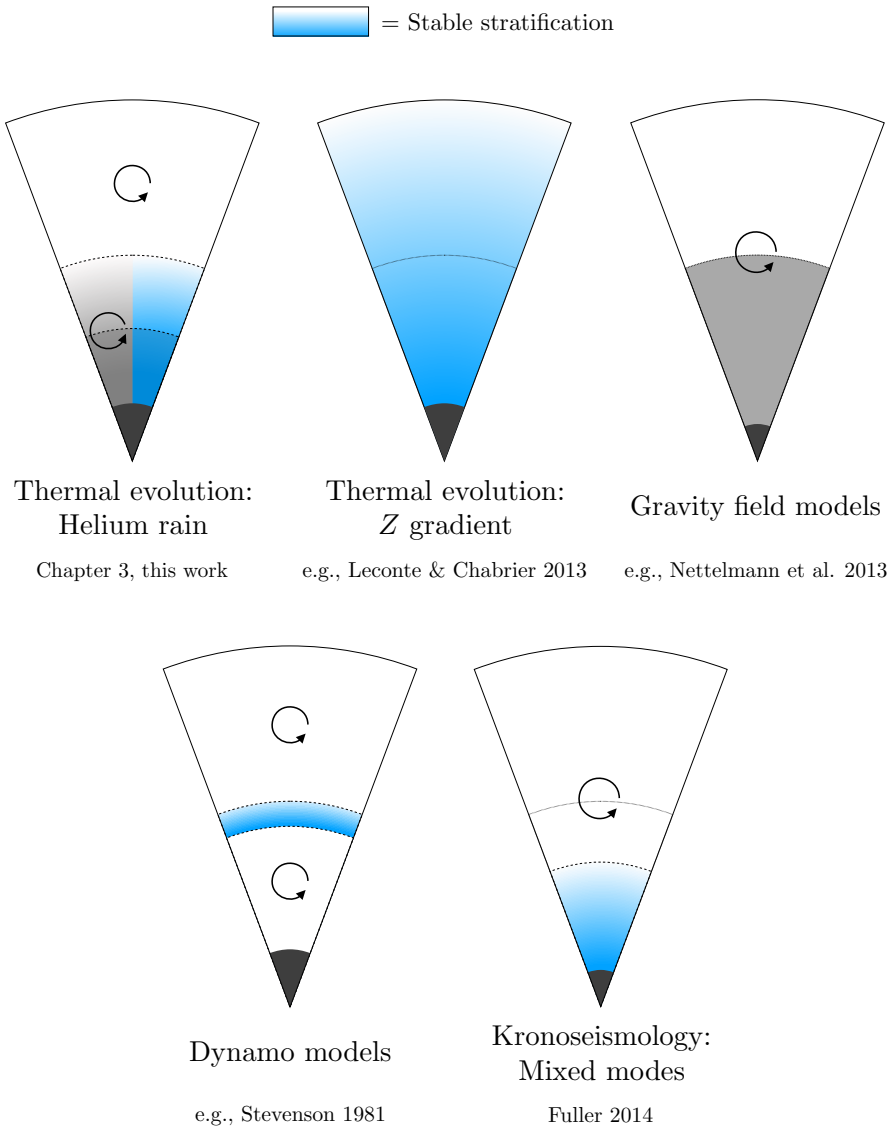

Figure 5.1: Possible interior structures for Saturn motivated by disparate datasets. The most fundamental difference among these models is their prediction for the location and extent of Saturn's stable stratification, if one exists.

Bibliography

Achterberg, R. K., Schinder, P. J., & Flasar, F. M. 2016, in AAS/Division for Planetary Sciences Meeting Abstracts, Vol. 48, AAS/Division for Planetary Sciences Meeting Abstracts #48, 508.01

Akaike, H. 1974, IEEE Transactions on Automatic Control, 19, 716

Anderson, J. D., & Schubert, G. 2007, Science, 317, 1384

Asplund, M., Grevesse, N., Sauval, A. J., & Scott, P. 2009, ARA&A, 47, 481

Atreya, S. K., Crida, A., Guillot, T., et al. 2016, arXiv e-prints, arXiv:1606.04510

Baillié, K., Colwell, J. E., Lissauer, J. J., Esposito, L. W., & Sremčević, M. 2011, Icarus, 216, 292

Banfield, D., Gierasch, P. J., Conrath, B. J., et al. 2014, in AAS/Division for Planetary Sciences Meeting Abstracts, Vol. 46, AAS/Division for Planetary Sciences Meeting Abstracts #46, 512.01

Baraffe, I., Chabrier, G., & Barman, T. 2008a, A&A, 482, 315

—. 2008b, A&A, 482, 315

Beck, P. G., Montalban, J., Kallinger, T., et al. 2012, Nature, 481, 55

Becker, A., Lorenzen, W., Fortney, J. J., et al. 2014, ApJS, 215, 21

Bolton, S. J., Lunine, J., Stevenson, D., et al. 2017, Space Sci. Rev., 213, 5

Busse, F. H. 1976, Icarus, 29, 255

Cao, H., Russell, C. T., Wicht, J., Christensen, U. R., & Dougherty, M. K. 2012, Icarus, 221, 388

Cao, H., & Stevenson, D. J. 2017, Icarus, 296, 59

Cassisi, S., Potekhin, A. Y., Pietrinferni, A., Catelan, M., & Salaris, M. 2007, ApJ, 661, 1094

Chabrier, G., Mazevet, S., & Soubiran, F. 2019, ApJ, 872, 51

Chaplin, W. J., & Miglio, A. 2013, ARA&A, 51, 353

Christensen-Dalsgaard, J. 2002, Reviews of Modern Physics, 74, 1073

Colwell, J. E., Nicholson, P. D., Tiscareno, M. S., et al. 2009, The Structure of Saturn's Rings, 375

Connelly, J. N., Bizzarro, M., Krot, A. N., et al. 2012, Science, 338, 651

Conrath, B. J., & Gautier, D. 2000, Icarus, 144, 124

Conrath, B. J., Gautier, D., Hanel, R. A., & Hornstein, J. S. 1984, ApJ, 282, 807

Cowling, T. G. 1933, MNRAS, 94, 39

Dederick, E., & Jackiewicz, J. 2017, ApJ, 837, 148

Dederick, E., Jackiewicz, J., & Guillot, T. 2018, ApJ, 856, 50

Desch, M. D., & Kaiser, M. L. 1981, Geophys. Res. Lett., 8, 253

Dougherty, M. K., Cao, H., Khurana, K. K., et al. 2018, Science, 362, aat5434

Durante, D., Guillot, T., & Iess, L. 2017, Icarus, 282, 174

Edgington, S. G., & Spilker, L. J. 2016, Nature Geoscience, 9, 472

Flasar, F. M. 1973, ApJ, 186, 1097

Fletcher, L. N., Orton, G. S., Teanby, N. A., Irwin, P. G. J., & Bjoraker, G. L. 2009, Icarus, 199, 351

Foreman-Mackey, D., Hogg, D. W., Lang, D., & Goodman, J. 2013, PASP, 125, 306

Fortney, J. J., Helled, R., Nettelmann, N., et al. 2016, ArXiv e-prints, arXiv:1609.06324

Fortney, J. J., & Hubbard, W. B. 2003, Icarus, 164, 228

Fortney, J. J., Ikoma, M., Nettelmann, N., Guillot, T., & Marley, M. S. 2011, ApJ, 729, 32

Freedman, R. S., Marley, M. S., & Lodders, K. 2008, ApJS, 174, 504

French, M., Becker, A., Lorenzen, W., et al. 2012, ApJS, 202, 5

French, M., Mattsson, T. R., Nettelmann, N., & Redmer, R. 2009, Phys. Rev. B, 79, 054107

French, R. G., McGhee-French, C. A., Nicholson, P. D., & Hedman, M. M. 2019, Icarus, 319, 599

French, R. G., Nicholson, P. D., Hedman, M. M., et al. 2016, Icarus, 279, 62

Fuller, J. 2014, Icarus, 242, 283

Fuller, J., Lai, D., & Storch, N. I. 2014, Icarus, 231, 34

Gaulme, P., Schmider, F.-X., Gay, J., Guillot, T., & Jacob, C. 2011, A&A, 531, A104

Giampieri, G., Dougherty, M. K., Smith, E. J., & Russell, C. T. 2006, Nature, 441, 62

Goldreich, P., & Tremaine, S. 1979, ApJ, 233, 857

Gough, D. 1980, in Lecture Notes in Physics, Berlin Springer Verlag, Vol. 125, Nonradial and Nonlinear Stellar Pulsation, ed. H. A. Hill & W. A. Dziembowski, 1

Graboske, Jr., H. C., Pollack, J. B., Grossman, A. S., & Olness, R. J. 1975, ApJ, 199, 265

Grossman, A. S., Pollack, J. B., Reynolds, R. T., Summers, A. L., & Graboske, H. C. 1980, Icarus, 42, 358

Guillot, T., Chabrier, G., Gautier, D., & Morel, P. 1995, ApJ, 450, 463

Guillot, T., Stevenson, D. J., Hubbard, W. B., & Saumon, D. 2004, The interior of Jupiter, ed. F. Bagenal, T. E. Dowling, & W. B. McKinnon, 35–57

Guillot, T., Miguel, Y., Militzer, B., et al. 2018, Nature, 555, 227

Gurnett, D. A., Persoon, A. M., Kurth, W. S., et al. 2007, Science, 316, 442

Gurnett, D. A., Kurth, W. S., Hospodarsky, G. B., et al. 2005, Science, 307, 1255

Hanel, R., Conrath, B., Herath, L., Kunde, V., & Pirraglia, J. 1981a, J. Geophys. Res., 86, 8705

Hanel, R., Conrath, B., Flasar, F. M., et al. 1981b, Science, 212, 192

Hanel, R. A., Conrath, B. J., Kunde, V. G., Pearl, J. C., & Pirraglia, J. A. 1983, Icarus, 53, 262

Hedman, M. M., & Nicholson, P. D. 2013, AJ, 146, 12

—. 2014, MNRAS, 444, 1369

Hedman, M. M., Nicholson, P. D., & French, R. G. 2019, AJ, 157, 18

Helled, R., Galanti, E., & Kaspi, Y. 2015, Nature, 520, 202

Helled, R., & Stevenson, D. 2017, ApJ, 840, L4

Hubbard, W. B. 1968, ApJ, 152, 745

—. 1969, ApJ, 155, 333

—. 1970, ApJ, 162, 687

Hubbard, W. B., & Dewitt, H. E. 1985, ApJ, 290, 388

Hubbard, W. B., Guillot, T., Marley, M. S., et al. 1999, Planet. Space Sci., 47, 1175

Hubbard, W. B., & Militzer, B. 2016a, ApJ, 820, 80

—. 2016b, ApJ, 820, 80

Hubbard, W. B., & Smoluchowski, R. 1973, Space Sci. Rev., 14, 599

Iess, L., Folkner, W. M., Durante, D., et al. 2018, Nature, 555, 220

Iess, L., Militzer, B., Kaspi, Y., et al. 2019, Science, https://science.sciencemag.org/content/early/2019/01/16/science.aat2965.full.pdf

Ingersoll, A. P., & Miller, R. L. 1986, Icarus, 65, 370

Ingersoll, A. P., & Pollard, D. 1982, Icarus, 52, 62

Jacobson, R. A., Antreasian, P. G., Bordi, J. J., et al. 2006, AJ, 132, 2520

Karami, K. 2008, Chinese J. Astron. Astrophys., 8, 285

Kaspi, Y., Galanti, E., Hubbard, W. B., et al. 2018, Nature, 555, 223

Kato, S. 1966, PASJ, 18, 374

Kippenhahn, R., & Weigert, A. 1990, Stellar Structure and Evolution,

Koskinen, T. T., & Guerlet, S. 2018, Icarus, 307, 161

Kumar, P. 1997, in IAU Symposium, Vol. 181, Sounding Solar and Stellar Interiors, ed. J. Provost & F.-X. Schmider, ISBN0792348389

Kurokawa, H., & Inutsuka, S.-i. 2015, ApJ, 815, 78

Landau, L. D., & Lifshitz, E. M. 1959,

Larson, T. P., & Schou, J. 2008, in Journal of Physics Conference Series, Vol. 118,

Journal of Physics Conference Series, 012083

Leconte, J., & Chabrier, G. 2013a, Nature Geoscience, 6, 347

—. 2013b, Nature Geoscience, 6, 347

Ledoux, P. 1947, ApJ, 105, 305

—. 1951, ApJ, 114, 373

Li, L., Conrath, B. J., Gierasch, P. J., et al. 2010, Journal of Geophysical Research (Planets), 115, E11002

Li, L., Baines, K. H., Smith, M. A., et al. 2012, Journal of Geophysical Research (Planets), 117, E11002

Li, L., Jiang, X., West, R. A., et al. 2018, Nature Communications, 9, 3709

Lindal, G. F., Sweetnam, D. N., & Eshleman, V. R. 1985, AJ, 90, 1136

Liu, J., Goldreich, P. M., & Stevenson, D. J. 2008, Icarus, 196, 653

Lorenzen, W., Holst, B., & Redmer, R. 2009, Physical Review Letters, 102, 115701

—. 2011, Phys. Rev. B, 84, 235109

Low, F. J. 1966, AJ, 71, 391

Mahaffy, P. R., Niemann, H. B., Alpert, A., et al. 2000, J. Geophys. Res., 105, 15061

Mankovich, C., Fortney, J. J., & Moore, K. L. 2016, ApJ, 832, 113

Mankovich, C., Marley, M. S., Fortney, J. J., & Movshovitz, N. 2019, ApJ, 871, 1

Markham, S., & Stevenson, D. 2018, Icarus, 306, 200

Marley, M. S. 1990, PhD thesis, Arizona Univ., Tucson.

—. 1991, Icarus, 94, 420

—. 2014, Icarus, 234, 194

Marley, M. S., & Hubbard, W. B. 1988, in BAAS, Vol. 20, Bulletin of the American Astronomical Society, 870

Marley, M. S., Hubbard, W. B., & Porco, C. C. 1987, in BAAS, Vol. 19, Bulletin of the American Astronomical Society, 889

Marley, M. S., Hubbard, W. B., & Porco, C. C. 1989, in BAAS, Vol. 21, Bulletin of the American Astronomical Society, 928

Marley, M. S., & Porco, C. C. 1993, Icarus, 106, 508

McMahon, J. M., Morales, M. A., Pierleoni, C., & Ceperley, D. M. 2012, Reviews of Modern Physics, 84, 1607

Miguel, Y., Guillot, T., & Fayon, L. 2016, A&A, 596, A114

Militzer, B., & Hubbard, W. B. 2013, ApJ, 774, 148

Militzer, B., Hubbard, W. B., Vorberger, J., Tamblyn, I., & Bonev, S. A. 2008, ApJ, 688, L45

Mirouh, G. M., Angelou, G. C., Reese, D. R., & Costa, G. 2018, MNRAS, arXiv:1811.05769

Mirouh, G. M., Garaud, P., Stellmach, S., Traxler, A. L., & Wood, T. S. 2012, ApJ, 750, 61

Moll, R., Garaud, P., Mankovich, C., & Fortney, J. J. 2017, ApJ, 849, 24

Morales, M. A., Hamel, S., Caspersen, K., & Schwegler, E. 2013, Phys. Rev. B, 87, 174105

Morales, M. A., Schwegler, E., Ceperley, D., et al. 2009, Proceedings of the National Academy of Science, 106, 1324

Mosser, B., Mekarnia, D., Maillard, J. P., et al. 1993, A&A, 267, 604

Nettelmann, N. 2017, A&A, 606, A139

Nettelmann, N., Becker, A., Holst, B., & Redmer, R. 2012, ApJ, 750, 52

Nettelmann, N., Fortney, J. J., Moore, K., & Mankovich, C. 2015, MNRAS, 447, 3422

Nettelmann, N., Püstow, R., & Redmer, R. 2013, Icarus, 225, 548

Nicholson, P. D., French, R. G., McGhee-French, C. A., et al. 2014, Icarus, 241, 373

Nicholson, P. D., & Porco, C. C. 1988, J. Geophys. Res., 93, 10209

Niemann, H. B., Atreya, S. K., Carignan, G. R., et al. 1998, J. Geophys. Res., 103, 22831

Stevenson, D. J. 1982, EOS Transactions of the American Geophysical Union, 63, 1020

Orton, G. S., & Ingersoll, A. P. 1980, J. Geophys. Res., 85, 5871

Paxton, B., Bildsten, L., Dotter, A., et al. 2011, ApJS, 192, 3

Paxton, B., Cantiello, M., Arras, P., et al. 2013, ApJS, 208, 4

Paxton, B., Marchant, P., Schwab, J., et al. 2015, ApJS, 220, 15

Pearl, J. C., & Conrath, B. J. 1991, J. Geophys. Res., 96, 18

Pollack, J. B., Grossman, A. S., Moore, R., & Graboske, Jr., H. C. 1977, Icarus, 30, 111

Porco, C. C., Baker, E., Barbara, J., et al. 2005, Science, 307, 1226

Püstow, R., Nettelmann, N., Lorenzen, W., & Redmer, R. 2016, Icarus, 267, 323

Read, P. L., Dowling, T. E., & Schubert, G. 2009, Nature, 460, 608

Rosen, P. A. 1989, PhD thesis, Stanford Univ., CA.

Rosen, P. A., Tyler, G. L., & Marouf, E. A. 1991a, Icarus, 93, 3

Rosen, P. A., Tyler, G. L., Marouf, E. A., & Lissauer, J. J. 1991b, Icarus, 93, 25

Rosenblum, E., Garaud, P., Traxler, A., & Stellmach, S. 2011, ApJ, 731, 66

Roulston, M. S., & Stevenson, D. J. 1995, in , AGU, 343

Saio, H. 1981, ApJ, 244, 299

Salpeter, E. E. 1973, ApJ, 181, L83

Saumon, D., Chabrier, G., & van Horn, H. M. 1995, ApJS, 99, 713

Saumon, D., & Guillot, T. 2004, ApJ, 609, 1170

Schmider, F. X., Appourchaux, T., Gaulme, P., et al. 2013, in Fifty Years of Seismology of the Sun and Stars, Vol. 478, 119

Schöttler, M., & Redmer, R. 2018, Physical Review Letters, 120, 115703

Schwarzschild, M., & Härm, R. 1958, ApJ, 128, 348

Seidelmann, P. K., Archinal, B. A., A'Hearn, M. F., et al. 2007, Celestial Mechanics and Dynamical Astronomy, 98, 155

Shu, F. H., Cuzzi, J. N., & Lissauer, J. J. 1983, Icarus, 53, 185

Simon, A., Banfield, D., Atkinson, D., & SPRITE Science Team. 2018, in American Astronomical Society Meeting Abstracts, Vol. 231, American Astronomical Society Meeting Abstracts #231, 144.01

Smith, B. A., Soderblom, L., Batson, R. M., et al. 1982, Science, 215, 504

Smoluchowski, R. 1967, Nature, 215, 691

Soufi, F., Goupil, M. J., & Dziembowski, W. A. 1998, A&A, 334, 911

Stanley, S. 2010, Geophys. Res. Lett., 37, L05201

Stevenson, D. J. 1975, Phys. Rev. B, 12, 3999

—. 1979, MNRAS, 187, 129

—. 1982a, Annual Review of Earth and Planetary Sciences, 10, 257

—. 1982b, Geophysical and Astrophysical Fluid Dynamics, 21, 113

Stevenson, D. J., & Salpeter, E. E. 1977a, ApJS, 35, 221

—. 1977b, ApJS, 35, 239

Straus, D. M., Ashcroft, N. W., & Beck, H. 1977, Phys. Rev. B, 15, 1914

Sweigart, A. V., & Gross, P. G. 1974, ApJ, 190, 101

Thompson, M. J., Christensen-Dalsgaard, J., Miesch, M. S., & Toomre, J. 2003, ARA&A, 41, 599

Thompson, S. L. 1990, ANEOS—Analytic Equations of State for Shock Physics Codes, Sandia Natl. Lab. Doc. SAND89-2951, http://prod.sandia.gov/techlib/access-control.cgi/1989/892951.pdf

Thorngren, D. P., Fortney, J. J., Murray-Clay, R. A., & Lopez, E. D. 2016, ApJ, 831, 64

Townsend, R. H. D., & Teitler, S. A. 2013, MNRAS, 435, 3406

Turner, J. S. 1974, Annual Review of Fluid Mechanics, 6, 37

Unno, W., Osaki, Y., Ando, H., Saio, H., & Shibahashi, H. 1989,

Vazan, A., Helled, R., & Guillot, T. 2018, A&A, 610, L14

Vazan, A., Helled, R., Kovetz, A., & Podolak, M. 2015, ApJ, 803, 32

Vazan, A., Helled, R., Podolak, M., & Kovetz, A. 2016a, ApJ, 829, 118

—. 2016b, ApJ, 829, 118

von Zahn, U., Hunten, D. M., & Lehmacher, G. 1998, J. Geophys. Res., 103, 22815

Vorontsov, S. V. 1981, Soviet Ast., 25, 724

Vorontsov, S. V., & Zharkov, V. N. 1981, Soviet Ast., 25, 627

Walin, G. 1964, Tellus, 16, 389

Wilson, H. F., & Militzer, B. 2010, Physical Review Letters, 104, 121101

—. 2012a, Physical Review Letters, 108, 111101

—. 2012b, ApJ, 745, 54

Wood, T. S., Garaud, P., & Stellmach, S. 2013, ApJ, 768, 157

Wu, Y., & Lithwick, Y. 2019, arXiv e-prints, arXiv:1901.04511

Zharkov, V. N., & Trubitsyn, V. P. 1978,

Appendix A

Potential perturbations from nonradial oscillations

The density perturbations associated with nonradial planet oscillations generally lead to gravitational perturbations felt outside the planet. These perturbations can be understood as time-dependent components to the usual zonal and tesseral gravity harmonics, and these are derived here following Marley & Porco (1993).

As in the standard harmonic expansion for the static gravitational potential outside an oblate planet (Zharkov & Trubitsyn 1978), the time-dependent part of the potential arising from nonradial planet oscillations can be expanded as

$$\Phi'(t) = \frac{GM}{r} \sum_{n=0}^{\infty} \left\{ -\sum_{\ell=2}^{\infty} \left(\frac{a}{r}\right)^{\ell} J'_{\ell n} P_{\ell}(\cos\theta) + \sum_{\ell=2}^{\infty} \sum_{m=-\ell}^{\ell} \left(\frac{a}{r}\right)^{\ell} P_{\ell}^{m}(\cos\theta) \left[C'_{\ell m n} \cos m\varphi + S'_{\ell m n} \sin m\varphi \right] \right\}. \tag{A.1}$$

The coefficients $J'_{\ell n}$, $C'_{\ell n}$ and $S'_{\ell n}$ are analogous to the usual gravity harmonics, but with the background density replaced by the Eulerian density perturbation $\rho'(\mathbf{r},t)$ due to the oscillation in the ℓmn mode:

$$\begin{aligned} Ma^{\ell} J'_{\ell n} &= -\int \rho'_{\ell mn}(\mathbf{r},t)\, r^{\ell} P_{\ell}(\cos\theta)\, d\tau, \\ Ma^{\ell} \begin{pmatrix} C'_{\ell mn} \\ S'_{\ell mn} \end{pmatrix} &= \frac{2(\ell-m)!}{(\ell+m)!} \int \rho'_{\ell mn}(\mathbf{r},t)\, r^{\ell} P_{\ell}^{m}(\cos\theta) \begin{pmatrix} \cos m\varphi \\ \sin m\varphi \end{pmatrix} d\tau, \end{aligned} \tag{A.2}$$

where $d\tau = r^2 \sin\theta\, d\theta\, d\varphi\, dr$ is the volume element and the integrals are carried out over the volume of the planet. Given that our solutions for the density perturbation take the form

$$\begin{aligned} \rho'_{\ell mn}(\mathbf{r},t) &= Y_{\ell}^{m}(\theta,\varphi)\rho'_{\ell n}(r)e^{-i\sigma_{\ell mn}t} \\ &= c_0 P_{\ell}^{m}(\cos\theta)\rho'_{\ell n}(r)e^{i(m\varphi-\sigma_{\ell mn}t)}, \end{aligned} \tag{A.3}$$

where

$$c_0 \equiv (-1)^{\frac{m+|m|}{2}} \left[\frac{2\ell+1}{4\pi}\frac{(\ell-|m|)!}{(\ell+|m|)!}\right]^{1/2}, \tag{A.4}$$

the integrals in Equation A.2 are separable:

$$Ma^{\ell} J'_{\ell} = -c_0 e^{-i\sigma t} \int_0^{2\pi} e^{im\varphi}\, d\varphi \times \int_0^{\pi} \left[P_{\ell}(\cos\theta)\right]^2 \sin\theta\, d\theta \int_0^{a} \rho'_{n\ell}(r)\, r^{\ell+2}\, dr \tag{A.5}$$

$$Ma^{\ell} \begin{pmatrix} C'_{\ell m} \\ S'_{\ell m} \end{pmatrix} = \frac{2(\ell-m)!}{(\ell+m)!} c_0 e^{-i\sigma t} \int_0^{2\pi} e^{im\varphi} \begin{pmatrix} \cos m\varphi \\ \sin m\varphi \end{pmatrix} d\varphi \times \int_0^{\pi} \left[P_{\ell}^{m}(\cos\theta)\right]^2 \sin\theta\, d\theta \int_0^{a} \rho'_{n\ell}(r)\, r^{\ell+2}\, dr. \tag{A.6}$$

Notice from the symmetric integrand over azimuth that the J'_{ℓ} only have contributions from axisymmetric ($m = 0$) modes, while the $C'_{\ell m}$ and $S'_{\ell m}$ only have contributions from nonaxisymmetric ($m \neq 0$) modes. Using the orthogonality of the associated Legendre polynomials

$$\int_0^{\pi} P_{\ell}^{m}(\cos\theta) P_{\ell'}^{m'}(\cos\theta)\, \sin\theta\, d\theta = \int_{-1}^{1} P_{\ell}^{m}(\mu) P_{\ell'}^{m'}(\mu)\, d\mu = \frac{2\delta_{\ell\ell'}\delta_{mm'}}{(2\ell+1)} \frac{(\ell+m)!}{(\ell-m)!}, \tag{A.7}$$

Equations A.5 and A.6 reduce to

$$Ma^{\ell} J'_{\ell} = -\left(\frac{4\pi}{2\ell+1}\right)^{1/2} e^{-i\sigma_{\ell mn} t} \int_0^{a} \rho'_{\ell n}(r)\, r^{\ell+2}\, dr, \tag{A.8}$$

$$Ma^{\ell} C'_{\ell m} = (-1)^{\frac{m+|m|}{2}} \left[\frac{4\pi}{(2\ell+1)} \frac{(\ell-|m|)!}{(\ell+|m|)!}\right]^{1/2} e^{-i\sigma_{\ell mn} t} \int_0^{a} \rho'_{\ell n}(r)\, r^{\ell+2}\, dr, \tag{A.9}$$

$$S'_{\ell m} = iC'_{\ell m}. \tag{A.10}$$

The coefficients $S_{\ell m}$ are identical to the $C_{\ell m}$ up to a phase offset and can thus be ignored. These expressions for the coefficients J'_{ℓ} and $C'_{\ell m}$ can be substituted into the

expansion A.1 to write the ℓmn component of the external potential perturbation as

$$\Phi'_{\ell mn}(\mathbf{r},t) = \begin{cases} \dfrac{G}{r^{\ell+1}} P_\ell(\cos\theta) \left(\dfrac{4\pi}{2\ell+1}\right)^{1/2} e^{-i\sigma_{\ell mn}t} \displaystyle\int_0^a \rho'_{\ell mn}(r) r^{\ell+2}\, dr, & m = 0, \\ \dfrac{G}{r^{\ell+1}} P_\ell^m(\cos\theta)(-1)^{\frac{m+|m|}{2}} \left[\dfrac{4\pi}{(2\ell+1)} \dfrac{(\ell-|m|)!}{(\ell+|m|)!}\right]^{1/2} e^{-i\sigma_{\ell mn}t} & \\ \qquad \times \cos m\varphi \int_0^a \rho'_{\ell mn}(r)\, r^{\ell+2}\, dr, & m \neq 0. \end{cases} \tag{A.11}$$

As above, we restrict our attention to prograde f-modes, namely those normal modes having $m > 0$ and $n = 0$. Thus for the modes of interest the amplitude of the potential perturbation felt at a radius r outside Saturn is simply

$$\Phi'_{\ell m0}(r,\theta) = \frac{G}{r^{\ell+1}} P_\ell^m(\cos\theta)(-1)^{\frac{m+|m|}{2}} \left[\frac{4\pi}{(2\ell+1)} \frac{(\ell-|m|)!}{(\ell+|m|)!}\right]^{1/2} \int_0^a \rho'_{\ell m0}(r)\, r^{\ell+2}\, dr \tag{A.12}$$

where the time dependence and azimuthal dependence are omitted for the purposes of estimating the magnitudes of torques on the rings.